Contributions to the FEL'96 Conference, August 26-31, 1996 in Rome, Italy

Contents

Feedback in a soft x-ray FEL by optically generated atomic lattices

B. Adams

Hamburger Synchrotronstrahlungslabor HASYLAB am Deutschen Elektronensynchrotron DESY, 22607 Hamburg, Germany

It is proposed to use a lattice of atoms, generated in an atom beam by a standing wave of laser light, as a Bragg mirror for feedback in an x-ray FEL. This lattice has a low absorption and is immune to radiation damage.

1 Introduction

The multibunch x-ray FEL has the potential to go beyond the self-amplified spontaneous emission (SASE) operation to much better temporal coherence if a small monochromatized fraction of the output can be fed back into the input to serve as a seed for the next buch in the bunch train. There is however the serious obstacle of absorption in and radiation damage to the first feedback mirror.

This paper proposes a novel way to circumvent these problems by use of a recent development in quantum optics, namely the phenomenon of Bragg reflection from lattices of atoms which are bound by a standing wave of light. Light-bound lattices of atoms have been realized by several groups, both in pre-cooled clouds of atoms [1–3] and in an atomic beam [4]. Bragg reflection of light at an optical wavelength from an atomic lattice has been demonstrated by [5]. Typical atom densities in light-bound atomic lattices are 10^9 to 10^{12} atoms per cm^3 [5,6]. At these densities, the absorbance for soft x-rays is very low. In the application discussed here, the atomic lattice would be generated in an atomic beam to be continuously renewed in the interaction zone.

2 The setup

Fig. 1 shows a schematic of the setup. Let z be the coordinate along the FEL amplifier axis and ξ be the direction of the x-ray scattering vector. An atomic

beam is directed at a right angle with respect to the z and ξ axes towards the interaction zone. It is precooled with respect to the ξ direction by an optical molasse. Two counterpropagating laser beams along the $\pm\xi$ axis with crossed linear polarizations generate a standing wave pattern which channels the atoms into lattice planes. They are aligned with respect to the FEL output to Bragg-reflect at the desired wavelength of several nm in a low reflection order, i.e. at small momentum transfer. The reflected beam is then guided back to the input of the FEL amplifier by conventional multilayer mirrors which can be used near back-reflection.

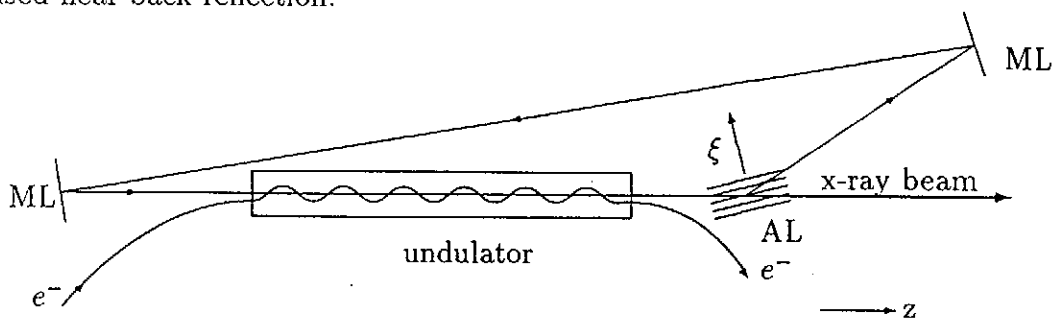

Fig. 1. Schematic of the feedback. AL is the atomic lattice and ML are multilayer mirrors. In this diagram, the atomic beam passes at a right angle through the paper plane.

In this setup, the atomic lattice handles the high power output from the FEL and transmits most of its power to the user stations while the multilayer mirrors which can transfer a large amount of momentum to the x-rays are not exposed to the high power. Most of the FEL output passes straight through the atomic lattice. Some focusing is necessary for optimum feedback. This can be accomplished by using curved multilayer mirrors or by shaping the standing laser wave pattern that generates the atomic lattice by use of lenses or curved mirrors.

3 Atomic lattices bound by light

Periodic optical potentials are generated by the light shift experienced by atoms in a stationary interference pattern of suitably tuned laser light. They can be used to modulate the spatial arrangement of otherwise free atoms which are optically cooled to μK temperatures. A typical setup uses two counterpropagating waves with mutually orthogonal linear polarizations at a frequency ω_ℓ which is close to an atomic $J = 1/2 \rightarrow J = 3/2$ transition at ω_0 [7]. The resulting pattern of elliptical polarization generates $\lambda_\ell/2$-periodic potentials which are offset by $\lambda_\ell/4$ for the two Zeeman sublevels of the $J = 1/2$ state where λ_ℓ is the laser wavelength. By a convenient choice of phases, the $g_\pm$ sublevels are

subjected to the potential [7]

$$U(\xi) = U_0(-2 \pm \cos(2k_\ell \xi))/2 \tag{1}$$

where $k_\ell = 2\pi/\lambda_\ell$ and

$$U_0 = -2\hbar\delta s_0/3 \tag{2}$$

where δ is the detuning $\omega_\ell - \omega_0$ and $s_0 = \Omega_R^2/2(\delta^2 + \gamma^2/4)$ is the saturation parameter. $\Omega_R = -2dE_0/\hbar$ is the resonant Rabi frequency which characterizes the coupling between the atomic dipole d and the field and γ is the natural linewidth. Treated quantum-mechanically, the atoms in the potential $U(\xi)$ have discrete energy levels. In the harmonic approximation [7], the localization of the atoms in the lowest vibrational energy level is given by:

$$\delta\xi = \sqrt{\frac{\hbar}{\sqrt{2mU_0}k_\ell}} \tag{3}$$

where m is the atomic mass.

4 Bragg reflection of x-rays from a light-bound crystal

Bragg reflection of x-rays from an atomic lattice is shown schematically in fig. 2. An atomic beam of width W passes vertically through the paper plane in the figure. A lattice is generated in it by optical laser beams in the $\pm\xi$ directions with wave number k_ℓ. The atoms are then arrayed in layers, spaced at distances of $\ell = \pi/k_\ell$ each. The thickness-to-spacing ratio is $\beta = k_\ell \delta x/\pi$. We define $L = W \tan\Theta$ where Θ is the scattering angle. The number L/ℓ is a measure of the number of lattice planes traversed by the FEL output beam. Due to the low density of the atomic lattice, the extinction length of the reflection is typically much larger than L. Therefore, the width w' of the exiting beam may be larger than w, the width of the incoming beam, as shown in fig. 2.

We will now look at the reflectivity, the energy bandpass width due to the finite size of the reflecting lattice, energy spread due to angular divergences and the issue of recoil energy loss.

Concerning the reflection of x-rays, an atomic lattice is similar to a multilayer mirror because both have a modulation of scatterer density along the scattering vector and are unstructured in the other directions. Following [8], we define

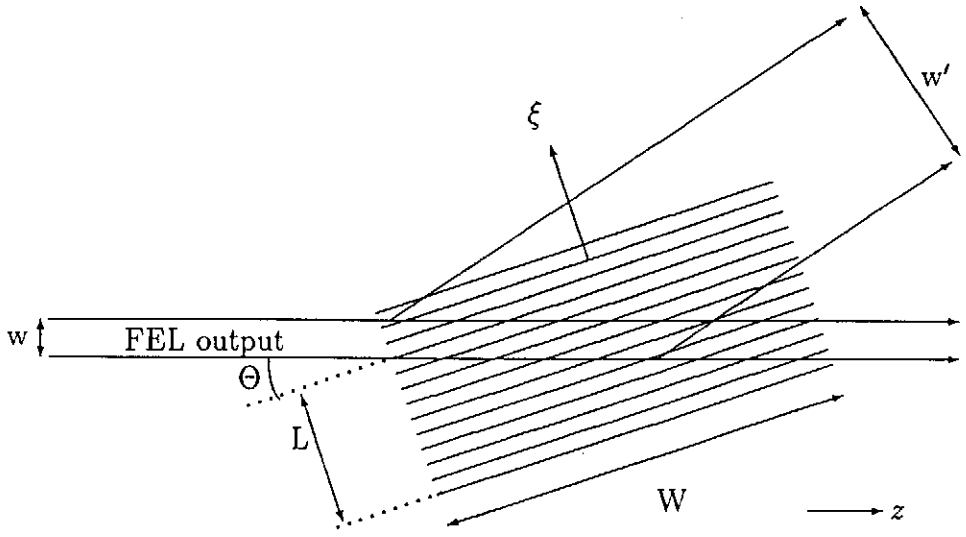

Fig. 2. Schematic of the Bragg scattering. Θ is the Bragg angle. The atomic beam passes through the paper plane at a right angle.

furthermore [1] : $\sigma = \cos 2\Theta$ the polarization factor, ϵ_1, ϵ_2 the dielectric constants in the density maxima and minima, respectively, $\mu = \beta\epsilon_1 + (1-\beta)\epsilon_2$ the mean dielectric constant and n the order of the Bragg reflex. The dielectric constant is given by:

$$\epsilon = r_e \rho f \lambda^2 / \pi \tag{4}$$

where ρ is the density of atoms and f is the scattering factor per atom (in number of equivalent electrons).

The reflectivity of a multilayer mirror is [8]:

$$R = \left| \frac{(B_n\sigma/2)\tanh(2\pi\ell L x/\lambda^2)}{b_n \tanh(2\pi\ell L x/\lambda^2) - ix} \right|^2 \tag{5}$$

where $B_n = 2(\epsilon_1 - \epsilon_2)\sin\pi n\beta/(\pi n), b_n = ((n\lambda)/(2\ell))^2 + 1 - \mu - \sin^2\Theta$ and $x = \sqrt{B_n^2\sigma^2/4 - b_n^2}$. This reflectivity needs some discussion: The relevant issue is the intensity that can be coupled back to the FEL input into a spot size that is comparable to the beam diameter and into a solid angle that is comparable to the intrinsic beam divergence of the TEM_{00} mode. To achieve optimum feedback, it is necessary to focus the reflected beam, especially so if the reflected beam is wider than the incident beam, as shown in fig. 2. As long

[1] [8] defines Θ relative to the multilayer surface normal, the definition used here conforms with the way that Θ is used in x-ray crystallography

as the FEL beam has full transverse coherence (i.e. contains only the TEM_{00} mode and if the longitudinal coherence length exceeds $W \cdot \sin\Theta$, see [9]), there is full coherence in the focus. In that case, eq. (5) may be used to calculate the reflectivity.

Now we turn to the monochromatizing properties of the atomic lattice. The energy bandwidth of the Bragg reflection is given by the extension L of the scattering volume in the direction of the scattering vector. By use of the Scherrer equation and the Bragg law, we obtain

$$\Delta\omega/\omega = -\lambda/(L\sin\Theta) \tag{6}$$

There is some spatial variation of the incidence angle due to a divergence of the FEL output and possibly due to a curvature of the atomic lattice if it is used for focusing. The energy shift of the Bragg reflection due to a deviation $\Delta\Theta$ from the nominal Bragg angle is:

$$\Delta\omega/\omega = -\Delta\Theta/\tan\Theta \tag{7}$$

Finally, we look at the recoil energy. A photon that is scattered from a free atom is slightly red-shifted due to loss of $E_R = 2\hbar^2 k_x^2 \sin^2\Theta/m$ where k_x is the wave number of the x-rays and 2Θ is the scattering angle. In our case the atoms are bound and can transfer momentum from the x-ray photons to the laser light field. If the spacing of the vibrational energy levels is larger than E_R the scattering is fully elastic. At high incident intensities, several x-ray photons are scattered from one atom and the spacing of the vibrational levels must be correspondingly larger.

5 Example

Let us now look at an example, using the TTF FEL with the following parameters: We tune the FEL to 150eV (λ = 8.6nm). The intrinsic frequency bandwidth of the TTF FEL is $\Delta\omega/\omega \approx 5 \cdot 10^{-3}$ [10]. The TTF FEL has a jitter of 300μm of the macropulse position which is larger than the macropulse length itself. In order to insure amplification in the feedback loop, we have to monochromatize to get a coherence length of 300μm, giving an energy bandpass of $\Delta\omega/\omega \approx 3 \cdot 10^{-5}$. For the atomic lattice, we take Cs atoms at a mean atom density of 10^{16} atoms per cm^3, bound by light of λ_ℓ = 852nm, incident at a flux of 2.2mW per cm^2. This wavelength corresponds to the $6S_{1/2}(F = 4) \rightarrow 6P_{3/2}(F' = 5)$ transition in Cs. Its natural linewidth is $\gamma_\ell/2\pi$ = 5.2Mhz. At the flux of 2.2mW/cm^2, the resonant Rabi frequency is $\Omega_R = \gamma_\ell$ [2]. The theory of light bound atomic lattices which was sketched

above applies to transitions from $J = 1/2 \rightarrow J = 3/2$. It is shown in [11] for Rb that the six hyperfine levels of the D2 line in Rb can be reduced to that simple picture with an effective Rabi frequency. Similarly, we use an effective Rabi frequency in Cs. We detune by $\delta = 10\gamma$. The potential energy is $U_0 = -7.15 \cdot 10^{-10}$eV.

At the chosen FEL wavelength, Cs has atomic scattering factors $f_1 = 34.9$ and $f_2 = 5.75$ [12]. We use the lowest order reflex of the atomic lattice which has a Bragg angle of $\Theta = 9.69$mrad. At that reflex order, the recoil energy is $E_R = 3.4 \cdot 10^{-11}$eV. This less than U_0 so that single x-ray photons are scattered elastically from the atoms. Even if there is a loss of recoil energy due to scattering of several x-ray photons from one atom, this loss is negligible in comparison to the width $1.5 \cdot 10^{-2}$eV of the monochromatization in the feedback loop.

By eq. (3), we calculate $\delta x = 45$nm, i.e. $\beta = 0.105$. At a mean atom density of 10^{16} atoms per cm^3, we now get by eq. (4): $\epsilon_1 = 1 - 2.14 \cdot 10^{-8} - i \cdot 3.52 \cdot 10^{-9}$ and due to the localization of the atoms $|\epsilon_2 - 1| \ll |\epsilon_1 - 1|$. Approximating $\epsilon_2 = 0$, we have in eq. (5) $x = \epsilon_1 \sqrt{(\sin(\beta\pi)/\pi)^2 - \beta^2} \approx 0.02\epsilon_1$. The density of 10^{16} per cm^3 is 4 orders of magnitude higher than in present day atomic lattices. Some technological development is still necessary both in production of such a dense atomic beam and in the generation of atomic lattices in it.

At $\lambda_\ell = 852$nm, we have $\ell = 426$nm. We choose the width of the atomic beam to be $P = 100$mm, giving $L = 1$mm. We may approximate $\tanh(x\ell L/\lambda^2)$ in eq. (5) by $x\ell L/\lambda^2$. Furthermore, $2b_1\pi L\ell/\lambda^2 \ll 1$. Therefore, the term $-ix$ is dominant in the denominator of eq. (5).

Equation (5) now simplifies to:

$$R \approx \left|2(\epsilon_1 - 1)\sin(\pi\beta)\ell L/\lambda^2\right|^2 \tag{8}$$

which gives $R \approx 7.7 \cdot 10^{-3}$.

According to eq. (6), the relative energy bandpass of the atomic lattice in our example is $\approx 10^{-3}$. The monochromatization to the required bandwidth must therefore be done by the multilayer mirrors.

With the above reflectivity and taking into account losses of 80 percent in the multilayer mirrors, the feedback is about 10^{-3} within the narrow monochromatized frequency interval. If the FEL amplifier has a gain of 10000, there is an amplification by a factor of 10 in each round trip until the FEL reaches saturation after about 3 round trips in our example and with the TTF FEL. During the rest of the bunch train there is a steady state situation with the feedback signal at the FEL entrance being about 1000 times stronger than

the shot noise within the monochromatized frequency interval and 10 times stronger than the shot noise within the total intrinsic frequency interval of the TTF FEL.

The inherent divergence of the TEM_{00} mode of the TTF FEL is $\approx$0.02mrad at $\lambda = 8.6$nm. According to eq. (7), the resulting energy spread $\Delta\omega/\omega \approx 0.002$ which is larger than the energy bandpass of the atomic lattice. In order to actually make use of the full FEL beam, the lattice planes in the atomic lattice have to be slightly curved to give the same incident angle for all parts of the FEL output beam.

Finally, we look at the regeneration of the atomic lattice. The maximum bunch repetition rate that the atomic lattice can handle is given by the time for a fresh part of the atomic beam to enter the FEL beam of 0.1mm width. In a thermal atomic beam of Cs, having a speed of 220m/s at 400K, this time is about 500ns.

I gratefully acknowledge the many stimulating discussions with G. Materlik, E.L. Saldin and M.V. Yurkov.

References

[1] A. Hemmerich and T.W. Hänsch, Phys. Rev. Lett. 70 (1993) 410

[2] A. Kastberg, W.D. Phillips, S.L. Rolston, R.J.C. Spreeuw and P.S. Jessen, Phys. Rev. Lett. 74 (1995) 1542

[3] M. Kozuma, K. Nakagawa, W. and Jhe M. Ohtsu, Phys. Rev. Lett. 76 (1996) 2428

[4] C. Salomon, J. Dalibard, A. Aspect, H. Metcalf and C. Cohen-Tannoudji, Phys. Rev. Lett. 59 (1987) 1659

[5] M. Weidemüller, A. Hemmerich, A. Görlitz, T. Esslinger and T.W. Hänsch Phys. Rev. Lett. 75 (1995) 4583

[6] A. Hemmerich, M. Weidmüller, T. Esslinger, C. Zimmermann and T. Hñsch, Phys. Rev. Lett. 75 (1995), 37

[7] J.-Y. Courtois and G. Grynberg, Phys. Rev. A 46 (1992) 7060

[8] I.V. Kozhevnikov and A.V. Vinogradov, Physica Scripta T17 (1987) 137

[9] T. Salditt, H. Rhan, T.H. Metzger, J. Peisl, R. Schuster and J.P. Kotthaus, Z. Phys. B96 (1994) 227

[10] E.L. Saldin, E.A. Schneidmiller and M.V. Yurkov, DESY Internal Report TESLA-FEL 96-07, see also the contribution to this conference: E.L.

Saldin, E.A. Schneidmiller and M.V. Yurkov, Simulation Studies of 6 nm Free Electron Laser at the TESLA Test Facility Starting From Noise, contribution to the FEL96 conference

[11] A. Hemmerich, D. Schropp and T.W. Hänsch, Phys. Rev. A 44 (1991) 1910

[12] www information server of Lawrence Berkeley Laboratory: http://www-cxro-lbl.gov:80/optical_constants/

Two-Stage Amplifier Scheme with Feedback by Bragg-Reflecting Mirrors in an Å Wavelength Range FEL

B. Adams, G. Materlik

Hamburger Synchrotronstrahlungslabor HASYLAB am Deutschen Elektronensynchrotron DESY, 22607 Hamburg, Germany

We describe the principle and ways of realization of the production of longitudinally coherent radiation from an x-ray FEL. The setup consists of two FEL amplifiers, the first one in a feedback loop with Bragg-reflecting mirrors going up only to a limited power level and the second one starting with the microbunched electron pulses coming out of the first part and amplifying up to the saturation limit.

1 Introduction

One of the peculiar features of the SASE process is the irregular temporal structure of the photon beam. A much better temporal coherence can be obtained by using a two-stage FEL amplifier scheme together with a multibunch LINAC like TESLA. The first stage, operating in the linear regime, generates a longitudinally coherent microstructure on the electron beam via feedback by monochromatizing crystals. This microstructure has the effect of a coherent seed in the second stage which amplifies up to the saturation limit without any further optical components.

After the passage of several bunches, the power in the monochromatic wavelength band is sufficient to override the shot noise at the entranc of the second stage and the gain in the feedback loop can be reduced to unity to reach a steady state which is still tolerable to the Bragg crystals.

We study this idea on the basis of a set of design parameters of the TESLA FEL which is being planned at DESY. At this stage, the chosen parameters only serve to illustrate the principle.

2 The setup

Fig. 1 shows a schematic of the setup. The two FEL amplifiers are traversed in succession by a train of equidistant macropulses. The x-ray output of the first FEL amplifier is monochromatized by a Bragg-reflecting crystal in back-scattering geometry to a typical energy bandwidth of $\Delta\omega/\omega \approx 10^{-5}$. This reflected beam is reflected again by an identical crystal on the entrance side of the FEL amplifier. The wavelengths at which the feedback loop operates are therefore discrete, but slightly tunable by controlling the temperature of the crystals.

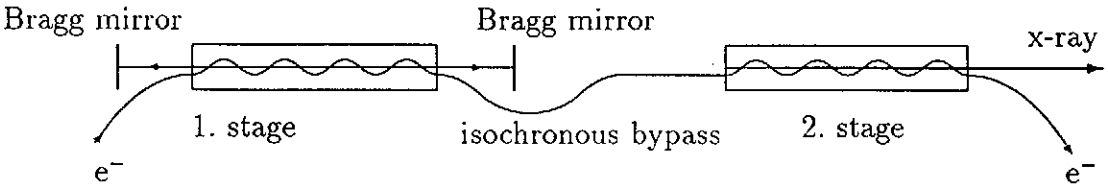

Fig. 1. Schematic of the setup

The first macropulse in a bunch train generates an x-ray output with the typical SASE coherence characteristic. The next macropulse is then seeded by the monochromatic feedback signal. Since the first amplifier operates in the linear regime, the spectrum at the entrance, containing the monochromatized peak on top of the shot noise is simply reproduced in amplified form at the output. The feedback signal in the second pass is therefore stronger, and so on with exponential growth of the monochromatized signal. At some point in this exponential curve, the gain in the feedback loop must be reduced to reach a steady state at a power level that is still tolerable to the Bragg mirrors. This reduction may be accomplished by piezo-controlled distortion of the Bragg crystals or by a switchable absorber.

After exiting from the feedback loop, the macropulses, now carrying a microbunch stucture which coherently extends over their full length, pass on through an isochronous bypass around the first Bragg mirror and enter the second FEL amplifier. There, they generate longitudinally coherent x-radiation. The degree of longitudinal coherence depends on the maximum power level that may be tolerated in the feedback loop.

In order to achieve exponential growth of the coherent signal in the feedback loop, the spectral power density of the feedback signal must be larger than that of the shot noise at the FEL entrance. This requires a gain of just a few dB in the feedback loop. However, for good longitudinal coherence, the power of the monochromatized feedback signal at the entrance of the first stage

should considerably exceed the shot noise power within the total frequency interval of the FEL. This requirement may be met even with a small gain in the feedback loop by allowing a large number of feedback round-trips before the gain reduction is activated.

The Bragg mirrors are exposed to a heat load which consists of three parts: The spontaneous synchrotron radiation from the undulator, the shot noise signal within the frequency interval of the FEL, amplified by one passage through the first stage and the absorbed part of the multiply amplified coherent signal. Both crystals are exposed to the latter part while the former parts are incident only on the downstream crystal.

The monochromatization of the crystals can be estimated by the ratio λ/ℓ where λ is the x-ray wavelength and ℓ is the extinction length, given by [1]:

$$\ell = \frac{2V}{r_e \lambda F} \tag{1}$$

V is the unit cell volume, r_e the classical electron radius and F is the unit cell scattering factor.

3 Example

We now take the example of the TESLA FEL which is being planned at DESY for an x-ray wavelength of 0.98Å.

In order to obtain good transverse coherence of the x-ray beam in the feedback loop, the first FEL amplifier must have a diffraction parameter below about 10 [2]. This means that its amplification must be at least 20dB. We choose a length of 20m for the first undulator which gives us the required gain. Fig. 2 shows the directional dependence of the intensity at the output of the first undulator. The power that is fed back to the input does not influence the shapes, but only the intensity scale. [2].

The Bragg mirrors are Si crystals, used in backscattering geometry with the (775) reflection. By eq. (1) we get a monochromatization of $\Delta\omega/\omega \approx 10^{-5}$. We place the crystals 140m apart with the downstream one at a distance of 100m from the exit of the first undulator. In order to match the round trip time between the crystals, we let every 10th bunch from the TESLA bunch train pass through the FEL, giving a bunch-to-bunch spacing of about 930ns [5]. The FEL parameters are summarized in tab. 1.

We now consider the heat load on the Bragg crystals. The downstream crys-

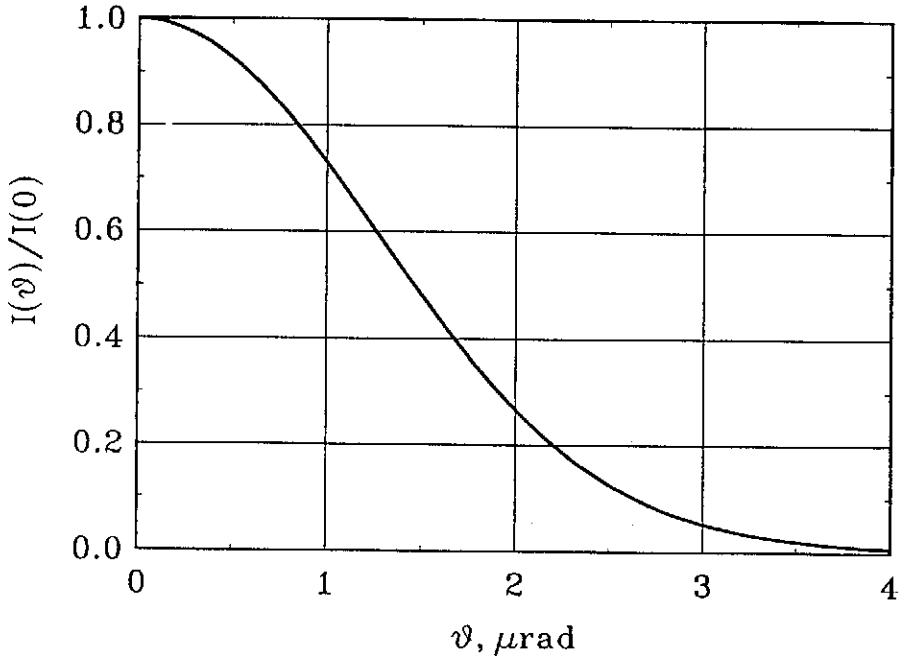

Fig. 2. Intensity at the output of the first undulator as a function of the deviation from the beam direction [2].

electron beam energy	36GeV
electron peak current	5kA
bunch train length	1.05 ms
beam current, averaged over bunch train	12 mA
emittance	1 mrad mm
λ	0.98Å
undulator period, helical	5cm
external beta function	10m
undulator field	0.95T
undulator parameter K	4.45
lenght of the first undulator	20m
x-ray beam diameter at the exit of the first stage	10μm
diffraction parameter in the first stage	7.8

Table 1
Summary of the FEL parameters in the example [2,5]

tal is exposed to synchrotron radiation, the shot-noise initiated output of the FEL within a frequency interval of about 10^{-3} and to the multiply amplified coherent signal. Only the latter contribution is incident on the upstream crystal. From present experience with synchrotron radiation crystal optics, we

expect that crystal arrangements can be made to withstand a total power of a few 100mW within the x-ray beam diameter of about 20μm and incident within the time interval of one bunch train. This amounts to an energy of several 100nJ, deposited by one 80fs-flash from the FEL in a volume of about $(20\mu m)^3$ (beam cross section times typical absorption depth). This is less by several orders of magnitude than the amount of energy needed to generate a plasma by ionizing the Si atoms in this volume. It is therefore justified to treat the heat load in terms of heat conductivity and heat capacity.

The largest part of the heat load on the downstream crystal comes from the spontaneous synchrotron radiation which is given by [4]:

$$P[kW] = 0.633 E^2[GeV] B^2[T] L[m] I[A] \qquad (2)$$

and is emitted into a divergence of approximately $1/\gamma$. With the parameters from table 1 and using every 10th bunch from the bunch train, this gives about 18kW into a divergence of about 14μrad, i.e. approximately 10 times more than the divergence of the coherent beam from the first undulator (see fig. 2). We place the downstream crystal 100m away from the undulator and put a pinhole of 20μm diameter in front of it. This reduces the power in the synchrotron radiation to about 4W. Of this, the part in the spectrum above several 10keV is almost not absorbed at all in Si of some mm thickness. For further reduction of the heat load, a suitably chosen absorber can be placed in front of the downstream crystal to cut off the low energy part of the spectrum (below some keV). Thereby, the heat load due to synchrotron radiation can be kept well below one W.

The pinhole has another advantageous effect. Since the divergence of the FEL beam is about 1.5μrad, the pinhole at a distance of 100m lets only about 1/50 of it pass through. This reduces the gain of the feedback within the monochromatization band to about 3dB, making the exponential growth slower and thus easier to control.

The frequency interval of the TESLA FEL with the above parameters is $\Delta\omega/\omega \approx 10^{-3}$ [2]. The shot noise power within that frequency interval is approximately 10kW [2,3]. For good longitudinal coherence, we feed back a peak power of 100kW in the steady state. The TESLA FEL will have a bunch length of approximately 80fs and a bunch-to-bunch spacing of approximately 930ns (using every 10th bunch) [5]. Averaging the power due to the coherent signal over one bunch train, this amounts to about 8mW of which 1/50 passes through the pin hole. Most of that is reflected and not absorbed. Finally, the contribution of the FEL beam outside of the monochromatization interval is 0.8mW time-averaged shot noise power at the entrance of the first undulator, amplified by 3dB (20dB due to the undulator minus 17dB due to the pinhole).

Fig. 3 shows the power in the second undulator over its length if a pre-microbunched bunch from the first undulator enters it.

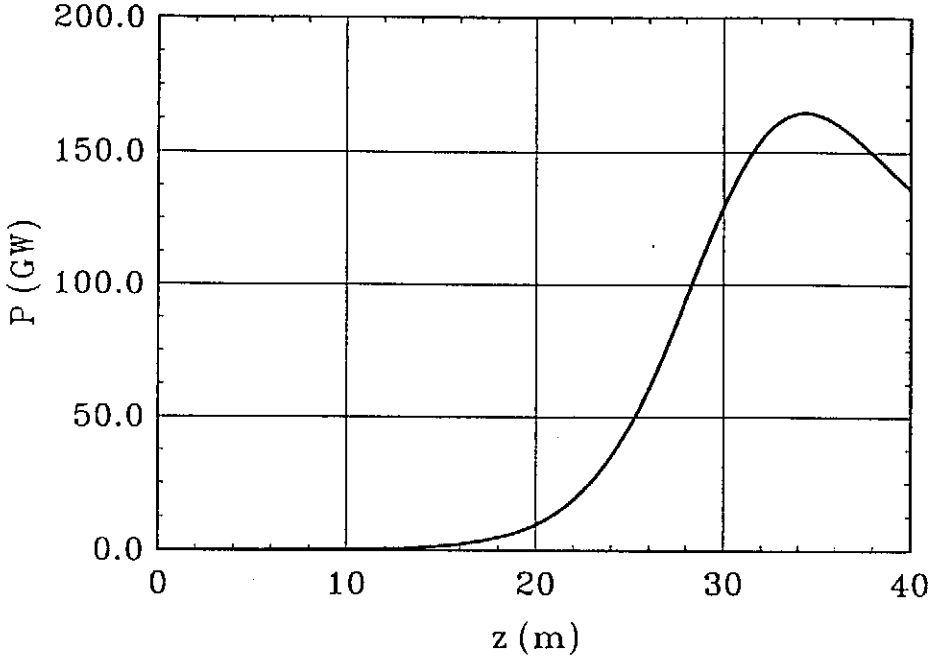

Fig. 3. Power in the second undulator, plotted over its length after a bunch has obtained a coherent pre-microbunching in the feedback loop [2].

4 Discussion

To summarize, the crucial point is not the power of the coherent signal in the feedback loop but the synchrotron radiation from the undulator which is incident on the downstream crystal. The upstream crystal is exposed to a much smaller heat load. The feedback peak power of 100kW in our example is therefore not the limit of what is possible - it is simply sufficient to obtain good longitudinal coherence in the output of the first FEL amplifier.

The heat load due to synchrotron radiation may increase for several reasons: If an electron beam of higher energy than in our example is used (see eq. 2) or if it becomes necessary to enlarge the pinhole or if more than only every 10th bunch is used. In these cases, several means of reducing the heat load seem feasible: The Si crystals may be cut asymmetrically to the scattering vector. Thereby, the heat load is spread over a much larger surface. In order to prevent a distortion of the wavefronts in the feedback, both crystals have to have equal asymmetry angles. It might also be possible to use rotating crystals to spread the heat load over a large area.

It might be desirable to use a part of the radiation in the feedback loop. This

may be accomplished by either using a Bragg crystal which is not thick in comparison to the extinction length (this would preferably be the upstream one), making it semi-transparent to the x-rays or by exploiting multiple Bragg reflexes which are quite common especially in backscattering geometry. Besides the backscattered beam, other beams are reflected from the crystal at different angles, making them accessible to diagnostics and further experiments.

References

[1] B. Batterman, H. Cole, Rev. Mod. Phys. 36 (1964), 681

[2] E.L. Saldin, M.V. Yurkov, private communication

[3] E.L. Saldin, E.A. Schneidmiller and M.V. Yurkov, Phys. Rep. 260 (1995), Nos. 4 and 5

[4] X-ray Data Booklet, Lawrence Berkeley Laboratory, PUB-490, April 1986

[5] J. Rossbach, Design parameters of the TESLA FEL, http://www.desy.de/pub/hasylab/xfelross.html

Presented at the XVIII FEL Conference, Rome, Italy

Parameter Study on Phase I of the VUV-FEL at the TESLA Test Facility

W. Brefeld[a], B. Faatz[a], Y.M. Nikitina[a], J. Pflüger[a], P. Pierini[b], J. Roßbach[a], E.L. Saldin[c], E.A. Schneidmiller[c] and M.V. Yurkov[d]

[a]Deutsches Elektronen Synchrotron DESY, Notkestr. 85, 22603 Hamburg, Germany
[b]INFN Milano - LASA, Via Cervi, 201,20090 Segrate (MI), Italy
[c]Automatic Systems Corporation, Samara, Russia
[d]Joint Institute for Nuclear Research, Dubna, Russia

ABSTRACT

Currently, a SASE-FEL in the VUV, driven by the TESLA Test Facility accelerator, is under construction at DESY. As a first phase of the project, three of the eight TTF accelerator modules will be installed to deliver an electron beam with a nominal energy of approximately 390 MeV with a peak current of 500 A. With this energy, employing an undulator with the same parameters as for the final design, the resonant wavelength is around 44 nm. For this wavelength, the transverse beam emittance and energy spread conditions can be relaxed as compared to the design wavelength of 6 nm in the final stage. The proposed length of the planar undulator with the integrated FODO lattice is about 15 m.
In this paper, we present a detailed study on how the performance around 300 MeV depends on the electron beam and undulator parameters. Also, the status of the project is briefly sketched.

1. Introduction

At Deutsches Elektronen-Synchrotron (DESY), a large effort is dedicated to build a Free Electron Laser (FEL) starting up from noise, i.e., in the so-called Self Amplified Spontaneous Emission (SASE) mode [1-2]. The superconducting (s.c.) accelerator will, in its final stage, deliver an electron beam with an energy of 1 GeV. In its first stage, however, only part of the accelerator will be built to obtain an energy up to 390 MeV. First experiments are planned at an energy of 300 MeV, corresponding to a wavelength of 70 nm, with a peak current of 500 A. For this stage, a 15 m long undulator will be built. The layout of the experiment is shown in Fig. 2.1, with parameters given in Table 2.1. For the final stage, the accelerator is extended to 1 GeV and the undulator to the full length of about 30 m (see Ref. [3] for more details), radiating at a wavelength of 6 nm. Several studies of the final stage of the design have already been published (see for example [4]).

There are two objectives of stage I of this project. First, to study the operation of the different components, such as the high-gradient s.c. accelerator. The second aim is a first prove of principle of a SASE FEL in this energy range. Because of the larger wavelength, demands on both energy spread and transverse emittance can be relaxed. Since the device is optimized for operation at higher electron energy, it is not a main goal to reach saturation. This is, however, not essential for the prove of principle of SASE. The main goal is to be well within the exponential gain regime. With the same undulator geometry used for stage I and for the final FEL, the variation in β-function due to the superimposed FODO-structure is 3.15 at 300 MeV (see Table 2.1). Influence of magnetic field errors and the geometrical tolerances of the different modules on the gain are presented in separate contributions [5-6].
In this paper, results of simulations are shown using the preliminary results of beam parameters of the accelerator system up to the undulator entrance.

2. FEL performance

The design parameters of Phase I of the SASE FEL at DESY are given in Table 2.1. There are limited possibilities to tune the focusing system of the undulator. The exact values of the emittance and the energy spread in the electron beam will be available only after commissioning the accelerator. Therefore, it is reasonable to study the FEL performance in the vicinity of these project parameters. For quick estimations of the region of parameters we have used analytical techniques [7-8] and comprehensive calculations have been performed with TDA-3D [9]. Optimized parameters are assumed for the FODO-lattice which differ slightly from the ones previously presented. This is due to a more detailed knowledge concerning undulator design, and the diagnostics between undulator modules. A different compression ratio in the second bunch compressor (see Ref. 1) has been chosen, resulting in a 20% decrease in peak

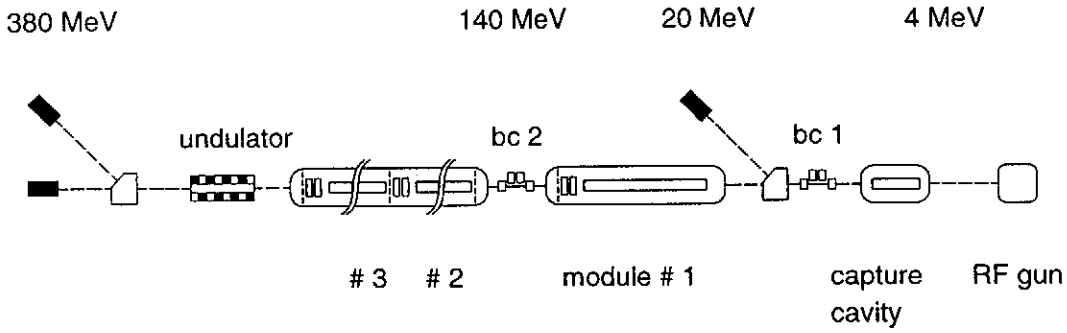

Figure 2.1: *Layout of the TTF-FEL for stage I.*

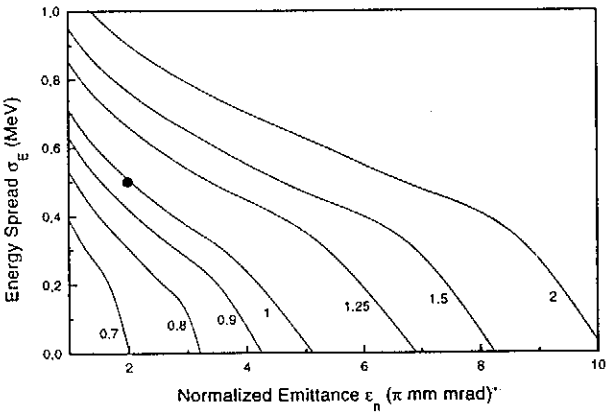

Figure 2.2: *Ratio of the gain length and the reference field gain length given in Table 2.1 for different values of the normalized emittance and energy spread.*

current. In addition to this, results are different compared to earlier simulations, because so-far, the variation in β-function was not included [7]. As a consequence of this variation, the saturation length is longer and the power is smaller in the simulations presented in this paper.

2.1. Phase Space Dependence

In Fig. 2.2 we present the results of analytical calculations of the field gain length dependence on the energy spread and the emittance of the electron beam. Analysis of these plots shows that there are no significant perspectives to improve the FEL parameters, the best case (emittance down to 1 π mm mrad and the energy spread down to 100 keV) will only reduce of the saturation length by 30 %.
In Fig. 2.3, the saturation length and the saturation power, calculated with TDA, are shown as function of the normalized emittance. Note that the saturation length is given in terms of a reduced length,

Electron beam	
Energy	300 MeV
Peak current	500 A
Normalized rms emittance	2π mm mrad
rms energy spread	0.17 %
External $\overline{\beta}$-function	1 m
β_{max}/β_{min}	3.15
average beam size	57 μm
Undulator	
Type	Planar
Period	27.3 mm
Peak magnetic field	0.497 T
Magnetic gap	12 mm
Undulator section length	4.5 m
Number of sections	3
FODO-lattice	
Period	0.9555 m
Quadrupole length	0.1365 m
Quadrupole strength	18.3 T/m
Radiation	
Wavelength	71.42 nm
Field gain length	1.2 m
bandwidth	$\pm$0.5%
Output power	220 MW

Table 2.1: *Simulation Parameters used for phase I of the TTF VUV-FEL*

i.e., the total length minus the total drift length between undulator modules. The total reduced length of the intended three modules is 13.5 m, the reduced length of 6 modules is slightly less than 27 m. As can be seen, for the design values given in Table 2.1, the FEL barely reaches saturation. The behaviour is similar to that obtained with previous calculations.

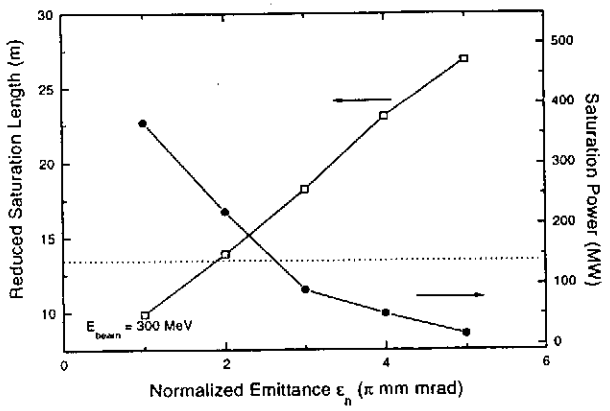

Figure 2.3: *Saturation power (solid symbols) and saturation length (open symbols) versus normalized emittance. The undulator length for phase I is indicated by the dotted line. All remaining parameters are listed in Table 2.1*

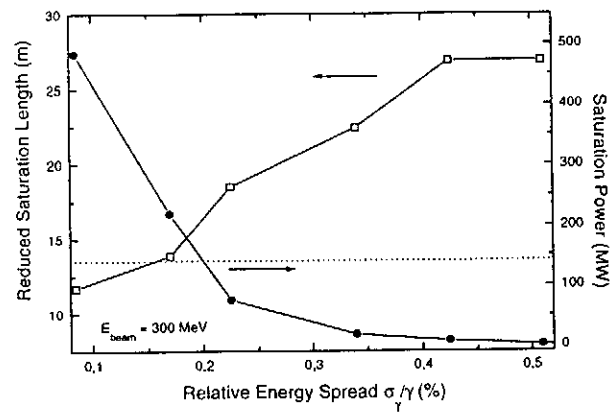

Figure 2.4: *Saturation power (solid symbols) and saturation length (open symbols) versus energy spread. The dotted line indicates the anticipated undulator length for phase I. All remaining parameters are listed in Table 2.1*

The increase in saturation length and decrease in power is a result of the large variation in β and due to diffraction of the field in the field-free gaps.
In Fig. 2.4, the influence of energy spread on both saturation power and (reduced) saturation length is shown. For large energy spread, the saturation length does not increase, because the calculations have not been extended beyond the maximum of six undulator modules. Thus, for a relative energy spread up to 0.17%, the power saturates within the three undulator modules employed in stage I. For an energy spread smaller than 0.4%, the radiation field reaches saturation within the undulator length in the final design at a power level of only 10 MW. All results are in good agreement with analytical results, taking into account the large variation of β, of which the influence will be discussed next.

2.2. Variation of the β-function

Each FODO cell consists of 136.5 mm long quadrupole magnets and 341 mm long focusing free sections. They are needed to provide a smooth FODO lattice running over the intersections between two adjacent modules. Between the three modules planned for phase I, some additional diagnostics is needed. Due to the large phase advance per FODO-period at 300 MeV, there is a large variation in β-function, and therefore a large variation in velocity spread. This increases the gain length.
The undulator design is optimized for an electron beam energy of 1 GeV. With the emittance and electron beam radius given in Table 2.1, the average β-function at this energy is 3 m, with $\beta_{\max}/\beta_{\min} = 1.36$. In general, the variation in β can be approximated by

$$\frac{\beta_{\max}}{\beta_{\min}} = \frac{2+\phi}{2-\phi} \quad \text{with} \quad \phi = \frac{L_{\mathrm{FODO}}}{\overline{\beta}},$$

where the angle ϕ is the phase advance per FODO-cell in radians. Because the same undulator geometry is used at 300 MeV, the phase advance per FODO cell, and therefore the β beat, is much larger. For the values given in Table 2.1, $\beta_{\max}/\beta_{\min} \approx 3$. The β-function is shown in Fig. 2.5.
In Fig. 2.6, the influence of a change in average β-function on saturation length and power is shown. Because the gap between undulator modules and the length of quadrupoles have to remain fixed in order to maintain a smooth β-function between modules, the β-function is varied by changing the quadrupole strength. Because this also changes the ratio $\beta_{\max}/\beta_{\min}$, the optimum for the average value of β compared to previous calculations is larger. For the present FODO-design, this ratio is 3.15 for 300 MeV. It increases to 6 for the smallest β-function investigated (with $Q = 25T/m$), and reduces to 1.33 for the largest β-function. Therefore, the gain is reduced for large β due to the small current density, and for small β due to large velocity spread. Simulations for an almost constant β-function of 0.9 m, realized here by an appropriate change of the FODO lattice, give a (reduced) saturation length of 12 m, with a corresponding power of 500 MW.

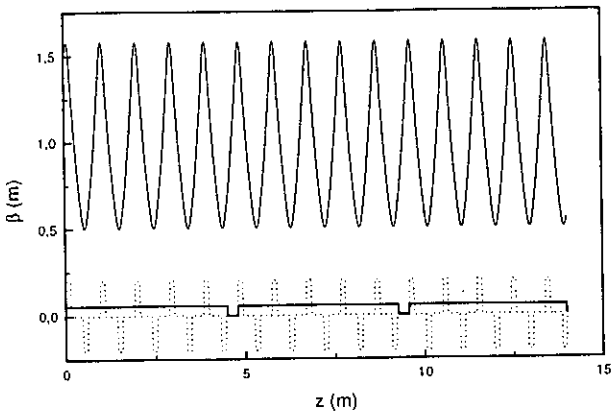

Figure 2.5: *β_x-function along the undulator for the values given in Table 2.1. The thick solid line at the bottom indicates the three undulator modules with the 300 mm long gaps, the dotted line the superimposed FODO-lattice.*

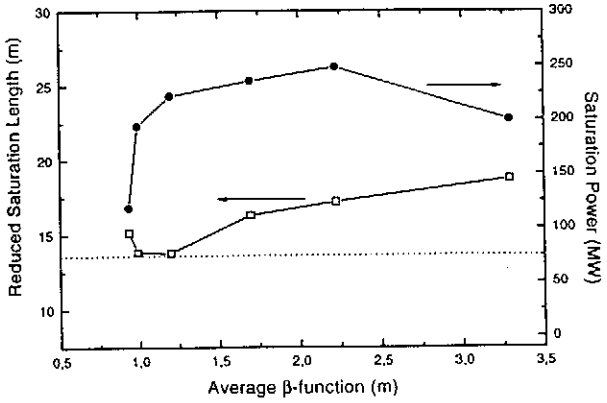

Figure 2.6: *Saturation power (solid symbols) and saturation length (open symbols) for different values of the β-function. The quadrupole gradient has been varied between 25 and 5 T/m as well as the initial Twiss-parameters in order to match the beam. The dotted line indicates the anticipated length of the undulator for phase I. All other parameters are as in Table 2.1*

3. Conclusions and Discussion

Results of simulations have shown that saturation can be reached within the three undulator modules. For the present FODO-period, decreasing the β-function by increasing the quadrupole strength does not decrease the saturation length. This could only be achieved by changing the FODO-period. Choosing a variable FODO-period is presently under investigation. If either energy spread or normalized transverse emittance are larger than the reference values saturation is not reached within the three undulator modules. In view of the main objectives of phase I as mentioned above, such situation would be tolerable, however.

At present, several components have already been built. The electron gun has undergone its first cold tests, with very promising results. A first s.c. accelerating section will be installed in fall; acceleration of the injector beam is expected by the end of this year. A complete 120-200 MeV module containing 8 s.c. cavities will be assembled until early next year, and is going to be installed in the beam line in spring 1997. The two first bunch compressors have been designed. For phase I, the increase of slice emittance due to coherent radiation in the compressors is small, while the over-all emittance growth is substantial but still tolerable [10]. For the final design of the third bunch compressor, studies are still ongoing. Another two accelerating modules with 8 s.c. cavities each will be build next year. Further details can be found in Ref. [11]. Mechanical tests on a first 220 mm long undulator module have been performed. A 0.8 m long prototype for field measurements is expected before the end of this year (see Ref. 3).

Acknowledgement: We would like to thank K. Flöttmann, T. Limberg and H. Weise for their contributions to this work.

References

1. "A VUV Free Electron Laser at the TESLA Test Facility: Conceptual Design Report", DESY Print TESLA-FEL 95-03, Hamburg, DESY, 1995.
2. J. Roßbach, *Nucl. Instr. Meth.* **A375** (1996) 269.
3. J. Pflüger, Y.M. Nikitina, B. Faatz and T. Teichmann, *The undulator system for the VUV-FEL at the TESLA Test Facility*, presented at this conference.
4. W. Brefeld et. al. Nucl. Instr. Meth. **A375** (1996) 295.
5. B. Faatz, J. Pflüger and Yu.M. Nikitina, *Study of the Undulator Specifications for the VUV-FEL at the TESLA Test Facility*, presented at this conference.
6. B. Faatz, J. Pflüger and Yu.M. Nikitina, *Geometrical Undulator Tolerances for the VUV-FEL at the TESLA Test Facility*, presented at this conference.

7. E.L. Saldin, E.A. Schneidmiller and M.V. Yurkov, DESY Print TESLA-FEL 95-02.

8. E.L. Saldin, E.A. Schneidmiller and M.V. Yurkov, Phys. Rep. **260**(1995)187.

9. T.-M. Tran and J.S. Wurtele, *Comp. Phys. Commun.* **54** (1989) 263; P. Jha and J.S. Wurtele, *Nucl. Instr. and Meth.* **A331** (1993) 477.

10. T. Limberg, presented at this conference.

11. H. Weise, for the TESLA collaboration, *Status of the TESLA Test Facility Linac*, XVIII International Linac Conference, Geneva, Switzerland, 1996.

AN X-RAY FEL LABORATORY AS PART OF A LINEAR COLLIDER DESIGN

R. Brinkmann, G. Materlik, J. Rossbach[1], J.R. Schneider, B.-H. Wiik

Deutsches Elektronen-Synchrotron DESY, Notkestr. 85,
D 22603 Hamburg, Germany

Abstract

This paper presents an X-ray Free Electron Laser laboratory (XFEL for short) as part of a Linear Collider facility. After presenting the over-all scheme, we discuss the advantage of using a low RF frequency linac (preferably a superconducting one) as the driver of an XFEL. The parameter range with respect to pulse structure, photon wavelength and brilliance values is presented as well as schemes of distributing the train of several thousand electron bunches per rf pulse to many different users. Main technical challenges and proposed solutions are discussed.

PROOFS:
J. Rossbach
DESY -MPY-
Notkestr. 85
D 22603 Hamburg
Germany
Tel.: +49 40 8998 3617
FAX: +49 40 8994 4305
e-mail: rossbach@desy.de

We O3 Presented at the 17th International Free Electron Laser Conference,
August 26 - 30, 1996, Roma, Italy

[1] corresponding author

1. INTRODUCTION

a) X-ray FELs

Due to the progress of accelerator technology during recent years it now seems possible construct a Free Electron Laser (FEL) that provides coherent radiation at wavelengths very far below the visible: This laser makes use of the principle of Self-Amplified-Spontaneous-Emission (=SASE), which does not require the optical cavity resonator normally used in multi-pass, longer wavelength FELs and can hence in principle deliver light with wavelengths in the Angstrom regime. Compared to state-of-the-art synchrotron radiation sources, one expects a transversely fully coherent beam, larger average brilliance, and, in particular, a pulse lengths of about 200 fs FWHM with eight or more orders of magnitude larger peak brilliance. The peak power is around the 10 GW level. As the SASE FEL is completely independent of atomic excitation levels, it can be tuned over a wide range in wavelengths.

b) Linear Colliders

There is a consensus within the particle physics community that measurements of the $e^+ e^-$ annihilation process should be extended to energies beyond these available at LEP. There is also agreement that this can only be achieved using a linear collider facility, which consists of a pair of linear accelerators directed against each other to accelerate and collide well focused high energy beams of electron and positrons. Based on theoretical studies and on experimental work it now seems feasible to construct such a facility for center-of-mass energies up to 500 GeV. A large R&D effort including the construction of test facilites is now under way at several laboratories including CERN, DESY, KEK and SLAC. It is expected that this work will lead to a proposal for a linear collider facility by year 2000.

In order to achieve sufficiently high counting rates for high energy physics, extremely small beam sizes and very large average beam power are mandatory for these machines. These are features which make Linear Collider beams and related technology most attractive for the next generation synchrotron radiation sources, aiming at diffraction limited beam sizes down to the Angstrom range wavelengths.

Based on the understanding that a linac driven X-ray Free Electron Laser (XFEL for short in this paper) could utilize a Linear Collider installation without mutual interference, this paper sketches an XFEL as part of a Linear Collider scenario.

2. OVER-ALL DESIGN

The different linac concepts considered by linear collider study groups mainly differ with respect to the choice of rf frequency. Roughly speaking, larger rf frequencies (up to 30 GHz) offer a higher accelerating gradient, i.e. a shorter over-all tunnel length, at the price of reduced power efficiency and worse beam energy distribution. In contrast, low frequency linacs (down to 1.3 GHz for the superconducting TESLA linac) promise very good beam quality, because each electron bunch extracts only a small fraction of the large energy that is stored in the big cavity volume (small 'wakefield' effects). At DESY, linear

collider studies are focused on this low frequency type[1]: the normalconducting S-Band Linear Collider (SBLC) operating at 3 GHz like the SLAC linac, and the TeV Superconducting Linear Accelerator (TESLA). Test facilities[3,4] for both versions are now under construction at DESY within the framework of international collaborations. The TESLA Test Facility (TTF) also includes a rf photocathode gun, a bunch compression system and an undulator which will enable us to verify and study the SASE-FEL mechanism at wavelengths of less than 100 μm. A project to upgrade the test facility to achieve photons with wavelengths down to 6 nm has been approved.

For an XFEL the highest priority is electron beam quality and large average beam current, while high accelerating gradient might be of minor importance. Thus there is a clear preference of low frequency linacs. With respect to longitudinal wakefields of 200 fs long bunches this preference is based on generally accepted scaling rules, because no experimental experience is available yet, and work is under progress to improve the understanding.

In order to make the full energy of the linac available for synchrotron radiation research, the XFEL laboratory building must be placed close to the collider interaction region. The electron beam is extracted from the regular acceleration structure at the desired energy level and then transferred by a beam transport line parallel to the linac, until it is deflected into the X-ray experimental hall(s), see Figure 1. Many such extraction lines can be built in parallel, so that various beam energies can be made available in the X-ray lab quasi-simultaneously. At the end, these beams are deflected into a small diameter, low cost tunnel pipe which separates the beams from the linac tunnel and directs them into the X-ray lab. While the linac tunnel is about 20 meters below ground, there is no problem to build this X-ray lab on the ground surface or at a more moderate depth. At the end of the extraction tunnel, a beam switchyard is foreseen distributing the beams to different undulators, see Figure 2.

3. PULSE STRUCTURE

Due to the large accelerating gradient foreseen, only pulsed rf operation is possible for both technical and economical reasons. Thus, the electron pulse structure consists of trains of electron bunches, repeated at the linac repetition rate f_{rep} , which is 5 Hz for TESLA and 50 Hz for SBLC. It is proposed to run in an interleaved pulse mode, where rf pulses for high energy physics and those for X-ray physics alternate, as shown in Figure 3 for the TESLA case. The advantage is that there is minimum interference between beam properties for high energy physics and X-ray physics, and that all kicker magnets required to switch beamlines can be made slow. In particular, the beam energy of the X-ray pulse in each extraction line can be varied from pulse to pulse (within a reasonable range mainly determined by the tuning speed of the extraction beamline magnets) and is independent of the required collider energy. In principle, both pulse length and repetition rate of the X-ray pulse could be increased within a certain limit, but one should keep in mind that, already in this scheme, the *average* electron beam power of the X-ray pulse alone is of the order of 1 MW, resulting in AC power consumption of some 10 MW, see Table 1. In the context of power efficiency it is certainly an advantage of TESLA that the AC power for compensation of the static cryogenic losses have to be invested anyway for the high energy pulse, so that the overall power efficiency for the X-ray pulse can be made as large as 28 % [5]. This optimum efficiency occurs at 18 MV/m accelerating gradient, but the optimum is quite broad, as seen from Figure 4.

Inside the pulse train there is considerable flexibility in choosing the bunch-to-bunch spacing, the fundamental limitation only given by the rf bucket length of less than a nanosecond. However there is a tendency that TESLA favors a much larger bunch spacing than SBLC, because the long rf filling time of superconducting cavities calls for comparatively long rf pulses with small pulse current. The bunch train distribution among different undulators can be done by either fast kicker magnets, by deflecting-mode-cavities synchronized with the accelerating rf, or by subharmonic cavities followed by a dispersive section. Each of these systems has different capabilities with respect to the pulse structure delivered to the respective users, so the choice will be made depending on the user requirements. Naturally, the procedure of bunch train distribution reduces the average brilliance to be generated by each undulator, but the peak brilliance remains untouched. Note also that even if the pulse train is distributed among (say) 20 undulators, the average brilliance from *each* undulator will still be three or more orders of magnitude higher than at present state-of-the-art 3rd generation synchrotron radiation sources.

4. ELECTRON BEAM PARAMETERS

While the electron beam size delivered from a radiation damping storage ring perfectly matches the requirements on the high energy physics pulse, such a beam cannot be utilized for an XFEL. A beam with smaller horizontal emittance and much smaller longitudinal emittance is required. Such a beam can be provided by an rf photocathode gun. With the present state of technology of rf guns[6], an XFEL could be made operating in the few nanometer range. Anticipating improvements in gun performance by about a factor of 3, a normalized emittance of $\varepsilon_n = 1\ \pi$ mrad mm (for 1nC bunch charge) seems to be feasible. It is important to understand that in a linac the *normalized* emittance is a conserved quantity, so that the *geometrical* emittance ε (which determines the diffraction limit) decreases linearly with energy: $\varepsilon = \varepsilon_n/\gamma$, γ being the relativistic factor. In contrast, the geometrical emittance of a storage ring (not determined by initial conditions but by quantum fluctuation effects) *increases* with the square of the energy for any particular magnet lattice. This tendency makes generation of high-energy, low-emittance beams in storage rings indeed difficult.

In order to achieve laser saturation within a single passage, XFELs require electron pulse currents of few kiloamperes. Because of space charge effects, such high currents cannot be generated directly from the rf gun cathode without blowing up the transverse emittance. Instead, a 7 ps long, 120 A beam is produced, accelerated, and longitudinally compressed by a factor of 40. This compression takes place in several steps at different energies. Bunch compressors are beam line sections which longitudinally compress the bunch using path length differences in a magnetic chicane. This is a well established technique, but has not yet been realized with extremely brilliant electron beams. Although simple in first-order theory, the physics of bunch compression becomes very challenging if collective effects like space charge forces and wake-fields are taken into account[7-9]. Especially emittance conservation is then a critical issue.

Bunch compression requires perfect control of the longitudinal energy distribution inside each bunch. For very short bunch lengths, this energy distribution is distorted or even dominated by longitudinal wakefields. As mentioned before, these wakefields are by far

smallest at TESLA[10], which seems to be an argument in favor of TESLA. Experiments and theoretical work are under progress in this field.

Even if the bunch compression has been perfectly managed, there is still another aspect of wakefields: for ultra-short bunches they determine the longitudinal energy distribution in the bunch[11]. The relative energy spread in the electron beam is very critical for the FEL process. For XFELs, it must not exceed a few 10^{-4} in order not to destroy the resonance condition. Fortunately, this condition must only be fulfilled within a longitudinal scale of the bunch called the cooperation length, which is, for XFELs, much shorter than the bunch length. However, even if a correlated energy distribution over the bunch length due to wakefields does not destroy the FEL operation, it nevertheless spoils the linewidth of the X-ray beam because the electron beam chirp is transferred into a photon beam chirp. One can also think of making use of this chirp for a further photon beam compression.

It is noted that generation and diagnostics of beam qualities close to the mentioned ones is an objective of several single pass FELs either proposed or under construction to study lasing at shorter and shorter wavelengths. Table 1 gives an overview[12-18].

5. UNDULATORS

There is a tendency that the undulator length l_u required to reach the FEL saturation power increases with decreasing photon wavelength. Most XFEL parameter sets call for l_u of at least 50 m. Also, considerable field quality (or corresponding correction elements) is required to guarantee, for instance, that the electron beam centroid does not depart from a straight line by more than 10 μm within some 10 meters of undulator length. Finally, a periodic quadrupole focusing lattice has to be superimposed to achieve the small beam diameter requested. Such an undulator has not yet been built, and it is believed that one should proceed step by step towards the challenging goal [19]. As milestones one may consider the 10 m long NISUS undulator now being installed into an FEL installation at BNL[14], and the 30 m long undulator being under construction at DESY for the TTF FEL project[20].

A very attractive alternative to these planar undulators are helical undulators. They radiate circularly polarized photons, which is of interest for some users, and, as a rule of thumb, they need to beonly half as long as planar devices. Finally it is noted that there is again a common interest with Linear Collider R&D. A 35 m long wiggler and a 150 m long helical undulator are of interest for a high brilliance positron source[21].

6. PHOTON BEAM PROPERTIES

The prediction of photon beam parameters of XFELs is based on both an elaborate theory, see e.g. [22-25] and various computer codes [26]. Figures 5,6 and Table 2 contain characteristic parameters based on electron beam parameters compiled in Table 2. The values quoted on the FEL performance should be used as a guideline only, since there is no experimental experience yet in this wavelength regime. As mentioned before, the average brilliance generated by each undulator is accordingly smaller than the number quoted if the electron beam is distributed to many undulators.

There is a radiation property that is not mentioned in Table 2 called superradiant spiking [10]. Due to the statistical character of the start-up from noise, the XFEL radiation intensity is not homogeneously distributed along the pulse length but concentrated within ultrashort pulses as long as the cooperation length l_c. This length is typically about 1000 times the photon wavelength, i.e. much shorter than the bunch length. The intensity of these spikes is randomly distributed between zero and twice the average intensity[27]. There is no phase correlation between these spikes, so the spike length reflects the longitudinal coherence of the radiation. A fully 3D computer simulation[28] of the start-up process is still missing, and it might be one of the most urgent enterprises to be undertaken to reliably predict the performance of future XFELs.

Brilliance values as a function of photon energy for SBLC and TESLA in Figs. 5,6 all assume the same electron beam quality and 20 GeV beam energy, so the photon energy is adjusted by appropriately choosing the undulator parameters. This results in decreasing brilliance with increasing photon energy. Since at SBLC/TESLA the electron energy is a free parameter, one could think of compensating this tendency by increasing the beam energy for increasing the photon energy. To a certain extent this is indeed possible, but there are two effects that deserve attention:

1. At this energy level there is a large contribution of spontaneous synchrotron radiation, which both detunes the resonance condition and represents a significant source of background to the FEL radiation. For a 20 GeV beam this spontaneous undulator spectrum is included in Figs. 5,6 to illustrate that the peak brilliance even of the spontaneous radiation exceeds that of 3rd generation synchrotron radiation sources by many orders of magnitude.
2. One might think that with increasing electron energy it should be possible to tune the XFEL to shorter and shorter wavelength. There is however a serious limitation due to the quantum fluctuation of spontaneous radiation[24]. For any set of electron beam parameters and tolerable undulator length there is an absolute minimum of photon wavelength which occurs at a finite electron energy. For quite optimistic electron parameters and $l_u = 200$ m this limit is 0.5 Angstrom.

Thus there are two potential ways to make use of the high electron beam energy that is available at a Linear Collider: To increase the XFEL brilliance at a not too small wavelength, or to use the spontaneous undulator spectrum in the hard X-ray regime that can extend up to the multi-MeV range and that provides spectacular brilliance values even without any FEL process.

REFERENCES

[1] R. Brinkmann: Low Frequency Linear Colliders, Proc. EPAC 94, London (1994)
[2] G. Loew (ed.): International Linear Collider Technical Review Committee Report 1995, SLAC-R-95-471 (1995)
[3] N. Holtkamp et al, Proc. 4th ICFA Seminar, Hamburg 1993 and DESY-M-93-05 (1993)
[4] D. A. Edwards (ed.), DESY Print TESLA 95-01 (1995)
[5] R. Brinkmann, DESY Print TESLA 96-01 (1996)
[6] J.E. Clendenin: RF Photoinjectors, to be published in Proc. Linac Conf. Geneva (1996)
[7] Ya.S. Derbenev, et al., DESY Print TESLA-FEL 95-05 (1995)
[8] B.E. Carlsten: Emittance Growth of a Short Electron Bunch in Circular Motion, this conference

[9] M. Dohlus, T. Limberg: Emittance Growth in Bunch Compressors, this conference
[10] A. Mosnier, DESY Print TESLA 93-11 (1993)
[11] A. Mosnier, O. Napoly, DESY Print TESLA 93-07 (1993)
[12] G. Travish, et al., Nucl. Instr. and Meth. in Phys. Res. **A 358** ABS 75 (1995)
[13] R. Sheffield Proc. this conference (1996)
[14] S. Krinsky (ed.),: The BNL DUV FEL Report, BNL Report(Jan. 1994)
[15] A VUV Free Electron Laser at the TESLA Test Facility at DESY, Conceptual Design Report, DESY Print TESLA-FEL 95-03 (1995)
[16] K. Yanagida, et al., this conference
[17] C. Pellegrini et al., Nucl. Instr. and Meth. in Phys. Res. **A 331** 223 (1993)
[18] R. Tatchyn, et al., Nucl. Instr. and Meth. in Phys. Res. **A 375** 274-283 (1996)
[19] R. Tatchyn, et al., Proc. PAC 93, Washington, (1993)
[20] J. Pflüger, et al.: The undulator system for the VUV-FEL at the TTF, this conference
[21] K. Flöttmann (PhD dissertation thesis), DESY 93-161 (1993)
[22] R. Bonifacio, C. Pellegrini, L.M. Narducci, Opt. Commun. **50** 373 (1984)
[23] E.L. Saldin, E.A. Schneidmiller, M.V. Yurkov, Phys. Rep. **260**, No. 4&5 (1995)
[24] J. Rossbach, et al., Nucl. Instr. and Meth. in Phys. Res. **A 374** 401-407 (1996)
[25] R. Bonifacio, et al., Phys. Rev Lett. **73** 70 (1994)
[26] see e.g. W. Brefeld, et al., Nucl. Instr. and Meth. in Phys. Res. **A 375** 295-298 (1996)
[27] P. Pierini, W.M. Fawley, Nucl. Instr. and Meth. in Phys. Res. **A 375** 332-335 (1996]
[28] L.R. Elias, et al. , this conference

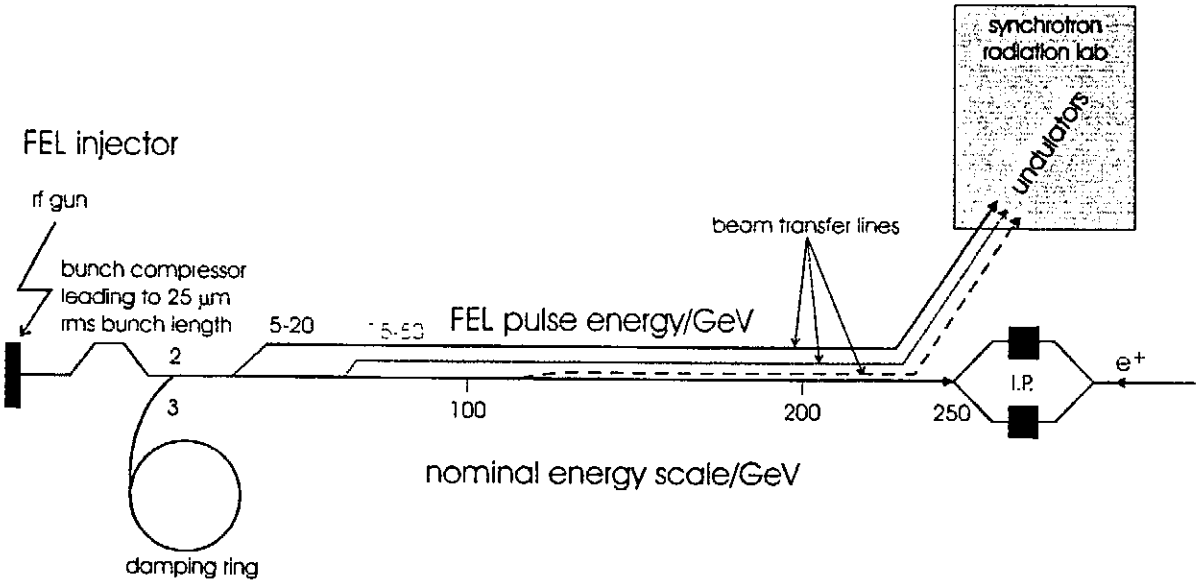

Figure 1: *Sketch of a coherent X-ray source based on a linear collider installation. The beam can be extracted at any energy between 2 and 250 GeV and is transferred inside the linac tunnel to the X-ray lab located close to the interaction points (I.P.). Multiple extraction lines could be utilized in parallel, so that various beam energies are available in the X-ray lab quasi-simultaneously. The XFEL electron beam is provided by an rf gun followed by a sequence of bunch compressors, while the electron (positron) bunch for collider physics is extracted from a damping ring.*

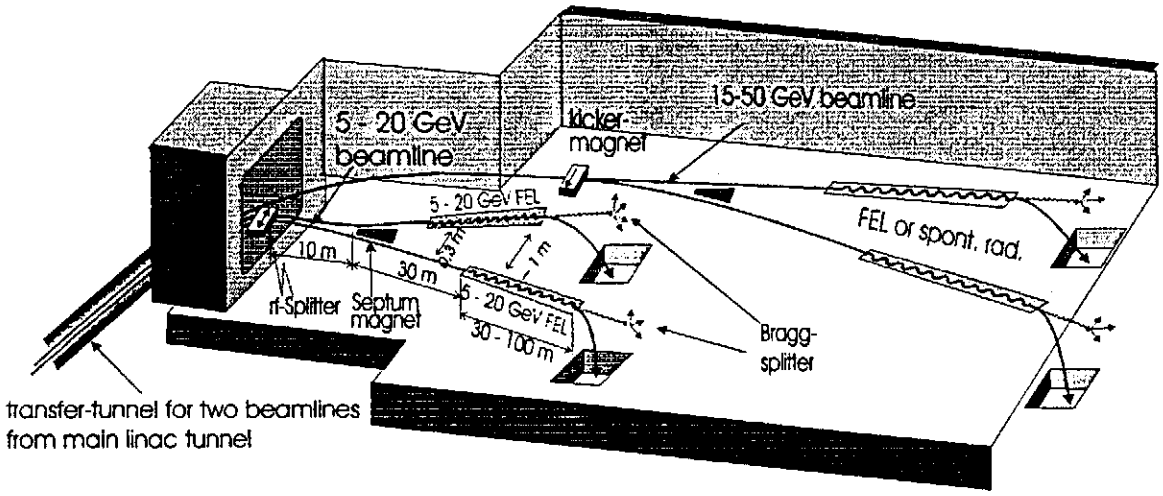

Figure 2: *Beam switchyard distributing two electron beam lines of various energies to different undulators. This distribution can be done within each electron pulse train, so that each undulator still gets a (though 'diluted') pulse train with some 10 Hz train repetition rate. The scheme sketched here can be extended to serve many more undulators.*

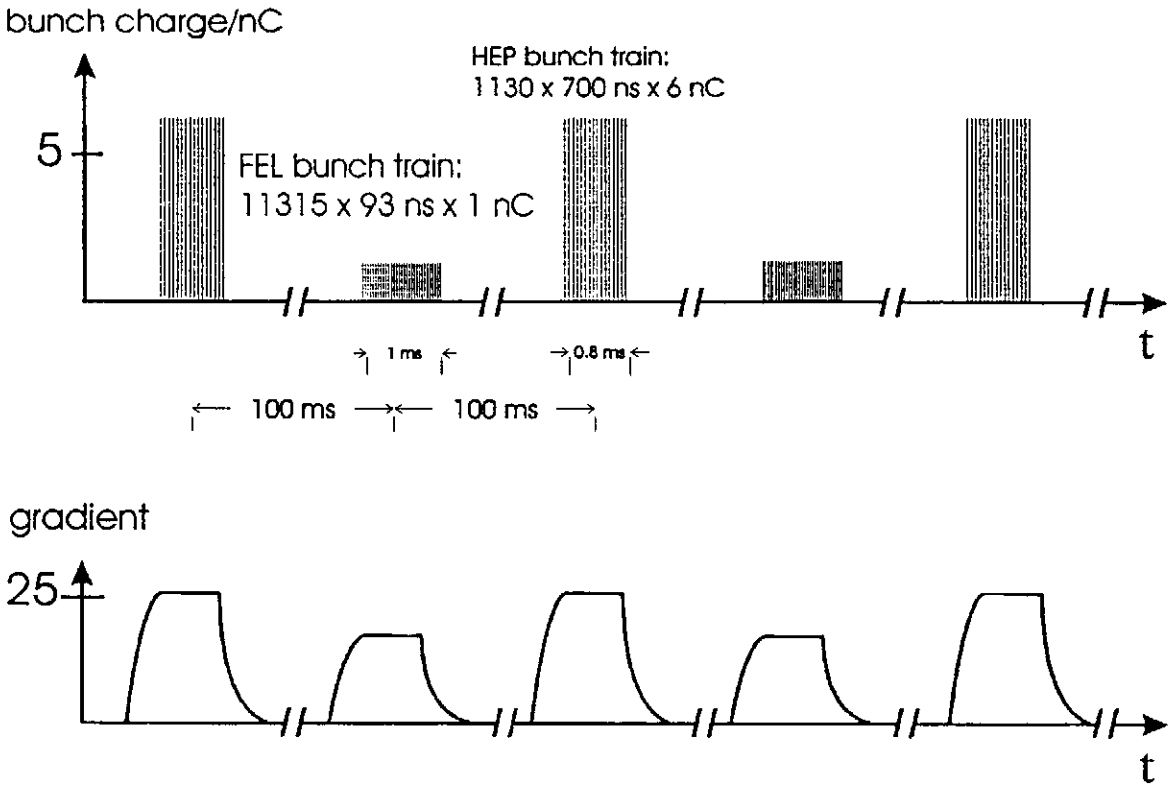

Figure 3: *TESLA pulse structure for high energy physics and X-ray operation.*

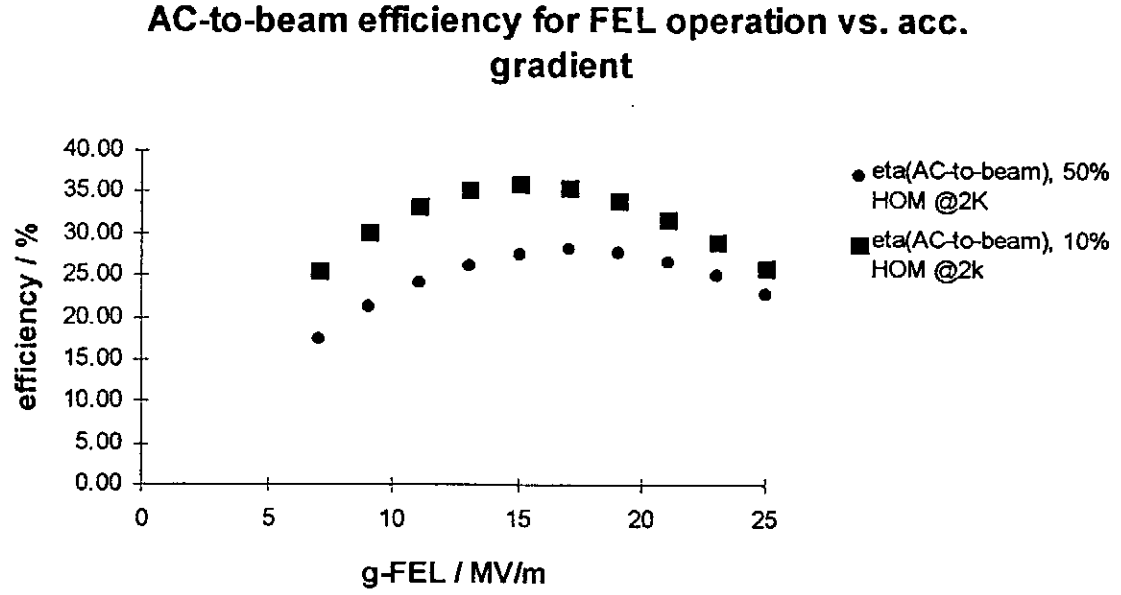

Figure 4: Overall efficiency $\eta_{AC\text{-}to\text{-}beam}$ for the FEL operation mode for the two cases of either 10% (squares) or 50 % (dots) higher order mode (HOM) losses at 2K [5].

When	Where	Wavelength	Objectives
1996	UCLA	10 -20 μm	start-up, growth rate [12]
1996	Los Alamos Ntl. Lab.	16 μm	start-up, growth rate [13]
1997	BNL	≥ 0.9 μm	start-up, growth, saturation, tapering, short bunch, superradiance, harm. generation [14]
1998	DESY TTF FEL Phase 1	50 - 100 nm	start-up, gain length, saturation [15]
1999	Spring-8 (if funded)	20 nm	start-up, gain length, saturation? [16]
2000	DESY TTF FEL Phase 2	6 nm	start-up, gain length, satur., superradiance, harmonics....*USERS* [15]
2000	SLAC LCLS (if funded)	0.1 - 5 nm	dto., *USERS* [17,18]
>2000	Linear Colliders (if funded)	0.1 - 6 nm	dto., *USERS*

Table 1: *Overview of linac based FEL projects relevant to pave the way towards short wavelength lasers.*

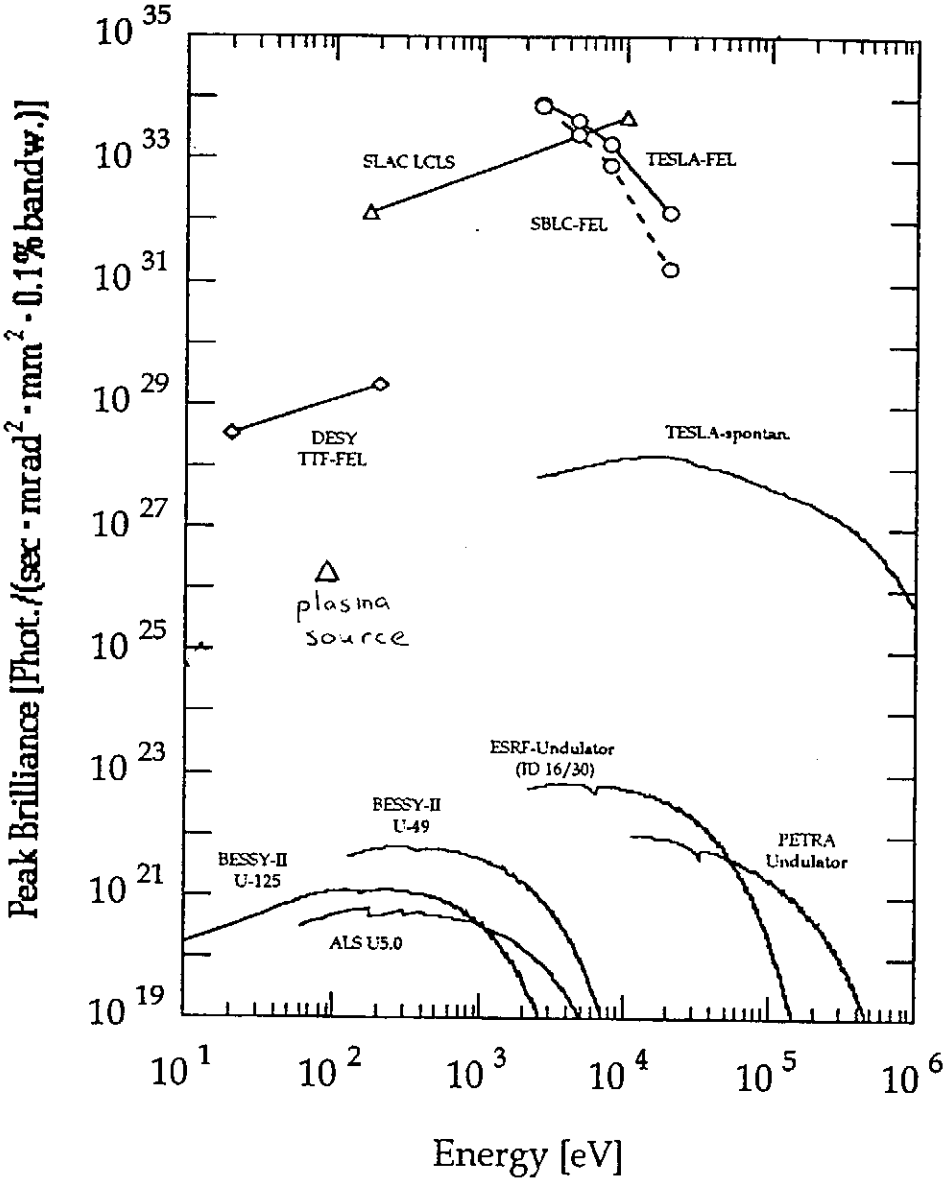

Figure 5: Spectral peak brilliance of XFELs based on SBLC and TESLA linear colliders together with that of third generation synchrotron radiation sources and the LCLS Free Electron Laser project discussed at SLAC, Stanford, USA. For comparison, also the spontaneous spectrum of an XFEL undulator at 20 GeV is shown. The peak brilliance of state-of the-art plasma lasers is also noted.

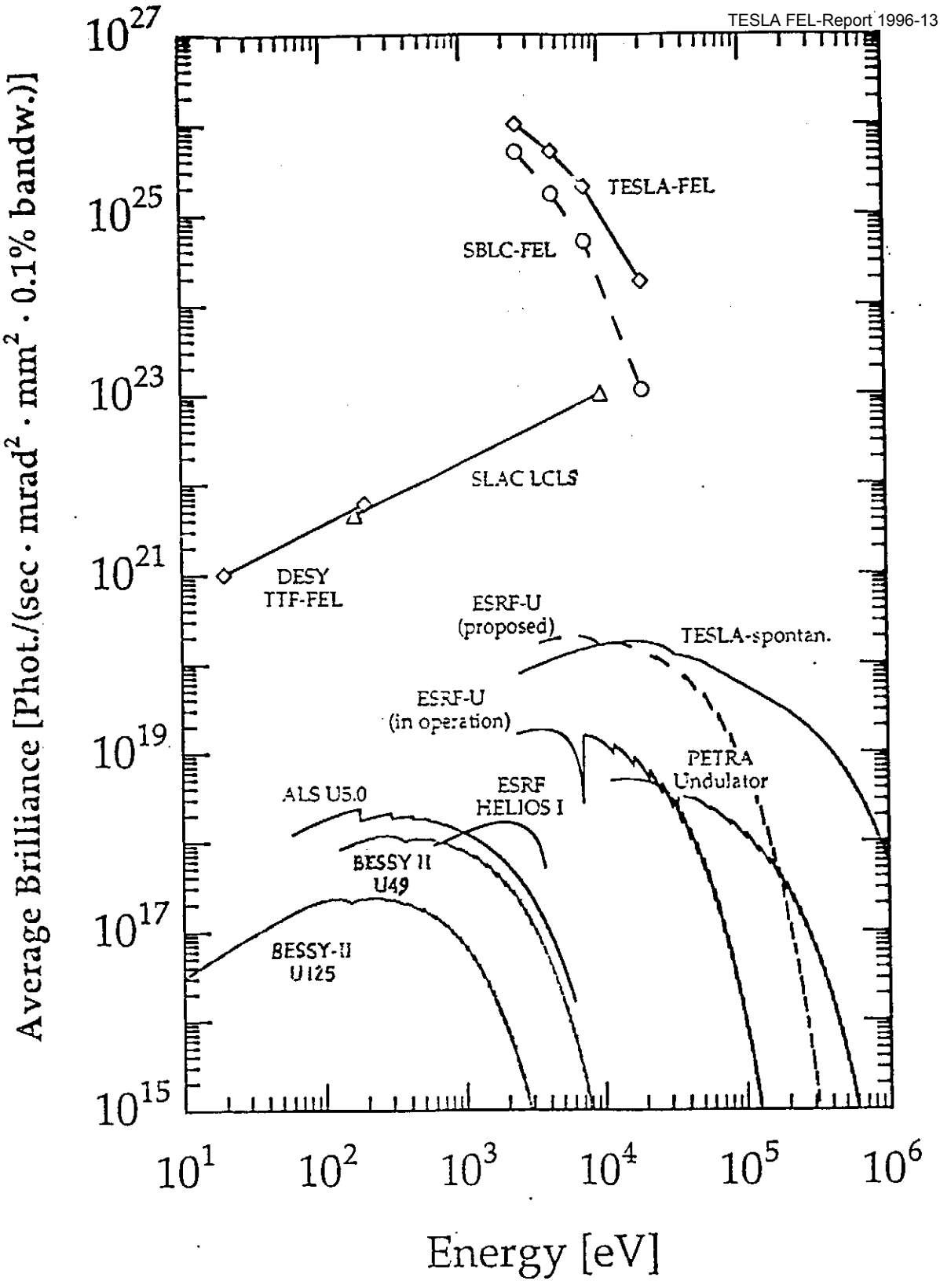

Figure 6: Spectral average brilliance of XFELs based on SBLC and TESLA linear colliders together with that of third generation synchrotron radiation sources and the LCLS Free Electron Laser project discussed at SLAC, Stanford, USA. For comparison, also the spontaneous spectrum of an XFEL undulator at 20 GeV is shown.

Variable	Unit	SBLC	TESLA
rf frequency	GHz	3	1.3
optimized acc. gradient for X-ray operation	MV/m	17	17
linac repetition rate f_{rep} for X-rays	Hz	50	5
bunch length (rms)	fs	80	80
bunch spacing	ns	3.33	93
number of bunches per train		600	11315
bunch train length	μs	2	1050
bunch charge	nC	1	1
normalized emittance	π mrad mm	1	1
electron beam size at 20 GeV (rms)	μm	23	23
pulse beam current	mA	300	11.9
average beam current	mA	0.03	0.059
duty cycle	%	0.01	0.5
average electron beam power at 20 GeV	MW	0.6	1.18
over-all power efficiency AC to beam	%	8.9	28
typical saturation length (planar undulator assumed)	m	50-100	50-100
photon energy range	keV	1 - ~20	1 - ~15
P_{sat} (saturated power)	GW	10 - 100	10 - 100
photons per bunch	E+12	0.5 - 50	0.2 - 50
peak flux [photons/s/0.1%BW]	E+24	2 - 270	1 - 270
average flux [photons/s/0.1%BW]	E+16	2 - 300	0.2 - 150
peak brilliance [photons/s/mm^2/mr/0.1%]	E+32	1 - 100	1 - 100
average brilliance [photons/s/mm^2/mr/0.1%]	E+24	1 - 100	0.1 - 50
typical opening angle (rms)	μrad	1	1
typical source diameter (rms)	μm	20	20

Table 2: *Parameters for coherent X-ray operation with SBLC and TESLA.*

TESLA FEL photo-injector simulations giving high quality beams

J. L. Coacolo, C. Pagani, L. Serafini
INFN - Milano, Lab. LASA. Via F. Cervi 201
20090, Segrate (Milano) Italy.

Abstract

To obtain a high brightness beam for the TESLA FEL project, operating in the VUV region, a photo-injector providing a high quality beam is needed, i.e, the rms radial and longitudinal emittances must be respectively of the order of 1 mm.mrad and 20 mm.KeV [1]. With these drastic conditions we can't use an analytical model with some approximations or scale laws, a refined study of the beam dynamics with a numerical code is necessary. The quality optimization is all the more difficult since many parameters play a role in the beam dynamics. The beam dynamics is simulated by the numerical code ATRAP (Acceleration and TRAnsport of Particles) [2]-[5], using the Liénard-Wiechert's equations to describe the self electromagnetic field. To reduce the total time of this optimization we have chosen the rf peak field on the cathode, between 40 and 60 MV/m, high enough to decrease the space charge effect and not to high, to avoid the defocusing effect of the rf field. In this paper we show the influence of the different parameters on the beam quality.

1 Introduction

To minimize the multipole components of the electromagnetic field in the 1.3 GHz RF cavity, a design with a coaxial input coupler, figure 1, has been proposed [6]. The optimization of the beam quality is not easy, since many parameters play a role in the beam dynamics. For a photo-injector with a solenoid, there are 6 main parameters [7], three of them characterize the space charge field (Q, σ_r, σ_t) the others deal with the accelerating and focusing fields (E_0, ν_{rf}, B_0). With regard to the beam parameters, a part is fixed by the project. The beam charge is 1 nC, the micro pulse rise time of the laser Nd:YLF is 5 ps then the pulse length $\sigma_t = 3$ ps. The beam length at the wiggler entrance must be 50 μm.

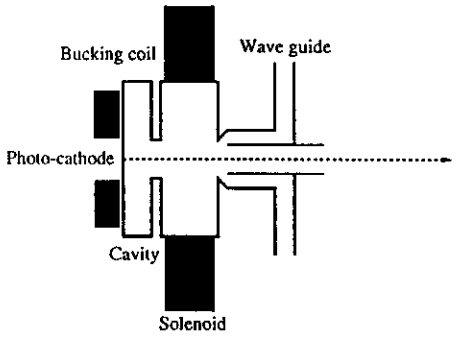

Figure 1: General scheme of the TESLA FEL gun.

To optimize the transverse emittance, the uniform longitudinal distribution is better than a gaussian distribution, because the radial component of the space charge force in the beam, is less dependent from the longitudinal position. Unfortunately the laser beam distribution is close to a gaussian. If we take a longitudinal superposition of pulses, we have a near flat top distribution, a compromise between the uniform and the gaussian distribution. We have chosen a superposition of 3 pulses, because it is the minimum number given a respectable flat top distribution, and a reasonable number, to obtain a beam length of 50 μm, at the wiggler entrance, after three magnetic compressions. In Ref. [8], we have changed the free parameter, which is the gap between two gaussian center, showing that a 7 ps gap (figure 2), with a $\pm$ 5% fluctuation on the flat top, is better than 5.5 ps (the minimun gap to have a respectable flat top) for the radial emittance. This result is due, in great part, to the fact that the ratio between the rise time and the total duration is smaller in the case "7 ps", and the negative tail effects on the transverse emittance are reduced. Afterwards, we consider only the case "7 ps". As the profile is a gaussian sum, and we can't consider all the particles , we need to cut the dis-

tribution tails. In our calculations we use a charge distribution ranging from $\pm 3\sigma_t$ before the first and the last gaussian maximum, to avoid unphysical effects induced by charge discontinuity. Therefore the temporal length [8, 9] is $2(\Delta\text{peak}+3\sigma_t)$, Δpeak being the gap between two gaussian maxima.

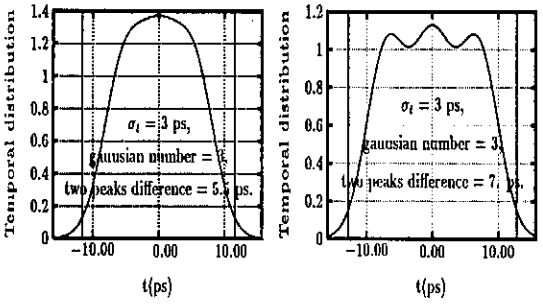

Figure 2: Beam temporal distribution, cases "5.5 ps", "7 ps".

The radial profile is taken as uniform, because this is achievable with a truncated gaussian distribution. The different parameters are summarized in the table 1.

Table 1: The ATRAP simulation parameters.

Charge	1 nC
E_0	50 MV/m
Thermal emittance	0. mm.mrad
Radial profile	uniform
Temporal profile	gaussian superposition
number	3
σ_t	3 ps
Δpeak(1)	7 ps
Launch phase(2)	-34^0

(1) Δpeak is the gap between two gaussian centers.
(2) Launch phase is the phase gap between the beam center exit and the maximum peak field on the cathode.

2 Transverse rms emittance

Since the current in the beam tails is small, we expect that it contributes weakly to the FEL interaction. For this, the transverse emittance is calculated over $2(\Delta\text{peak}+2\sigma_t)$, as shown in the figure 2 (the two vertical lines). The corresponding charge is 0.98 nC.
The definition of the transverse rms emittance is :

$$\varepsilon_r = \frac{1}{2mc}\sqrt{< r^2 >< p_r^2 > - < rp_r >^2}, \quad (1)$$

with $p_r = \gamma m dr/dt$. In figure 3, the minimum value of ε_r in the drift space after the gun exit, is plotted for different beam radii in function of the solenoid peak field. The minimum is between 1. and 1.2 mm.mrad, for a radius smaller than 2.5 mm, what is very close to our objective. In Ref. [8],[9] we have shown that the transverse emittance taking into account the total charge, is between 1.6 and 2. mm.mrad for the same sets of parameters that previously. This result shows that the 2% of the charge at the limits of the initial distribution, if taken into account, increases the transverse emittance value by more than 40%.

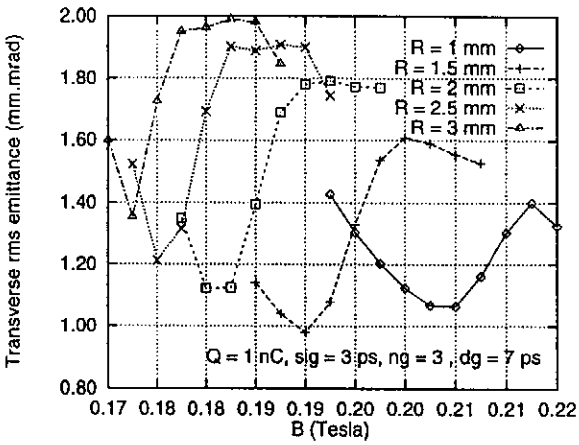

Figure 3: Minimum Transverse rms emittance for 98% of the charge, versus the magnetic peak field.

3 Longitudinal rms emittance

For the definition of the longitudinal rms emittance we have taken :

$$\varepsilon_z = c\sqrt{< \Delta z^2 >< \Delta {p_z}^2 > - < \Delta z \Delta p_z >^2}, \quad (2)$$

with $\Delta p_z = p_z - \overline{p_z}$, $\Delta z = z - \overline{z}$, and $p_z = m\beta\gamma c$. Figures 4 shows the longitudinal rms emittance, ε_z, for 98% of the charge, when the radial emittance is minimum, as a function of the magnetic peak

field. These different curves have large fluctuations, because :

- all these points are not at the same position, ϵ_r minimum moves with the magnetic field,
- the longitudinal emittance is greatly dependent on the rms radius evolution.

We see that we can obtain $\epsilon_z < 20$ mm.KeV for $R <$ 3 mm. Therefore, with the two previous curves, the simulation shows that our objective is reached for a radius less than 2.5 mm.

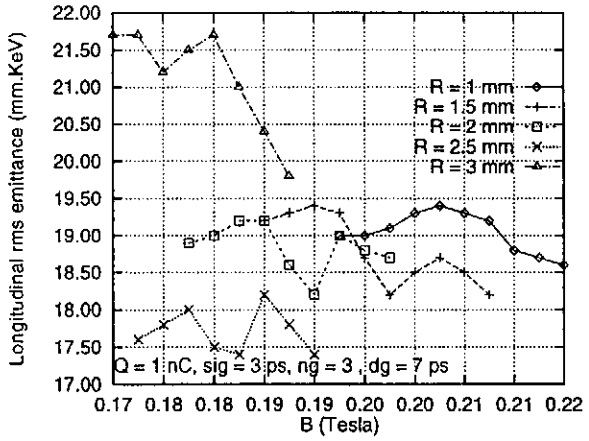

Figure 4: ϵ_z for 98% of the charge, when ϵ_r is minimum, versus the magnetic peak field.

4 On cathode rf field influence

Figure 5 shows the optimized transverse rms emittance versus the magnetic peak field for the case 3 (R = 1.5 mm), and for three different values of the maximum rf electric field E_0 on the cathode. We see that the magnetic field values scales as the rf peak field, because the focusing effect varies like B^2/γ^2 and, to keep the same beam evolution, the magnetic peak field must be a growing function of the energy.

We see that the case $E_0 = 50$ MV is the better case. We can explain this by the fact that increasing the peak field on the cathode the space charge effects decrease, but the rf field effects go up.

Figure 6 shows the longitudinal rms emittance in function of the magnetic peak field at the longitudinal position where the radial emittance is minimum. We see that for a maximum rf field on the

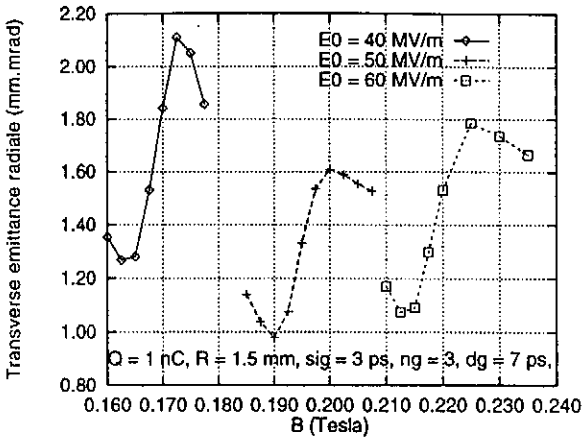

Figure 5: Minimum Transverse rms emittance for 98% of the charge, versus the magnetic peak field.

cathode between 40 and 60 MV, ϵ_z is always less than 20 mm.mrad.

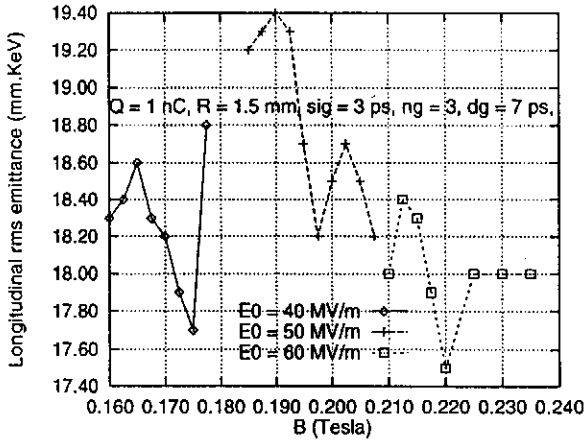

Figure 6: Longitudinal rms emittance for 98% of the charge, when ϵ_z is minimum, in function of the magnetic field.

5 Conclusion

The results exposed in this paper, show that we can have $\epsilon_r \approx 1$ mm.mrad and $\epsilon_z \approx 20$ mm.KeV at the TTF gun exit with a charge of 1 nC. An unconventional temporal distribution like a gaussian superposition with $\sigma_t = 3$ ps, and a flat top fluctuation close to 5% gives 1. mm.mrad for the

transverse rms emittance, if we consider only 98% of the beam charge. We have proved [9] that, using a proper matching of the beam into the first 9 cell SC TESLA cavity after the photo-injector, one can accelerate the beam up to 15 MeV, decreasing even further ϵ_r, at the booster exit. But, with regard to the longitudinal emittance, at the capture linac exit we obtain 40 mm.KeV. In fact the beam is too long and it seems necessary to reduce the rms pulse duration to 2 ps, if we want to operate with this kind of profile.

References

[1] Tesla Test Facility Linac, Design report, Version 1.0, March 1st 1995.

[2] J.M. Dolique and J.L. Coacolo, Proc. 1991 IEEE Particle Accelerator Conf., San Fransisco, 233 (1991).

[3] J.M. Dolique and J.L. Coacolo, Proc. 1992 European Particle Accelerator Conf., 771, Berlin (1992).

[4] J.L. Coacolo, Thesis, Université de Grenoble ,Oct. 13th 1993.

[5] J.L. Coacolo, "ATRAP : a 2D1/2 beam dynamics code using the Liénard-Wiechert's equations", this Conference.

[6] Y. Huang and K. Floettmann, Simulation Study of the RF Gun for the TTF Free Electron Laser, Desy TESLA, 96-01.

[7] L. Serafini and J.B. Rosenzweig, 1996 EPAC 96 European Particle Accelerator Conf., to be published.

[8] J.L. Coacolo, C. Pagani, L. Serafini, 1996 EPAC 96 European Particle Accelerator Conf., to be published.

[9] J.L. Coacolo, C. Pagani, L. Serafini, TTF-FEL Photo-injector Simulation Giving a High Quality Beam, Desy TESLA, 96-04.

A Concept of High-Intensity Polarized Monochromatic Gamma-Source at ESRF

R. Corsini[a], C. Pagani[b], E.L. Saldin[c], E.A. Schneidmiller[c], M.V. Yurkov[d]

[a] *CERN, PS Division, CH-1211 Geneva 23, Switzerland*

[b] *INFN Milano - LASA, Via Cervi, 201, 20090 Segrate (MI), Italy*

[c] *Automatic Systems Corporation, 443050 Samara, Russia*

[d] *Joint Institute for Nuclear Research, Dubna, 141980 Moscow Region, Russia*

Abstract

In this paper we consider a way for constructing a high intensity, monochromatic, polarized gamma-source at ESRF. The principle of operation of the gamma-source is Compton backscattering without knock-out the electrons off the beam. The source of primary photons is high power infrared free electron laser operating in CW mode. The driving beam for the FEL is produced by the accelerator constructed on the base of LEP 2 superconducting cavities. The average flux of the gamma-quanta is about 10^{13} s^{-1}. The gamma-quanta energy is tunable in the range from several MeV up to $\sim$ 60 MeV. The energy resolution of the gamma-source is limited by the finite angle spread in the electron beam and is about 1 %.

Such a gamma-source could form a part of an FEL radiation complex at the ESRF. The heart of this complex is powerful tunable infrared free electron laser. Such a complex may extend significantly the radiation spectrum available at the ESRF for longer wavelengths (down to 100 μm) and for hard γ-rays (up to several tens of MeV). This will allow to extend the scope of experimental researches with the following directions: extension of synchrotron radiation researches with "two colour" experiments for studying chemical reaction dynamics and molecular spectroscopy, researches in nuclear physics (intensive gamma-source) and researches using powerful infrared radiation.

1. Introduction

As a rule, energy acceptance of high energy storage rings is about one percent of the nominal energy. It means, that when the deviation of electron energy lies within the energy acceptance, it does not leave the separatrix and its energy is relaxed to the equilibrium value within the damping time of synchrotron oscillations. Absolute value of the energy acceptance is rather high. For instance, for LEP2 it constitutes the value about 1 GeV. A. Hofmann was the first who noticed that this feature of high energy storage rings could be used for construction of a high intensity gamma-source [1]. The idea was to produce γ-quanta by means of Compton backscattering of laser photons on the electrons. The laser light wavelength is chosen in such a way that after the scattering the electron does not leave the separatrix. Because the probability of the scattering is rather small, energy oscillations are damped prior to the next scattering. The proposed source operates in a "parasitic" mode not interfering with the main mode of the accelerator operation. As a rule, the laser light wavelength should be in infrared wavelength band, which is covered only by free electron lasers [1].

In refs. [2, 3] it was shown that it is technically possible to construct γ-sources at storage rings with an ultimate flux of photons up to 10^{14} γ-quanta/s. The main essence of the idea is to provide precise synchronization of the FEL radiation pulses with the electron bunches rotating in the storage ring. Technical realization of this idea assumes to use superconducting driving accelerator for an FEL oscillator. The frequency of the accelerating RF field should be identical to that used in the RF system of the storage ring. At the present day state-of-art in superconducting accelerator and FEL technology it is possible to construct free electron laser operating in infrared wavelength band with the peak and average radiation power about 10 MW and 1 kW, respectively [4] which reveals the possibility to achieve the above mentioned flux of γ-quanta.

The gamma-source based on Compton backscattering possesses several significant advantages with respect to traditional ones. First, the Compton spectrum has a sharp maximum and the largest fraction of photons is in the high energy region. Second, there is definite energy-angle correlation of scattered photons and the process of Compton scattering is well described by analytical formulae. Third, there is a possibility of steering the polarization of the backscat-

Table 1: Parameters of the ESRF storage ring

Energy	6 GeV
Circumference	844.39 m
Number of bunches[a]	16
Bunch spacing	175.92 ns
Beam current	80 mA
Number of electrons per bunch	8.8×10^{10}
Bunch length	0.6 cm
Horizontal emittance	4×10^{-7} cm rad
Vertical emittance	4×10^{-9} cm rad
Energy acceptance	1 %
RF frequency	352.2 MHz
Synchrotron damping time	3.6 ms
Natural rms energy spread	1.06×10^{-3}
Horisontal $\beta^{(b)}$	26.85 m
Vertical $\beta^{(b)}$	12.85 m

[a] 16-bunch mode of operation
[b] Undulator straight section

terd γ-quanta by the steering the laser beam polarization. Unique features of the γ-source (high intensity, monochromaticity and polarization) together with the latest achievements in the polarized target design will reveal an opportunity to perform a wide range of completely novel experiments in nuclear physics dealing with polarization phenomena.

2. Free electron laser

In this paper we consider possible design of the FEL oscillator synchronized with the time structure of electron bunches in the ESRF operating in 16-bunch mode (see Table 1) [7]. Thus, the repetition rate of the laser pulses should be equal to 5.684 MHz.

Table 2: LEP2 cavity parameters

RF frequency	352.2 MHz
Operating field	6 MV/m
Operating voltage	10.2 MV
Number of cells	4
Effective length (four cells)	1.7 m
Modular length (between cryostat flanges)	2.82 m
R/Q ($R = V^2/2P$)	232 (1/2)
Field flatness tolerance $\delta E/<E>$	± 5 %
Q_0 at operating field (4.5 K)	$> 3.2 \times 10^9$
RF losses at 6 MV/m and 4.5 K	< 70 W
Cryogenic standby losses per complete module	< 90 W
Q_{ext} of RF coupler (nominal)	2×10^6

Table 3: Parameters of free electron laser

Electron beam	
RF frequency	350.2 MHz
Energy, $\mathcal{E}_0$	20 ... 40 MeV
Peak current, I	50 A
Energy spread	150 keV
Normalized emittance, ϵ_n	10 mm-mrad
Micropulse duration	30 ps
Micropulse repetition rate	5.684 MHz
Mode of operation	CW
Average beam current	9 mA
Average beam power	180 .. 360 kW
Undulator	
Undulator period, λ_w	5cm
Undulator field, H_w	1.5 ... 4.5 kGs
Number of undulator periods, N_w	40
Optical resonator	
Radiation wavelength, λ	5 ... 50 μm
Resonator length	26.39 m
Curvature radius of mirrors	13.1 m
Radiation power losses	10 %
Efficiency	0.8 %
Peak radiation power	8 ... 16 MW
Average radiation power	1.4 ... 2.8 kW

2.1. *Accelerator*

The driving accelerator for the FEL is constructed on the base of LEP 2 superconducting cavities (see Table 2) [5]. Four cavities provide energy gain up to 40 MV with the average power in the beam more than 300 kW. RF frequency (352.2 MHz) is identical to that used in the RF system at ESRF, thus synchronization of laser and electron bunches is provided.

The electron bunches (pulse duration 1.5 ns, peak current 1.5 A, average current 9 mA, pulse repetition rate 5.684 MHz) are produced by a gridded electron gun. Then the electron bunches are fed into a subharmonic buncher consisting of two coaxial resonators operating at 6-th and 3-rd subharmonic frequency, respectively. Then the bunches are accelerated up to final energy.

2.2. *Undulator and optical resonator*

General parameters of the FEL oscillator are presented in Table 3. The undulator is a steel-$SmCo_5$ hybrid one with the following parameters: period $\lambda_w = 5$ cm, number of undulator periods $N = 40$. Field amplitude changes in the limits $0.15\ \mathrm{T} < B_w < 0.45\ \mathrm{T}$.

Optical resonator is formed by two spherical copper mirrors (radius of mirror curvature is equal to 13.1 m and aperture - 30 cm). The resonator base is equal to 26.39 m and Rayleigh length is equal to $L_R \simeq 1$ m. One of the mirrors has a hole for radiation

output. Total resonator losses are equal to 10 %. A peculiarity of such a resonator consists in the rather large resonator length which is connected with the low micropulse repetition rate.

At optimal choice of the resonator losses (i.e. at optimal choice of the size of the output hole), the FEL efficiency at saturation is equal to $\eta \simeq 0.3/N \simeq 0.8$ %. Peak and average output radiation power are equal to 8 MW.

A project for an FEL oscillator with parameters close to those required has been developed at LBL [4].

3. Parameters of the γ-quanta source at ESRF

High energy γ-quanta are produced by means of Compton backscattering of the laser photons by the high energy electrons. The energy of the backscattered γ-quanta is considered to be less than the energy acceptance of the storage ring. The frequencies of the incident and scattered photons, ω and ω_γ, are connected by the relation (in the small-angle approximation):

$$\hbar\omega_\gamma = 4\gamma^2\hbar\omega_\gamma/(1+\gamma^2\theta^2), \qquad (1)$$

where θ is the scattering angle, $\gamma = \mathcal{E}/m_e c^2$ is the relativistic factor, m_e and $\mathcal{E}$ are the electron mass and energy, respectively.

The focusing of the laser beam on the electron beam is provided by the mirror installed apart from the electron beam trajectory. Under the conditions of optimal focusing [6] the flux of gamma-quanta is given by expression [2]:

$$\frac{dN_\gamma^{\max}}{dt} = N_e N_b f \frac{2W\sigma_T}{\hbar c^2}\Delta\ , \qquad (2)$$

where N_e and N_b are the number of electrons in the bunch and the number of electron bunches circulating in the storage ring, respectively, W is peak power of the laser radiation, $1/f$, is the revolution time of the electrons in the storage ring, $\sigma_T = 8\pi r_e^2/3$ and $r_e = e^2/m_e c^2$. Factor Δ is equal to unity when the laser beam spot size at the conversion point is much larger than the transverse size of the electron beam. Analysis of the parameters of the existent storage rings shows that in some cases it is difficult to fulfill this condition due to a relatively large value of the horizontal emittance. When the laser beam spot size is larger than the vertical size of the electron beam and smaller than the horizontal one, factor Δ is approximately equal to the ratio of the laser beam spot size to the horizontal size of the electron beam.

Main parameters of the electron storage ring ESRF are presented in Table 1. The energy acceptance of the storage ring is about 1 %, so the maximal energy of γ-quanta is about 60 MeV, and the wavelength of the primary photons should be $\lambda \gtrsim 10$ μm.

Bunch separation in the 16-bunch mode of operation is 175.92 ns. Each time when the electron bunches pass through the focus of the mirror, they scatter the laser photons. In accordance with formulae (2), parameters of the laser radiation and the electron beam parameters at conversion point (see Tables 1 and 3), we obtain the maximal flux of gamma-quanta to be about $dN_\gamma/dt \simeq 3\times 10^{13}$ s^{-1} (see Table 4).

Table 4: Parameters of the gamma-source at ESRF

Maximal energy of γ-quanta	$6-60$ MeV
Average flux of γ-quanta	10^{13} s^{-1}
Angular divergence	85 μrad
Energy resolution	1 %
Polarization	linear / circular
Repetition rate	5.684 MHz
Pulse duration	0.2 ns

Due to the angle-energy correlation of the backscattered γ-quanta (1), the monochromatization of γ-quanta could be provided by angular selection. The angle spread in the electron beam, $(\sigma_\theta)_{x,y} = \sqrt{\epsilon_{x,y}/\beta_{x,y}}$, limits maximal degree of monochromaticity. Vertical emittance of the beam is usually much less than the horizontal one, so maximal degree of monochromaticity is given by:

$$(\Delta\hbar\omega_\gamma)/\hbar\omega_\gamma \simeq (\gamma\sigma_{\theta x})^2/2. \qquad (3)$$

FEL radiation, used as a source of primary photons, is always totally polarized: linearly or circularly for a planar or helical undulator, respectively. In the case of circular polarization of the laser beam, spectral density of backscattered gamma quanta is given with the relation:

$$\frac{dN^+}{d\xi} \propto \xi^2, \qquad \frac{dN^-}{d\xi} \propto (1-\xi)^2, \qquad (4)$$

where $\xi = \hbar\omega_\gamma/(\hbar\omega_\gamma)_{\max}$ and notations N^+ and N^- correspond to the right and left helicity of the γ-quanta. This relation means that there is definite correlation of the energy of the gamma quantum and its polarization. Thus, the angular selection provides not only monochromatization, but determines also the polarization of gamma quanta.

When designing the gamma-source one should take care of an additional energy diffusion in the electron beam arising due to the process of multiple scattering. The coefficient of energy diffusion is given by the formula [2]:

$$< \frac{d(\delta\mathcal{E}/\mathcal{E})^2}{dt} >= \frac{448}{15}\frac{r_e^2\lambda_c\gamma^2\omega^2 W f}{m_e c^5}\Delta\ . \qquad (5)$$

where $\lambda_c = h/mc$.

Let us consider specific example. The laser light wavelength is 23 μm which corresponds to maximal energy of γ-quanta of 30 MeV. Using angular selection, the energy monochromatization about 1 % could be achieved. Within this energy window, in the vicinity of maximal energy, the polarization of γ-quanta is close to 100 %. At average flux of γ-quanta of 10^{13} s^{-1} rms energy spread in the electron beam is 1.2×10^{-3} which is only by 10 % larger than the energy spread in the unperturbed electron beam (see Table 1).

4. A concept of radiation complex at ESRF

The intensive gamma-source described in the previous section could form a part of an FEL radiation complex at the ESRF. The heart of this complex is powerful tunable infrared free electron laser. Such a complex may extend significantly the radiation spectrum available at the ESRF for longer wavelengths (down to 100 μm) and for hard γ-rays (up to several tens of MeV). This will allow to extend the scope of experimental researches with the following directions: extension of synchrotron radiation researches with "two colour" experiments for studying chemical reaction dynamics and molecular spectroscopy, researches in nuclear physics (intensive gamma-source) and researches using powerful infrared radiation.

In our opinion, the ESRF is the most optimal place for constructing such an FEL radiation complex. This is connected with the international status of the Institute, excellent parameters of the storage ring and well developed infrastructure. If such a facility will be constructed, it will be unique one in the world.

The proposed facility will consist of two parts: powerful free electron laser and user facility. As for the free electron laser itself, now there is firm technical base for its construction. The driving accelerator for the FEL could be constructed on the base of LEP 2 superconducting sections [5]. There exist also well developed technical solutions for the injector of the accelerator, undulator and optical resonator design [4]. Another fraction of equipment to be built, is the users equipment. The volume and the cost of the equipment required can be determined only after the step of elaboration of scientific program for this complex.

5. Acknowledgements

We wish to thank A. Hofmann, D. Husmann, G. Materlik, J.R. Schneider, S. Tazzari and A. Wagner for stimulating discussions concerning a possibility of constructing an FEL radiation complex at a high energy storage ring.

6. References

[1] A. Hofmann, Phys. Rep. **64**(1980)253.

[2] E.L. Saldin et al., Nucl. Instrum. and Methods **A362**(1994)574.

[3] E.L. Saldin et al., Nucl. Instrum. and Methods **A375**(1996)606.

[4] K.-J. Kim et al. Nucl. Instrum. and Methods **A341**(1994)280,
LBL preprint Pub-5335(1992)

[5] D. Boussard, "Operetional experience with the LEP 2 SC cavity system", preprint CERN SL-96-016, CERN, 1996.

[6] E.L. Saldin, V.P. Sarantsev, E.A. Schneidmiller and M.V. Yurkov, Nucl. Instrum. and Methods **A339**(1994)583.

[7] European Synchrotron Radiation Facility, Annular Report 1992, ESRF 1992, Grenoble, France. European Synchrotron Radiation Facility, Annular Report 1994/1995, ESRF 1995, Grenoble, France.

Emittance Growth due to Wake Fields on Curved Bunch Trajectories

M.Dohlus, T. Limberg

Deutsches Elektronen Synchrotron Notkestr. 85, 22607 Hamburg, Germany

1 Introduction

A new generation of accelerators, particularly linacs used as FEL drivers or for linear colliders, pushes the single bunch peak current into the kilo-Ampere regime by compressing the bunches longitudinally to 100μm length and below. This compression is done in 'bunch compressors': magnet chicanes or arcs where particles of different energy have different path lengths so that the bunch length can be adjusted by inducing a longitudinal energy gradient. To keep that gradient within reasonable limits, the path length difference per particle energy offset must not be too small, which, given overall length limitations, can necessitate the use of bending magnets with relatively small bending radii (of the order of meters).

If short bunches travel along trajectories with small bending radii a simple geometrical condition permits strong longitudinal and radial wake fields to act on the bunch: electromagnetic fields emitted by a particle can 'overtake' on a shorter straight trajectory and interact with particles which ahead in the bunch. The bunch then starts to radiate coherently. This effect is characterized by the 'overtaking length', the length the bunch needs to travel on its curved trajectory to allow particles to interact via 'overtaking fields' with others one sigma ahead [6]. It is given by pure geometrie; by the difference in length between a circular orbit and its cord:

$$L_o = \left(24\sigma_s R^2\right)^{1/3}$$

with σ_s being the bunch length and R the bending radius. At the storge ring HERA, this length is hundreds of meters and the effect can be neglected. However, in the bunch compression section for the first stage of the SASE-FEL at the TESLA Test Facility [1], a chicane of four dipole magnets with a bending radius of 1.5 meter and a bunch length of $250\mu m$, it is only about a quarter of a meter.

The calculation of the wake fields is described in the next chapter. The calculation of fields, or forces to test particles for a source charge distribution in circalur motion has been done by many autors e.g. transversal effects [2, 7], transversal effects with shielding [3], longitudinal effects [6, 8], longitudinal effects with shielding (infinitely conducting parallel plates) [8], (toroidal chamber) [4, 5]. Our approach is valid for a general path (e.g. straight lines, curved trajectories and the transition from straight to curved or curved to straight pathes).

The source bunch has no transversal dimensions (1D bunch) and does not change its longitudinal profile (rigid bunch). Two- or three-dimensional bunches are composed from one-dimensional line line charges. The simulation of the shielding effects due to infinitely conducting plates in the horizontal plane is taken into account by mirror charges.

Chapter three describes the calculation of emittance increase for the case of a bunch compressor in the TESLA Test Facility FEL. The longitudinal variation of the wake fields cause a correlated bunch deformation in longitudinal-transversal phase space. This can be quantified by a 'centroid-emittance', which interprets the bunch as a sequence of slices and yields the width of the transverse distribution of the slice centroid coordinates. The transverse variation of the wake acts on the bunch like any non-linear field and causes non-correlated emittance growth inside the bunch slices.

2 Calculation of the Lorentz Force

2.1 Approach for 1D Bunches on a General Path

The action of the electromagnetic field caused by a source (index s) to a charged test particle (index t) is described by the *Lorentz force equation*:

$$\frac{1}{q_t}\vec{F}_t = \vec{E}_s + \vec{v}_t \times \vec{B}_s \ . \tag{1}$$

Using the scalar and vector potentials $\vec{E}_s = -\nabla V_s - \dot{\vec{A}}_s$, $\vec{B}_s = \times \vec{A}_s$ this force can be split into two terms:

$$\frac{1}{q_t}\vec{F}_t = \underbrace{\nabla\left(\vec{v}_t \cdot \vec{A}_s - V_s\right)}_{\frac{1}{q_t}\vec{F}_{At}} + \underbrace{\left(-\dot{\vec{A}}_s - \vec{A}_s(\vec{v}_t \cdot \nabla)\right)}_{\frac{1}{q_t}\vec{F}_{Bt}} . \tag{2}$$

As the space charge and current density distributions are determined the scalar and vector potentials can be directly obtained from the *retarded potential equation*. For a one dimensional bunch with the line charge density $\lambda(s,t) = \lambda(s - v_s t)$ which moves with constant velocity v_s along the general path $\vec{r}_s(s)$ the three dimensional vector potential integrations are reduced to line integrals:

$$\frac{1}{q}\vec{F}_{At} = \frac{1}{4\pi\epsilon}\int\left\{\frac{\dot{\lambda}}{cR} + \frac{\lambda}{R^2}\right\}\left(1 - \vec{\beta}_t \cdot \vec{\beta}_s\right)\vec{n}ds' , \tag{3}$$

$$\frac{1}{q}\vec{F}_{Bt} = \frac{1}{4\pi\epsilon}\int\left\{\frac{\left(\vec{n}\cdot\vec{\beta}_t - 1\right)\dot{\lambda}}{cR} + \frac{\vec{n}\cdot\vec{\beta}_t\lambda}{R^2}\right\}\vec{\beta}_s ds' \tag{4}$$

with $\vec{R} = \vec{r}_t - \vec{r}_s(s')$, $\vec{n} = \vec{R}/R$, $\vec{\beta}_s = \vec{v}_s/c_0$, $\vec{\beta}_t = \vec{v}_t/c_0$, and $\lambda = \lambda(s' + \beta_s R - v_s t)$. The integrals are solved numerically. The motion of the test particle (or of an ensemble of particles) can be calculated from the *equation of motion* and it can be verified if the asumed dynamic of the source bunch is consistent. This formulation includes singularities at the location of the line charge:

- transversal force $\propto \lambda/\gamma$
- longitudinal force $\propto \lambda'/\gamma^2$ and
- transversal (radial) force, independent of γ, invers proportional to curvature radius.

The first two contributions are usually called 'space charge forces', the third term has been calculated first by Talman [2] for the case of circular motion. Due to the singularities the 1D bunch model cannot be used as source distribution for the simulation of particle motion. For a realistic simulation at least the horizontal dimensions of the beam have to be taken into account (2D bunch, see section 2.3) or better a fully three dimensional source distribution.

2.2 1D-Examples

In Fig. 1 we have the simple case of a gaussian line charge on a circular path with radius R for two different bunch lengths σ_s. The longitudinal wake function scales as

$$W_\parallel = \frac{q}{\epsilon} \frac{1}{(2\pi)^{3/2} 3^{1/3} \sigma_s^{4/3} R^{2/3}}$$

(at $s = 0$). Fig. 2 shows the transient behavior of the longitudinal wake as the line charge enters a bending magnet. The typical length of the transient zone is of the order of the 'overtaking length'. The radial field, in comparison, has a very short transient region (less than a centimeter).

In Fig. 3 the transient when leaving the bending magnet is shown. Note that the bunch experiences longitudinal wake fields on the straight section following the bending magnet for a distance comparable to the magnet length.

In Fig. 4 we introduce shielding by perfect conducting parallel plates. For this purpose, the fields of a sequence of alternating mirror charges are summed up. The longitudinal wake field is shown for different plate distances or chamber heights (note that the bunch length in this example is 250 μm). The shielding starts to be effective if the 'shielding length'

$$L_s = \frac{\sigma_s^2 + h^2}{2\sigma_s}$$

is of the same order as the 'overtaking length' L_o. L_s is the path length for the electromagnetic field from the emitting particle to the reflecting wall to a particle σ_s behind it. h is the distance between the plates.

2.3 Approximation for 2D Bunches on a Horizontal Path

The exact simulation of two dimensional bunches (in the horizontal plane) is not possible with a rigid horizontal charge distribution. Otherwise particles in circular motion, but with different radial offset would have a different velocit. An approximation of the different motion of transversal slices of a 2D bunch is possible by simulating each slice by an independent 1D bunch. To avoid the singularity at locations without transversal offset to the 1D bunches, a smoothing technique is used, which can be applied if the motion is restricted to the horizontal plane (x,y coordinates). Therefore the field of

a subbunch ν on the path $\vec{r}_\nu$ (with $\vec{r}_\nu \cdot \vec{e}_z = 0$) is replaced by the field of a bunch at $\vec{r}_\nu - \Delta z \vec{e}_z$ for $z > 0$ and by the field of a bunch at $\vec{r}_\nu + \Delta z \vec{e}_z$ for $z < 0$. In this way a two dimensional charge distribution in the plane $z = 0$ is simulated. This corresponds to a horizontal density function

$$g(x) = \frac{1}{\pi} \frac{\Delta z}{x^2 + \Delta z^2} \tag{5}$$

for a bunch in linear motion. The transversal Talman force of a bunch in circular motion has a logarithmic pole with the same spatial dependency as the 'space charge pole' of a linear bunch. Therefore also for the circular motion $g(x)$ describes the horizontal charge density. A rough approximation of a gaussian density with the horizontal width σ_h is obtained for $\Delta z = \sqrt{2/\pi}\sigma_h$. Although the transversal shape of a sub bunch is not quite exact defined and not consistent with the motion, the sumation for the total bunch smears out the errors and converges (with incresing number of slices) to an unique solution (see fig.5).

3 Emittance Growth Calculations

The field calculation for the bunch compressor simulates the bunch as a set of gaussian line charges - each with a different energy, different initial conditiones and an individual path. The rotation and the shortening in the compressor can be exactly modeled. At this stage, the trajectories of these sub-bunches are not effected by the calculated fields.

An independent set of bunch slices, initially lined up, is traced through the compressor and experiences the energy variations due to the longitudinal fields and the transverse kicks due to the transverse fields. Due to the strong longitudinal variation of the fields, the slice centroids follow different paths and a 'centroid emittance' developes.

To evaluate emittance growth at fixed longitudinal positions, the slice in the bunch center is populated with an ensemble of test particles. Here, the fields are evaluated at the transverse offsets of the test particles and applied as energy and angle kicks.

The calculated bunch compressor consists of four half meter long dipole magnets and half meter long drifts (the middle one is actually one meter). The entering beam has a normalized emittance of 1 mmmrad. At a β-function

of 10 m that corresponds to horizontal beam sizes $\sigma_x = 170\mu m$ and $\sigma_{x'} = 17\mu rad$ at the compressor energy of 150 MeV. The bunch enters with a length of about 0.75 mm (one sigma) and an induced energy spread of about 0.3 % and is compressed to 0.25 mm at the compressor end. The maximum dispersion is about 0.3 m and the maximum bunch width about 1 mm (one sigma).

For the tracking, bending magnets and drift spaces (according to chapter 2 drift spaces are active elements!) are cut into slices and the fields are calculated and applied at the end of each slice. Convergence test show that for our case slice thicknesses of about 10 cm are accurate within 10%.

Fig. 6 and 7 show horizontal and longitudinal beam sizes along the bunch compressor. The RMS-values for the spread of the slice centroids are shown, the increase in beam size for the test ensemble in the central slice, the bunch length and the relative energy spread.

First, the results show that our model is applicable: even in the case without shielding the additional energy spread due to wake fields is small compared to the one induced for bunch compression. The generated spread of the slice centroids is for the most part of the compressor small compared to the energy-spread dominated beam size. The increase in beam size of the test ensemble in the central slice is even small compared to the incoming beam size. So for this case it seems justified to perform the field calculation with undisturbed sub-bunches as explained above. For even stronger fields one needs a self-consistent tracking. The implementation into this code presents no principle problem. However, it is questionable whether accelerators which design parameters request such calculations are operable.

Second, it can be seen that in the case without shielding the centroids develope RMS-values which are about equal to the incoming beam in the case of position spread and about five times bigger in the angular spread. The increase in beam size of the test ensemble in the central slice is small compared to the initial beam size. So the slices would lase in the FEL, but would point into different directions. A remedy for this is shown in Fig. 7 where the shielding effect of a 10 mm high vacuum chamber is taken into account. With an adjusted optics, the RMS centroid spreads are smaller than the undisturbed beam size.

4 Summary

We present a complete treatment of the longitudinal and radial electromagnetic forces acting on a bunch travelling on a curved trajectory. Effects like space charge forces, coherent synchrotron radiation etc. are implicitly included. Based on this field calculation a tracking code was developed and results for the bunch compressor at stage I of the TESLA Test Facility SASE-FEL are presented. Emittance growth at fixed longitudinal bunch positions is not a problem, but the bunch is coherently distorted in the horizontal-longitudinal phase space. To reduce this effect to a negligible portion, the vacuum chamber must be less than 10 mm high to provide sufficient shielding.

Formula Symbols

References

[1] A VUV Free Electron Laser at the TESLA Test Facility at DESY. Conceptual Design Report. DESY Print June 1995, TESLA-FEL 95-03

[2] R.Talman: 'Physical Review Letters', Vol. 56, p. 1429, April 86.

[3] A.Piwinsky: 'On the Transverse Forces caused by the curvature', CERN/LEP-TH/85-43, Dec. 1985.

[4] R.Warnock, P.Morton: 'Coherent Synchrotron Radiation in a Toroidal Chamber', SLAC-PUB-456, March 1988.

[5] S.Heifets, A.Michailichenko: 'Ont the Impedance due to Synchrotron Radiation', Proc. 1991, Particle Accelerator Conference, pp. 458-460, 1991.

[6] Y.Derbenev, J.Rossbach, E.Saldin, V.Shiltsev: 'Microbunch Radiative Tail-Head Interaction', TESLA-FEL 95-05, September 95.

[7] Y.Derbenev, V.Shiltsev: 'Transverse Effects of Microbunch Radiative Interaction', Fermilab-TM-1974, May 1996.

[8] J.Murphy,S.Krinsky,R.Gluckstern: 'Longitudinal Wakefield for an Electron Moving on a Circular Orbit', BNL-63090, April 1996.

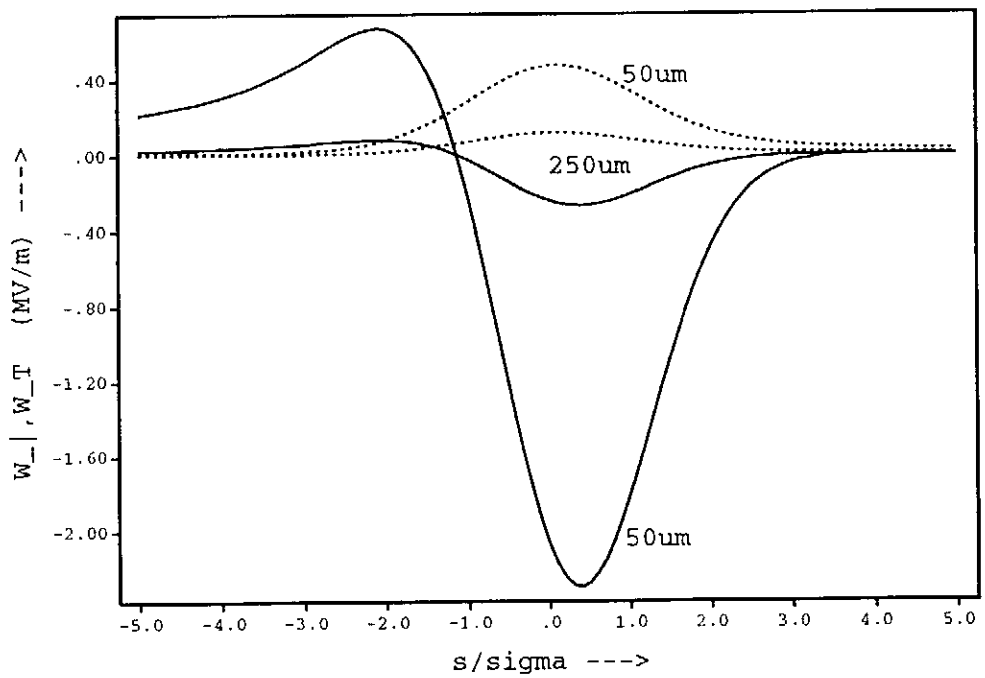

Figure 1: Longitudinal and Transverse Wake
gaussian line bunch, $\sigma = 50\mu$m and $\sigma = 250\mu$m, $q = 1$nC, $R = 1.5$m; observation point: s =ordinate, $\partial r = 0$, $\partial z = 10\mu$m

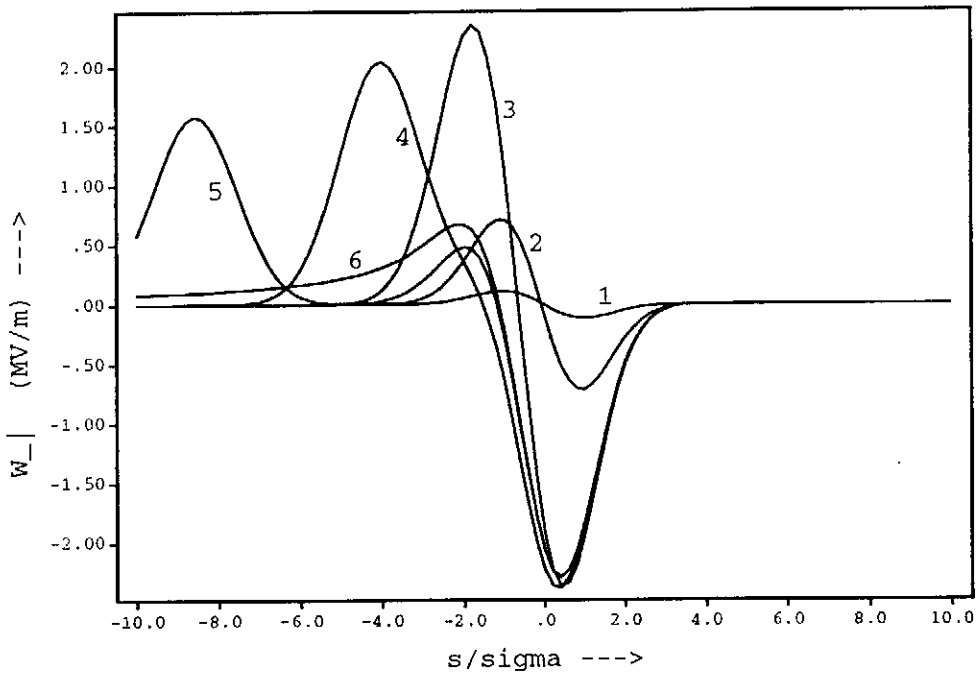

Figure 2: entering the magnet, longitudinal wake
gaussian line bunch, $\sigma = 50\mu$m, $q = 1$nC, $R = 1.5$m; observation point: s =ordinate, $\partial r = 0$, $\partial z = 10\mu$m
curve 1: 2cm after begin of magnet
curve 2: 5cm after begin of magnet
curve 3: 10cm after begin of magnet
curve 4: 14cm (interaction length)
curve 5: 18cm after begin of magnet
curve 6: steady state

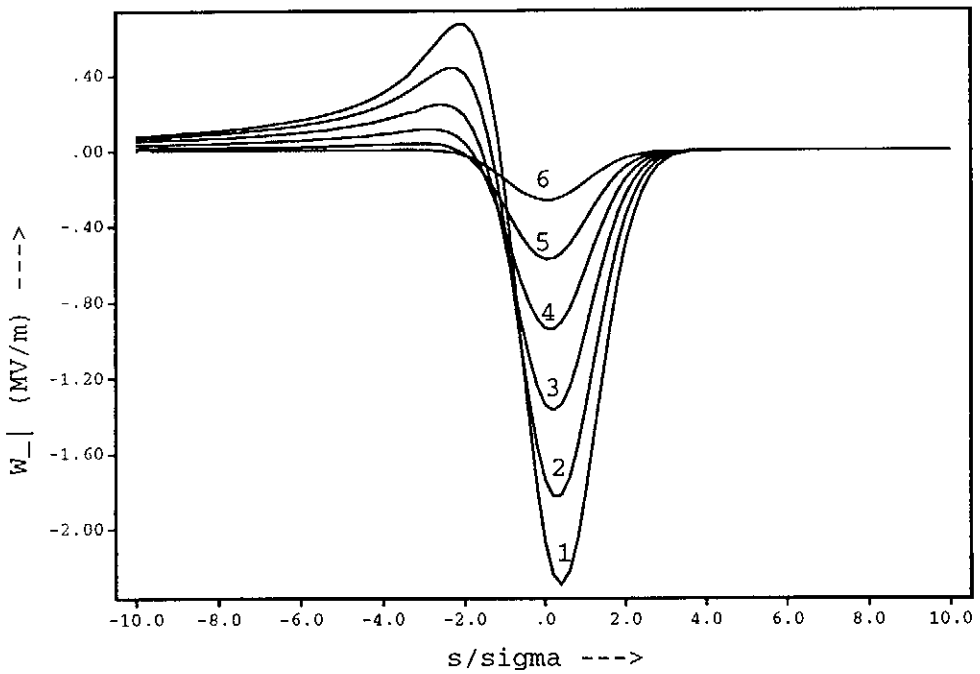

Figure 3: end of magnet, longitudinal wake
gaussian line bunch, $\sigma = 50\mu$m, $q = 1$nC, $R = 1.5$m; observation point: s =ordinate, $\partial r = 0$, $\partial z = 10\mu$m
curve 1: end of magnet
curve 2: 2cm after end of magnet
curve 3: 5cm after end of magnet
curve 4: 10cm after end of magnet
curve 5: 20cm after end of magnet
curve 6: 50cm after end of magnet

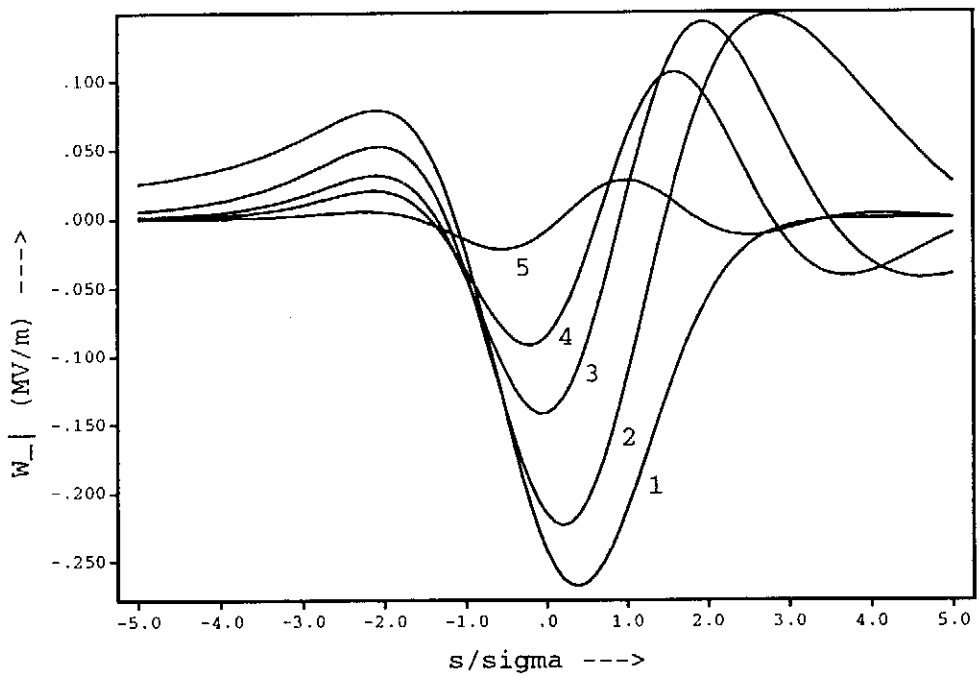

Figure 4: shielding by horizontal plates
gaussian line bunch, $\sigma = 250\mu$m, $q = 1$nC, $R = 1.5$m; observation point: s =ordinate, $\partial r = 0$, $\partial z = 10\mu$m
curve 1: without shielding
curve 2: 15mm distance between plates
curve 3: 10mm distance between plates
curve 4: 8mm distance between plates
curve 5: 5mm distance between plates

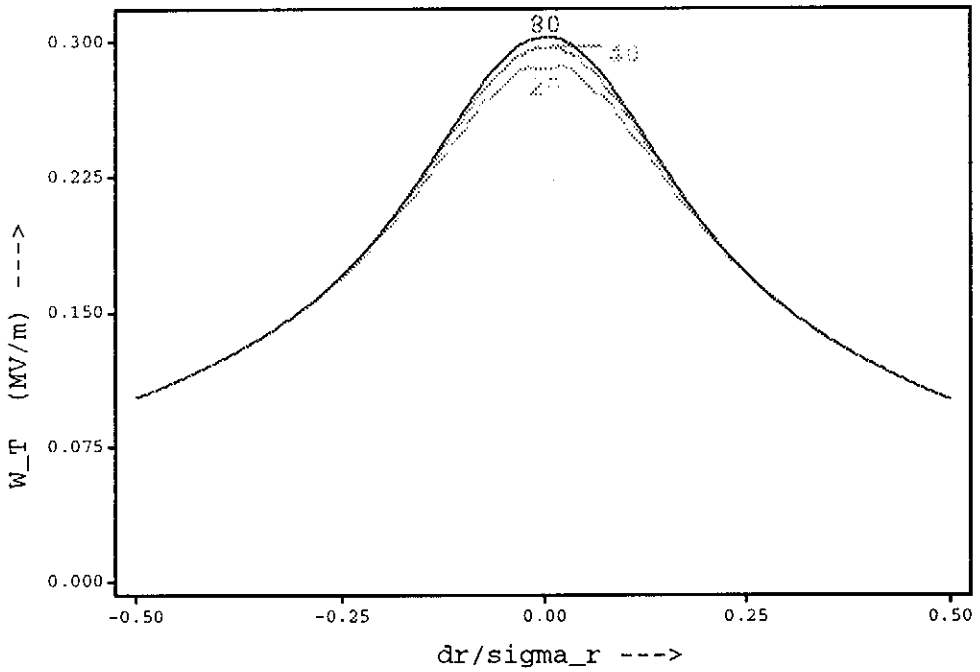

Figure 5: Transversal wake of a two dimensional gaussian bunch: $\sigma_s = 50\mu$m, $\sigma_r = 100\mu$m, $q = 1$nC, no energy spread, $R = 1.5$m; observation point: $s = 0$, ∂r =ordinate, $\partial z = 0\mu$m.
The bunch with the transversal width σ_r is injected to a homogeneous dipole field. After a rotation of $\phi = \pi/2$ the transversal spread is transformed in a pure longitudinal spread. The transversal wakefield is observed after a rotation of $\phi = \pi$ when the bunch has again its initial transversal distribution. The transversal profile is simulated by 20, 40 and 80 subbunches to demonstrate the convergence of the transversal wake.

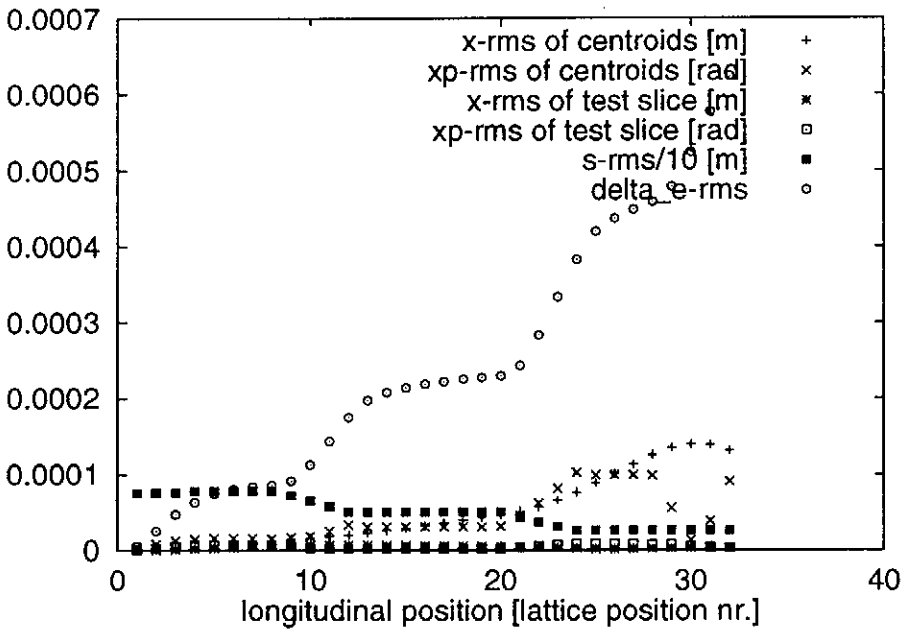

Figure 6: Beam rms-values through the TESLA Test Facility bunch compressor at 150 MeV
$\sigma_s = 750 -> 250\mu$m, $q = 1$nC, $R = 1.5$m;

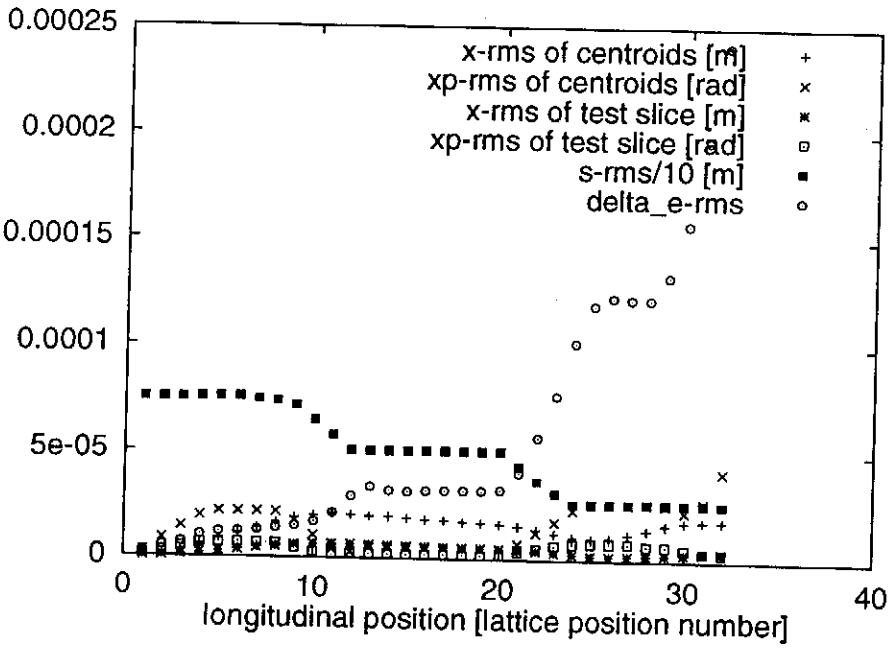

Figure 7: Same as 6, but the wakes are shielded by a 10 mm high vacuum chamber

RF Gun design for the TESLA VUV Free Electron Laser

B. Dwersteg, K. Flöttmann, J. Sekutowicz, Ch. Stolzenburg
DESY, Notkestr. 85, 22603 Hamburg, Germany

Abstract

A high brightness rf gun for the VUV FEL at the TESLA Test Facility is under construction at DESY. Besides challenging beam parameters a high duty cycle of 1% is demanded which requires a powerful cooling system. The rf and the mechanical design of the gun cavity and a new symmetric input coupler are presented. Simulation results and the emittance budget of the gun are discussed.

Introduction

The VUV Free Electron Laser at the TESLA Test Facility at DESY [1] requires an electron beam of 1nC charge per bunch. The transverse and the longitudinal emittance should not exceed 1π mrad mm and 20keV mm, respectively. A high brightness rf gun capable of producing these beam parameters is currently under construction at DESY. Besides the emittance requirements a duty cycle of 1% (1ms rf pulse at 10Hz repetition frequency) is demanded in order to take full advantage of the superconducting linac. The normal conducting rf gun consists of a $1^1/_2$ cell cavity with coaxial input coupler and solenoids for the compensation of space charge induced emittance growth [2] (see Figure 1). The gun will be followed by a 9-cell superconducting booster cavity and a magnetic bunch compressor.

The gun cavity works in a π mode at 1.3GHz as the main linac. It will be powered by a 5MW klystron, which allows to run the cavity up to the required gradient of 50MV/m but leaves only about 500kW for regulation issues and transfer losses. The klystron will later be replaced by a 10MW klystron (under construction) so that the gradient can be increased while a sufficient margin for regulation issues will be kept.

The TESLA linac is designed for the maximum conversion efficiency of wall plug power to beam power. While the TESLA pulse structure foresees 800 bunches of 8nC in one rf pulse of 1ms it would be possible to accelerate up to 8000 bunches of 1nC within one rf pulse for the FEL operation. The operation will start, however, with a maximum bunch number of 800 per pulse.

The Photocathode and the Laser

The electrons will be emitted from a Cs_2Te cathode illuminated by laser light of 263nm. A cathode preparation chamber and a load lock system are under construction at INFN Milan. The laser is designed and build at the Max-Born-Institut Berlin [3]. The decision for both the cathode material and the laser material is governed by the high duty cycle of the linac to be served by the gun. A cathode with high quantum efficiency ($\geq 2\%$) is mandatory in order to keep the average laser power below 2.0W.

The pulse length of 1ms is short compared to the time scale of cooling processes in the gain medium of the laser. The varying temperature distribution in the gain medium may lead to thermal lensing and to an unstable laser operation. Neodymium doped Yttrium-Lithium Fluorid (Nd:YLF) has been chosen as active medium since it combines a small thermal lensing effect with a high induced emission cross section and a relatively

long fluorescence lifetime (480μs). A pulse train with the desired spacing is selected out of the bunches in a pulse train oscillator working at 36MHz by means of pockels cells. The light pulses will be amplified in a linear low gain amplifier chain and then quadrupled in frequency. Relay imaging techniques in combination with spatial filtering will be used to produce a radially uniform intensity profile. The longitudinal beam profile can be adjusted by means of a pulse stretcher based on the method of splitting and overlaying delayed bunches. A minimum (gaussian) pulse length of 5ps FWHM is aimed for. The option of reducing the rise time down to ~2ps by improved mode locking techniques will be studied.

The gun cavity

An elongated half cell is known to improve the transverse emittance of an rf gun. For the present design a half cell length of 0.28λ has been chosen. An even longer cell improves the transverse emittance but on the expense of the longitudinal emittance. The length of the full cell has only a small effect on the emittance thus it has been set to λ/2.
The ratio of the iris radius to the iris thickness is close to 1 which gives a good approximation to the optimized iris geometry found in Ref [4]. Opening the iris while increasing the iris thickness facilitates the construction of cooling channels in the iris, increases the heat conductivity of the iris and increases the cell-to-cell coupling. The rather large value of 0.4% cell-to-cell coupling in the present design results in an improved field stability on the cost of a somewhat reduced shunt impedance. The sensitivity of the field to distortions of the cavity geometry which occur for example due to thermal stress or due to a misplaced cathode plug are rather weak. Therefore it is planned to build the cavity without tuning plungers. The coarse tuning will be made by means of a deformation of the cavity while a fine tuning can be achieved by means of a temperature variation of the gun. Due to the strong coupling a sufficient field stability is expected. In addition beam dynamics simulations have revealed only small emittance distortions over a range of E_1/E_2=0.7-1.5 (E_1=field amplitude in the half cell, E_2=field amplitude in the full cell). Table 1 lists rf parameters of the gun cavity.

input power	4.5MW
resonance frequency	1.3GHz
Q value	21500
max. gradient on the cathode	50MV/m
max. energy gain for a particle starting with β=0 on the cathode	5.6MeV

Table 1 RF parameters of the gun cavity.

Mechanical design and temperature calculations

The average heat load of the cavity amounts to 50kW which has to be removed by the cooling water. The highest power density of 30W/cm^2 occurs at the outer cavity wall, however, the highest temperature occurs at the central iris due to the limited heat conductivity of the copper. A system of cooling channels including also channels inside the iris has been optimized based on numerical simulations of the temperature distribution. The maximum temperature difference has been reduced to 30K. The resulting distortions of the cavity geometry are negligible.

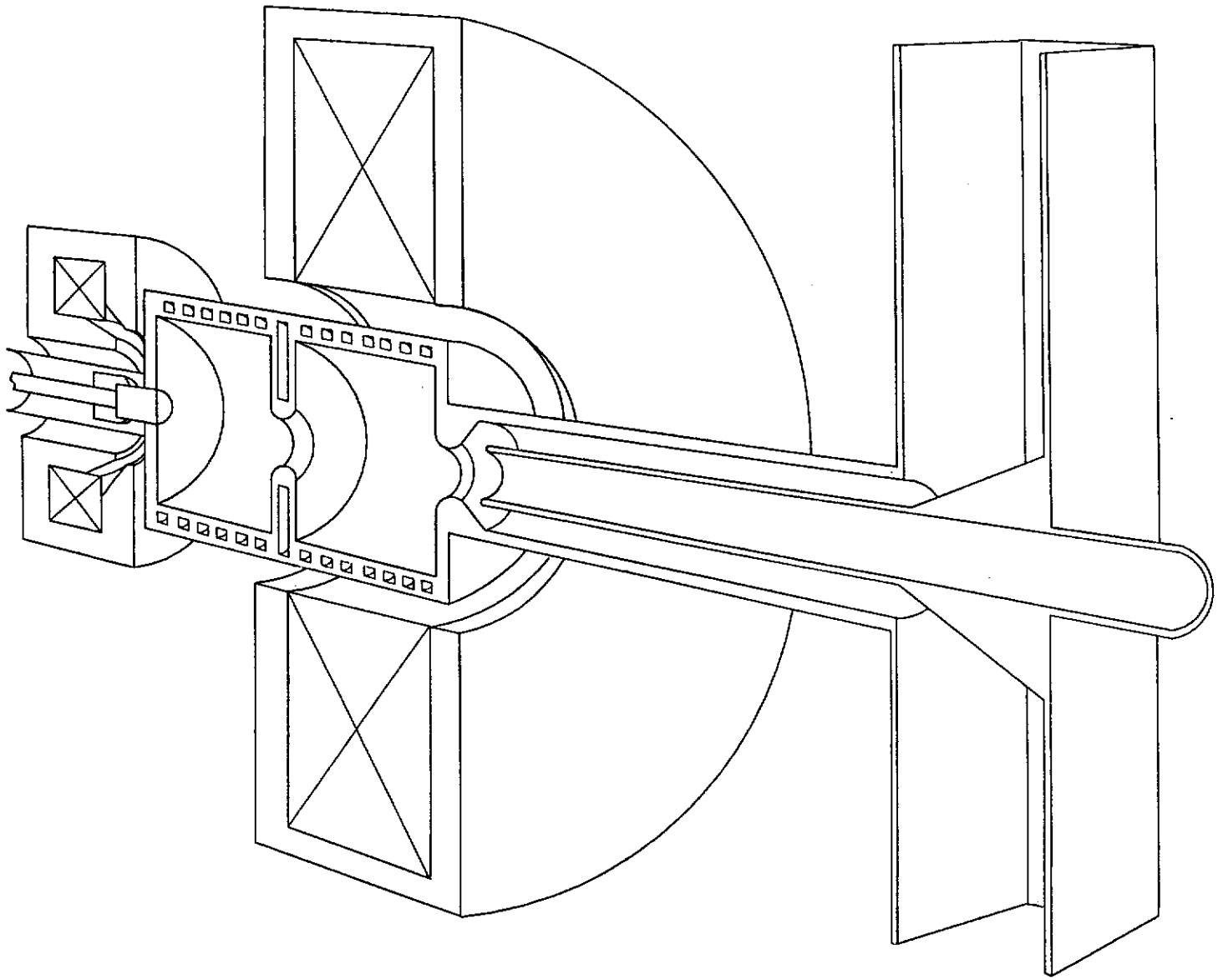

Figure 1 Cross sectional view of the rf gun (schematic) with the gun cavity, the cathode plug, the main solenoid and the bucking coil and the coaxial input coupler. The rf is coupled from the rectangular waveguide via a door knob transition into the coaxial line and the cavity. The electrons leave the gun through the inner conductor.

The mechanical design of the cavity avoids both brazed connections in high field regions and brazed connections between cooling channels and the vacuum system. All cooling channels will be machined from the outside of the cavity, so that a reliable vacuum performance is expected.

The input coupler

In order to avoid emittance growth due to field asymmetries a symmetric input coupler has been developed. Previous calculations have revealed an emittance contribution of more than 1πmrad mm for a conventional asymmetric input coupler. The symmetric coupler is designed as a coaxial input coupler that couples to the cavity on the cavity axis. Figure 1 shows a schematic layout of the gun and the coupler. The electrons leave the cavity through the inner conductor of the coaxial line. Asymmetric mode configurations are strongly suppressed (at least by 1/Q) since the symmetry of the cavity is not disturbed. Dipole modes which can be generated at the door knob transition are in addition damped in the coaxial line. Therefore emittance growth due to field asymmetries is negligible in the present design. A large diameter of the outer conductor has been chosen for the coaxial line to avoid multipacting. A commercial, planar rf window will be used provided that the high power tests which are under preparation are successful. The new coupler design allows to place the focusing solenoid at its optimum position around the full cell of the gun cavity since this area is not occupied by the coupler. In addition the construction of the cooling channels is facilitated since the coupler connects to the gun at an area of low heat deposition.

Cold test measurements

Aluminum models have been build to verify the cavity and the coupler geometry. The inner conductor of the model coupler is adjustable in length so that the coupling could be optimized. A VSWR of 1.15 has been achieved, i.e. only 0.5% of the power is reflected. A 2D finite element code with third order approximation of the field function and curvilinear mesh approximation was used for the design of the cavity [5]. Field profile and frequency measurements revealed a great accuracy of the calculated geometry and the manufacturing of the cavity. Only a small tuning was necessary to obtain a field flatness of $E_1/E_2=1.02$ at resonance frequency.

Magnet design

A conventional solenoid with iron return yoke will generate the required field of 0.22T that is necessary to compensate space charge induced emittance growth. A bucking coil is used to compensate the field on the cathode in order to avoid emittance growth due to the conservation of the canonical momentum. The iron yoke of the bucking coil penetrates into the aperture of the coil thus leaving only a small slot close to the cathode (see Fig. 1). This design -copied from the Los Alamos design[6] - concentrates the field near the cathode and allows to reduce the size of the bucking coil considerably. The main solenoid will be placed on micro movers so that a precise alignment with respect to the cavity axis can be achieved based on beam observations.

Simulation results and emittance budget

In order to optimize the beam parameters and the setting of the focusing solenoid (position and strength) a simulation study has been performed with the PARMELA

code [7] and with the ATRAP code [8]. Both simulations do not include the magnetic bunch compressor behind the booster cavity. (The simulation of the bunch compressor has been started.) Transverse and longitudinal emittances of 1π mrad mm and 20keV mm, respectively, have been achieved at 1nC charge but required an improved rise time of the laser of 2ps. This improvement is in principle possible but requires experimental experience with the laser system under development. With the design parameter of the laser of 5ps rise time transverse and longitudinal emittances of 1.8π mrad mm and 22keV mm, respectively, could be achieved which is sufficient for the Phase I experiments of the TTF FEL.
An emittance budget has been set up in order to include effects which are not taken into account in the simulations. Besides field asymmetries multi bunch effects [9] and field distortions due to the cathode plug have been considered. An investigation of wake fields is on the way. All these effects seem to be negligible in the present design. The thermal emittance of the Cs_2Te cathode has been estimated to be 0.76π mrad mm. A detailed measurement of the thermal emittance is in preparation at INFN Milan.

References

1 'A VUV Free Electron Laser at the TESLA Test Facility, Conceptual Design Report', TESLA-FEL 95-03, DESY, 1995.

2 B. E. Carlsten 'New Photoelectric Injector Design for the Los Alamos XUV FEL Accelerator', NIM A285, 313-319, 1989.

3 I. Will, P. Nickles, W. Sandner, 'A Laser System for the TESLA Photo-Injector' internal design study, Max-Born-Institut, Berlin 1994.

4 K. T. McDonald, 'Design of the Laser-Driven RF Electron Gun for the BNL Accelerator Test Facility', DOE/ER/3072-43, 1984.

5 J. Sekutowicz, '2D FEM Code with Third Order Approximation for RF Cavity Computation', Proc. Conf. Linear Acc., Tsukuba 1994.

6 R. L. Sheffield, 'High Brightness Beams and Applications', Los Alamos Report LA-UR-95-3018, 1995.

7 Y. Huang, K. Flöttmann 'Simulation Study of the RF Gun for the TTF Free Electron Laser' TESLA-FEL 96-01, DESY, 1996.

8 J. L. Coacolo, C. Pagani, L. Serafini 'TTF-FEL Photoinjector Simulation giving a High Quality Beam' TESLA-FEL 96-04, DESY, 1996.

9 K. Flöttmann, Ch. Stolzenburg 'Multi Bunch Effects in a $1^1/_2$ Cell RF Gun' TESLA-FEL 96-08, DESY, 1996.

Geometrical Undulator Tolerances for the VUV-FEL at the TESLA Test Facility

B. Faatz, J. Pflüger and Yu.M. Nikitina

Hamburger Synchrotronstrahlungslabor HASYLAB
at Deutsches Elektronen Synchrotron DESY
Notkestr. 85, 22603 Hamburg, Germany

ABSTRACT

The VUV FEL, which is in its design stage at DESY, is a SASE device driven by a superconducting linac with final energy of 1 GeV. A 30 m long undulator is needed to reach saturation. For practical reasons it is built in sections of about 4.5 m length. In this paper, the specific problems related to this modular setup of the undulator are studied. The main problem turns out to be the alignment of the different modules. Because of the superimposed focusing (FODO) structure which is used in the TTF undulator to keep the electron beam radius small this problem is more severe than in a planar undulator without strong focusing.

1. Introduction

The goal of the TESLA Test Facility (TTF) FEL at DESY is to reach saturation in a single pass through the undulator starting from signal noise [1]. The project is divided in two stages. In phase I, the energy of the electron beam will be 390 MeV, and the minimum achievable radiation wavelength is 44 nm. Compared to phase II, where the electron energy is increased to 1 GeV, radiating at 6 nm, the electron beam parameters can be slightly relaxed, and the length of the undulator can be reduced from 30 m to 15 m. However, for an undulator with this length, there are still severe engineering problems associated with both hardware manufacturing and measurements of the magnetic fields. Therefore, the undulator is subdivided into modules of about 4.5 m length. This makes manufacturing and magnetic field measurements easier, but also imposes tough requirements on the mutual alignment of the individual modules.

Several studies have been performed on the influence of such a modular setup so far [2-4]. For perfectly aligned modules, the gain is changed due to diffraction of the radiation field and due to (de)bunching of the electron beam in the drift sections. For ideal modules, i.e., without magnetic field errors, there can be either transverse or longitudinal misalignment. For a planar undulator without external focusing, this effect on the gain is small. In contrast, with a superimposed FODO-lattice, the overlap between radiation field and electron beam is reduced due to betatron oscillations. The maximum allowable misalignment error in this case is determined by the maximum strength of steering stations and the loss of overlap. Longitudinal misalignment results in a phase mismatch between electron beam and radiation field. All of these effects have to be investigated.

This paper is dedicated to phase I of the TTF-FEL project. Conservatively, the energy used for simulations is taken equal to 300 MeV, resulting in a radiation wavelength of 72 nm. In Sec. 2, results by other authors are summarized and in addition some practical relations are given for steering strength and phase mismatch. In Sec. 3, results of simulations are presented. Finally, results are discussed and conclusions are drawn.

2. Specification of modular undulator geometry

For an ideal undulator, the two important reasons for gain reduction due to intersection gaps are diffraction loss and (de)bunching. Even though the latter can in principle enhance the gain, the effect for a high gain FEL is in most cases only significant close to saturation, in which case the beam debunches due to the large induced energy spread. The situation is different for an optical klystron or for long driftspaces, which are not considered here. In Ref. 2, both effects have been described. For the TTF parameters given in Table 3.1, the loss per intersection due to diffraction is approximately 10% for a Rayleigh length of 0.5 m. The coherence loss is of the order of 20% per intersection. For both effects to be small, the gap length has to be small compared to the Rayleigh length and β-function, respectively. In case of misalignment of different modules in the transverse direction, the influence on the gain depends on whether a FODO-lattice is used or not.

For a planar undulator without strong focusing, a small translation or rotation of a module in an arbitrary direction results only in a minor change of the electron trajectory. The relative change of undulator period seen by the electrons due to a rotation has to be small compared to the Pierce parameter ρ in order not decrease the gain. The situation changes with strong focusing. Because a magnetic axis is now well defined, electrons deviating from this axis will perform a betatron motion. As a result, the overlap with the radiation field reduces and the transverse momentum increases. If corrector stations are available, one can consider redirecting the electron beam along the magnetic axis per module. Thus, only overlap with the radiation field is (partially) lost. The maximum strength per corrector is easy to calculate. If the distance between the last corrector of a module and the first corrector of the next module is L_G, then the transverse displacement, Δx, that can be corrected is given by

$$\gamma \Delta x = \frac{e}{mc} B_s L_s L_G \equiv a_s L_G \,, \qquad (1)$$

with B_s and L_s the strength and length of the corrector (steering) station, and L_G the length of the gap between modules. If the module is only rotated, then the results are the same if the rotation angle is $\Delta x / L_u$, with L_u the length of each module. For a 300 MeV beam, which is studied in this paper, an integrated corrector strength of 0.3 T mm can correct a 100 μm displacement over a drift length of 0.3 m. In addition to the maxium strength and the reduced overlap, the possible large transverse electron beam velocity in the gap introduces an undesired phase shift between electron beam and radiation field. In order for the electron beam to be in phase with the field behind the drift section, one needs

$$L_G \left(1 + a_s^2\right) = n \lambda_u \left(1 + \frac{a_u^2}{2}\right) \left[1 + \left(\frac{\pi \sigma_\gamma}{\gamma}\right)_{\rm eff}\right] \,, \qquad (2)$$

where the effective energy spread is included to take into account the red shift of the wavelength with respect to the resonant wavelength. The factor π may slightly depend on energy, and

$$\left(\frac{\sigma_\gamma}{\gamma}\right)_{\rm eff} = \left[\left(\frac{\sigma_\gamma}{\gamma}\right)^2 + \left(\frac{c \lambda_u}{2 \lambda_s \beta}\right)^2\right]^{1/2} \,,$$

where it has been assumed that $\epsilon_x / \beta_x = \epsilon_y / \beta_y$ [5]. The effective energy spread is usually small, but it is multiplied by an integer n in Eq. (2). If the intersection gap is large, it may play a role. The strength of a corrector station influences the required length of the gap because it shifts the electron beam with respect to the radiation field, which propagates along the z-axis. In order to prevent this shift, a displacement by Δx perpendicular to the magnetic axis should be compensated by a decrease of the intersection gap length by

$$\Delta L_G = -\frac{(\Delta x)^2}{2 n \lambda_s} \,, \qquad (3)$$

where λ_s denotes the radiation wavelength. For the forementioned displacement of 100 μm, the decrease of intersection gap length should be 11.5 mm for the radiation wavelength and intersection gap given in Table 3.1.

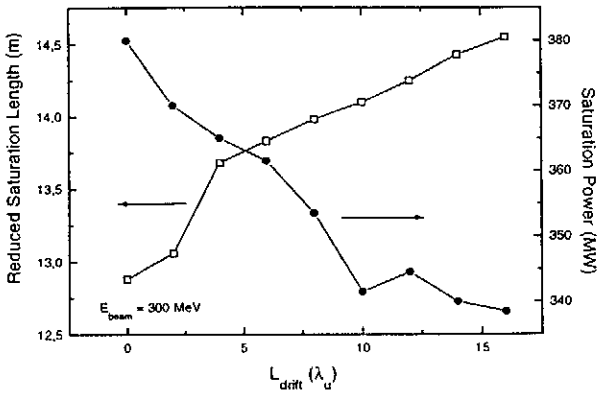

Figure 3.1: *Saturation length and saturation power versus length of the intersection gap.*

3. Results

Before investigating misalignments, first results of an increase of the length of the intersection gaps is shown in Fig. 3.1. The saturation length is given in terms of undulator length minus the total length of the gaps. The length of each undulator module has been kept constant. In order to keep the average β-function constant and smooth over the intersections, the length and strength of the individual quadrupoles, and the FODO-period have been changed for the different calculations. Phase matching of electron beam and radiation field has been guaranteed for all calculations performed. The

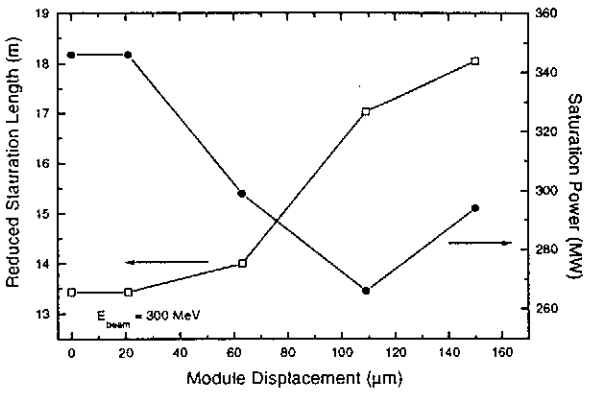

Figure 3.2: *Reduced Saturation length and saturation power versus misalignment of one of the undulator modules. Steering stations have been set to values to prevent betatron oscillations. Increase in length is due to loss of overlap of radiation and electron beam and due to phase mismatch between modules. All remaining parameters are as in Table 3.1.*

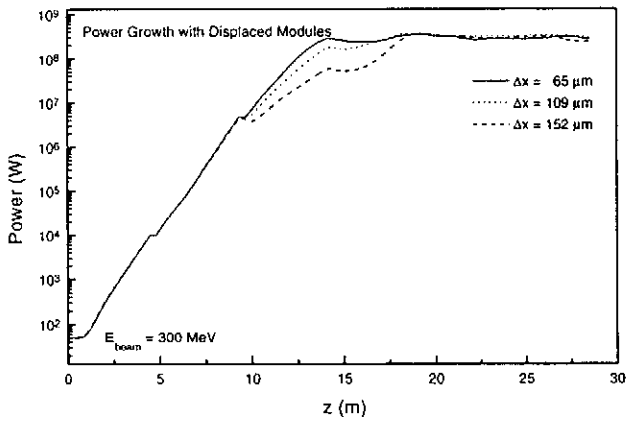

Figure 3.3: *Power growth for three different displacements of the third undulator module. Correctors are used to keep the beam on the magnetic axis at all time. Parameters are given in Table 3.1*

increase in reduced saturation length when one uses a drift space of $16\lambda_u$ is approximately 1.5 m.
As a first possible error, the influence of a variation in average undulator strength a_u has been investigated. Simulations for several values of the Pierce parameter ρ have shown that no change is observed when the change in a_u between two modules is smaller than ρ. As the difference becomes larger, the saturation length increases. Only a change in a_u in the exponential gain regime has been investigated.

Table 3.1: *Parameters used for simulation of the TTF VUV-FEL*

Electron beam	
Energy	300 MeV
Peak current	600 A
Normalized rms emittance	2π mm
rms energy spread	0.17 %
External β-function	1 m
rms beam size in the undulator	57 μm
Undulator	
Type	Planar
Period	27.3 mm
Peak magnetic field	0.497 T
Magnetic gap	12 mm
Undulator section length	4.5 m
Intersection gap	0.30 m
FODO-lattice	
Period	1.2 m
Quadrupole length	0.273 m
Quadrupole strength	9.9 T/m
Radiation	
Wavelength	72 μm

One can easely calculate that for transverse displacement larger than 80 μm, the saturation length increases due to a phase mismatch between the electron beam and radiation field (see Eq.(2) with parameters given in Table 3.1). This is confirmed by the simulation results shown in Fig. 3.2, where the saturation length and saturation power are shown for different values of the transverse displacement of the third module. The results are almost independent of which one of the first three modules is shifted. In all cases, steering stations at entrance and exit of the modules are used to realign the electron beam to the magnetic axis. The length of the intersection gap has not been adjusted to compensate for the phase mismatch. In Fig. 3.3, the power growth along the undulator is shown for different displacement of the third undulator module. A displacement up to 20 μm did not need any correction: it did not reduce the gain. For a displacement of 109 μm, radiation was absorbed due to phase mismatch at the modules' entrance. For 152 μm, the dip in power is even more apparent. In addition, the power growth was slower, probably due to loss of overlap.

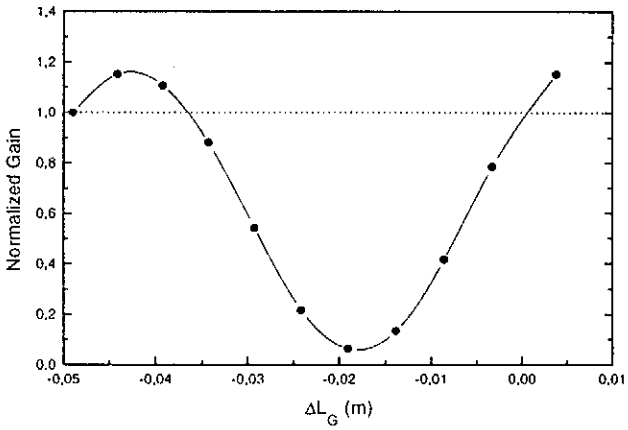

Figure 3.4: *Gain for different values of the change in gap length. $\Delta L_G = 0$ corresponds to $L_G = 0.54$ m, which gives exact phase match without energy spread. All other parameters are given in Table 3.1. The dotted line indicates the reference value for the gain that would be obtained for this length.*

A final point to be addressed is the phase mismatch due to effective energy spread. In order to enhance this effect and to be able to change the intersection gap length by small amounts, the electron phase equation has been changed in the TDA simulations to include a matching field

$$\psi' = k_u - \frac{k_s}{2\gamma^2}\left(1 + \frac{a_D^2}{2} + p_\perp^2\right) .$$

All other electron equations describe a pure drift. The inclusion of a_D gives a possibility to match the phase between electrons and field for any gap length. For $a_D = 0$, the original equations are recovered. For $a_D = a_u$, the phases are always matched according to the first order relation between gap length and phase matching given in Ref. 2 (see also Eq. (2) without effective energy spread and steering strength).
The length of the gap has been made larger than the value given in Table 3.1 in order to enhance the effect of a change in length, which is proportional n in Eq. (2). Results are shown in Fig. 3.4. For the TTF-FEL parameters, the gap length has to be increased by approximately 2 mm, giving a 7% larger gain.

4. Conclusion

In case that the undulator consists of several modules, a number of criteria have to be fullfilled. Between different modules, the average value of a_u should not differ more than by an amount ρ. Larger differences will increase the saturation length. A displacement of undulator modules by less than 20 μm does not influence the FEL proces. The betatron motion is small in this case. For any displacement larger than this, correctors have to be used in order to adjust the electron beam position to the magnetic axis of each individual module. For displacements up to 60 μm, there is no gain reduction after correction of the electron beam. For larger displacements, both a phase mismatch between radiation field and electron beam, and a loss of transverse overlap between the two, give rise to an increase in saturation length (see Eq. (1) and Fig. 3.2). One can compensate for the phase mismatch by readjusting the drift length by an amount that can be calculated with Eq. (3).
The choice of the length of the intersection gap is slightly influenced by the red shift of the radiation wavelength compared to the resonant wavelength, determined by the effective energy spread (Eq. (2)). For the TTF-parameters, this gives a length increase of the gap by 2 mm, corresponding to a phase mismatch of 15^0 between field and electron beam.

References

1. "A VUV Free Electron Laser at the TESLA Test Facility: Conceptual Design Report", DESY Print TESLA-FEL 95-03, Hamburg, DESY, 1995.

2. K.-J. Kim, M. Xie and C. Pellegrini Nucl. Instr. Meth **A375** (1996) 314.

3. N.A. Vinokurov Nucl. Instr. Meth. **A375** (1996) 264.

4. A.A. Varfolomeev and T.V. Yarovoi Nucl. Instr. Meth. **A375** (1996) 352.

5. J. Roßbach, E.L. Saldin, E.A. Schneidmiller and M.V. Yurkov, *Nucl. Instr. Meth.* **A374** (1996) 401; E.L. Saldin, E.A. Schneidmiller and M.V. Yurkov, *Physics Reports* **260** (1995) 187.

Study of the Undulator Specification for the VUV-FEL at the TESLA Test Facility

B. Faatz, J. Pflüger and Y.M. Nikitina

Hamburger Synchrotronstrahlungslabor HASYLAB
at Deutsches Elektronen Synchrotron DESY
Notkestr. 85, 22603 Hamburg, Germany

ABSTRACT

In this paper, the influence of undulator errors, more specific magnetic field errors, on the Free Electron Laser performance is investigated. Both the influence of variation in undulator peak field and of dipole fields resulting from misaligned quadrupoles, is considered. For these quantaties, upper limits are given, and the influence of additional correction stations on the reduction in performance is studied.

1. Introduction

When building a Free Electron Laser (FEL) in the visible and beyond, much effort is spent in getting a small electron beam emittance and energy spread. In VUV and X-ray FELs, where high-reflectivity mirrors are no longer available, saturation of the radiation power has to be reached in a single pass through the undulator. At DESY, the aim is to reach saturation starting from signal noise. For this process of Self Amplified Spontaneous Emission (SASE), an undulator with a length of ten to a hundred meters is required for the power to saturate [1]. For an undulator with this length, undulator errors can start to decrease the gain and thus increase the saturation length. Detailed knowledge of the influence of undulator errors is needed in order to built a device that limits the increase in saturation length without imposing an unrealistically high undulator field quality.

During the past decade, both analytical and numerical studies have shown that the two important parameters that determine the FEL performance are the phase of the electron with respect to the optical field, as well as the beam wander, i.e., the deviation of the electron beam from the optical axis [2-10]. The first quantity determines the energy exchange between electrons and the field, the second determines the transverse overlap between electron beam as a whole and the radiation field. All undulator errors can be expressed in terms of these two physical quantities. Possible gain reduction due to the modular setup of the TTF-undulator is the subject of a separate paper. The aim of this study is to determine the influence of both beam wander and phase shake on the FEL gain as well as establish some general idea how many steering stations are needed per module in order to keep the electron beam within some acceptable distance from the optical axis. For the simulations, the energy of the TTF-FEL of stage 1 is used, but the results are general and can be applied to all TTF energies as well as to other high-gain devices. In section 2, some comments will be made on the possible field errors. In the next section results of simulations for different error distributions are shown. In the last section the results are discussed and tolerances as well as specifications for the undulator are given.

2. Sources of undulator errors

In the undulator for the TTF-FEL, the intrinsic errors are roughly

(1) magnetization direction errors.
(2) undulator period variation.
(3) magnetic peak field errors and quadrupole misalignment.

All of these errors influence the resonance condition (phase shake) and overlap between electron beam and radiation field (beam wander). The variation of resonance condition occurs even when the electron beam remains on the optical axis (non-steering error). The second one is due to a non-zero magnetic field integral (steering error). Even for a very poor undulator quality, steering errors can be corrected. The resonance condition is, however, given with given undulator and determines the quality that is needed for the undulator.

All errors can be described by an effective variation in B_y and a quadrupole displacement. Errors perpendicular to this direction can in first order be described independently. For an electron beam close to the magnetic axis, the beam wander is inversely

Table 3.1: *Parameters used for simulations of the TTF VUV-FEL*

Electron beam	
Energy	300 MeV
Peak current	600 A
Normalized rms emittance	2π mm mrad
rms energy spread	0.17 %
External $\overline{\beta}$-function	1 m
average beam size	57 μm
Undulator	
Type	Planar
Period	27.3 mm
Peak magnetic field	0.497 T
Magnetic gap	12 mm
Undulator module length	4.5 m
FODO-lattice	
Period	1.2 m
Quadrupole length	0.273 m
Quadrupole strength	9.9 T/m
Radiation	
Wavelength	70 nm
Gain for the first module	203

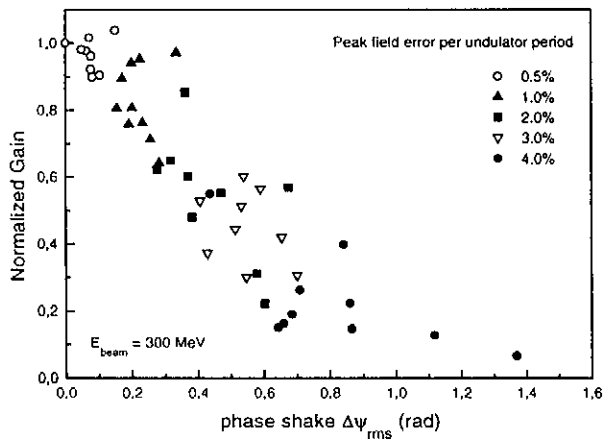

Figure 3.1: *The power gain after the first undulator module as a function of rms phase-shake. The error has been varied between 0.5% and 4%. The gain has been normalized to the gain without field errors. All remaining parameters are as in Table 3.1.*

proportional to energy. The phase shake is independent of energy. It is obtained by subtracting a linear part over one gain length from the phase to minimize the average phase advance. A first indication of the largest rms value of the phase shake that is acceptable, one can compare $\Delta\psi_{\rm rms}$ with the rms-value of the phase due to energy spread over one gain length (for $a_u \approx \sqrt{2}$)

$$\sqrt{3}\rho\Delta\psi_{\rm rms} = \sqrt{\left(\frac{\Delta\lambda_u}{\lambda_u}\right)^2 + \left(\frac{\Delta a_u}{2a_u}\right)^2} < \frac{\sigma_\gamma}{\gamma}, \quad (1)$$

where $\Delta a_u = e\lambda_u \Delta B_0/(2\pi mc)$ only includes peak field errors, and ρ is the well-known Pierce parameter [11]. With $\sigma_\gamma/\gamma < \rho$, we get $\Delta\psi_{\rm rms} < 1/\sqrt{3}$. One can see that Eq. (1) depends on energy indirectly through the gain length $\ell_g = 4\pi\lambda_u/\rho$. For a fixed distance, however, the rms phase shake is independent of energy for an on-axis electron beam. More details on the influence of both phase shake an beam wander on the FEL performance are obtained from simulations of which results are presented in the next section.

3. Results

The simulation presented in this section have been performed for one undulator module, using the TDA code [12]. The TTF-FEL parameters used for these simulations are given in Table 3.1.

The first set of simulations is done for a random undulator peak field error per undulator period. As a consequence, there is no beam wander and gain degradation is only due to phase shake. In Fig. 3.1, the gain, normalized to the gain without undulator field errors, versus rms phase-shake is shown. The undulator errors have been varied from 0.5 % to 4 % in order to see a reduction in gain. The results are very similar to simulations performed by other authors (see for example Ref. 5).

In case of the TTF-FEL, where $\sigma_\gamma/\gamma \approx \rho/2 \approx 2 \cdot 10^{-3}$ for the 0.3 GeV case, the phase-shake due to undulator errors has to be small compared to $17^0 = 0.3$ rad in order not to have any influence (see Eq. (1)), as confirmed by Fig. 3.1. A first estimate on random peak field errors is $\Delta a_u/a_u < 4 \cdot 10^{-3}$. Note that with increasing rms field peak field error, the average gain reduction becomes larger as well as the deviation from this average value (see Ref. 6).

In a more realistic situation, the non-zero first and second magnetic field integrals will result in wander of the electron beam, thus reducing the overlap between amplified wave and electron beam. For

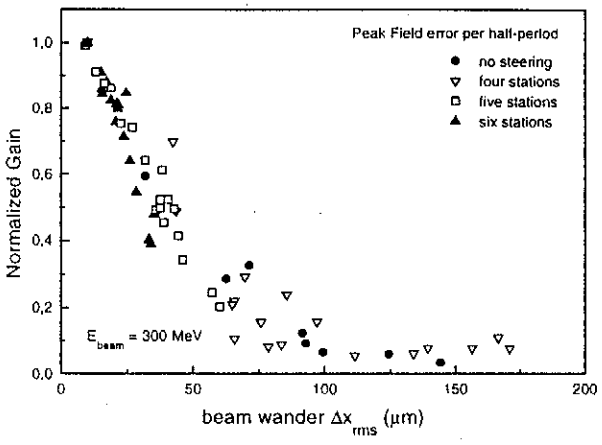

Figure 3.2: *The power gain after the first undulator module as a function of rms electron beam wander without steering stations (solid circles), with four (open triangles), five (open squares) and with six steering stations (solid triangles) within the module. The peak field error is 0.5%. The gain has been normalized to the gain without field errors. All remaining parameters are as in Table 3.1.*

this reason, all remaining simulations have been performed with a magnetic field error per half period. Its rms value has been chosen, based on the requirement deduced from Fig. 3.1, to be equal to 0.5 %. In Fig. 3.2, compared to the previous figure, where the same error of 0.5 % gave a reduction in gain of no more than 10 %, one can see that the influence of the beam wander causes the gain to be reduced to almost zero in some cases if one does not include any steering stations (solid circles). Because the main cause is the beam wander in this case, the gain reduction is given versus this parameter, rather than versus phase shake (see also Ref. [13]).

As can be seen, the simulated results including steering stations follow the same curve as without steering stations. The steering stations have are approximated by δ-functions at equidistant positions with the first one at the entrance of each undulator module and the last one at its exit. It is assumed that detection of the electron beam center is perfect. At each steering station position, there is a beam position monitor (the so-called coincident arrangement, see Ref. 4). At each of these monitors, the electron beam is on axis. Therefore, the field integral from one steering station to the next is equal to zero. Possible misalignment of monitors is not taken into account. In general, the performance increases with number of steering stations. In Fig. 3.2, results are shown for zero (solid circles), four (open triangles), five (open squares) and six steering stations (solid triangles). Without steering stations, the rms beam wander is in most cases larger than the 200 μm shown in this figure, and the gain is correspondingly small. Even with six steering stations the gain can be as small as 40% of the ideal gain. With seven steering stations (not shown in this graph), the gain reduction is no more than 30 %. This in turn means that one steering station per gain length would suffice. Note that the rms beam wander has to be of the order of 10 μm. This value is comparable to the normal oscillation amplitude $x = \lambda_u a_u/(2\pi\gamma)$ for 300 MeV. The rms beam wander can be expressed in terms of the second field integral, which has to be approximately 10 T mm^2. The maximum integrated dipole field of the steering station needed to correct the beam trajectory was $B_s L_s \approx 1$T mm, where B_s is the magnetic strength of the correction station, and L_s is its length. A more typical steering strength was 0.25 T mm. One has to realise that beam wander is calculated from an integral along a particle trajectory, whereas a field integral is performed along a straight line. As a consequence, the correction strength is only proportional to the second field integral between correctors if the quadrupoles do not change the electron trajectory. In all other cases, the strength depends on whether the correction occurs within a defocusing or focusing quadrupole. Simulations with a (random) rms misalignment of the individual quadrupoles in the x-direction within $\pm 50\,\mu$m follow approximately the same curve as Fig. 3.2. The gain reduction with six steering stations is no more than 20%, compared to 60% in case of undulator errors with the same number of steering stations.

With six steering stations, the rms beam wander is less than 30 μm, and the main cause for gain reduction is the phase shake. One way to reduce the phase shake is by increasing the β-function. The simulations of which the results are shown in Fig. 3.3 have used a quadrupole strength of 4.5 T/m instead of the 9.9 T/m in previous calculations. With the present undulator design, such a change can be easily accomplished at a late stage. As a result, the β-function at 300 MeV has increased from 1 to 2 m. Due to the smaller phase-advance between steering stations (defined as L_D/β [rad], with L_D the distance between steering stations), the phase shake in this case has decreased. As a consequence, the gain reduction at 300 MeV with six correctors is only 30%, compared to 60% for a β-function of 1 m. The gain has decreased by almost a factor of

two compared to the results presented in Fig. 3.2 due to a smaller value of the Pierce parameter ρ. The minimum phase advance in Fig. 3.2 is 55^0, in Fig. 3.3, it is 27^0 for six correctors. The obvious conclusion is that when one includes a FODO-lattice, the phase advance between steering stations should not exceed 30^0. This is equivalent to a distance between correctors of $\beta/2$.

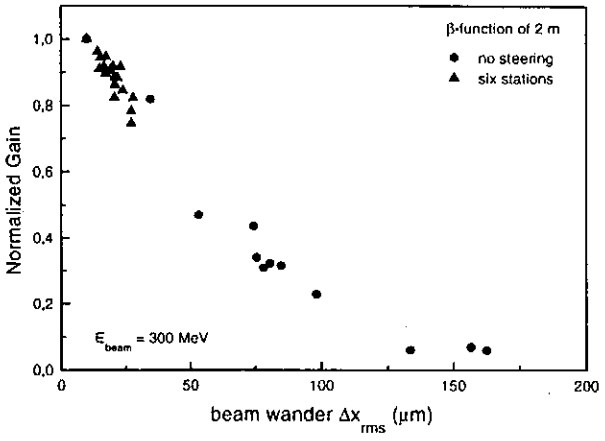

Figure 3.3: *The power gain after the first undulator module without (solid circles) and with six (solid triangles) steering stations as a function of rms electron beam wander. Calculations have been performed with a quadrupole strength of 4.5 T/m. All remaining parameters are as in Fig. 3.2.*

4. Conclusions

Calculations have been performed assuming the parameters as given in Table 3.1. The results of field error calculations have been expressed in terms the rms value of either of phase shake or beam wander. Simulations of peak field errors have shown that the undulator tolerances for the TTF-FEL are mainly related to the transverse overlap of the radiation field with the electron beam and the phase-shake related to this beam wander. The phase-shake for an on-axis electron beam turns out to be less important as long as the rms peak field error does not exceed 0.5%, as was shown by simulations of errors per period (Fig. 3.1), thus fixing the electron beam to the undulator axis. Straight forward calculations show that as long as $\Delta\psi_{rms} < \sigma_\gamma/(\gamma\rho\sqrt{3})$, with ρ the Pierce parameter (see Ref. 11), the gain reduction is small compared to the reduction due to energy spread.

Simulations of an undulator peak field error per half period have been performed with an rms error of 0.5% based on the previous calculations. The error per half period reduces the overlap between electron beam and radiation field. If one adds a random displacement of quadrupoles, the conclusions are virtually the same. A displacement between $\pm 50\,\mu$m shows a comparable rms beam wander as for a peak field error of 0.5%. The simulations show that the rms value of the electron beam wander should not exceed $0.2\,\sigma_{\rm beam}$. This corresponds to a second field integral of 10 T mm^2 for an electron beam radius of $57\,\mu$m.

In case the desired beam wander and phase shake can not be achieved, the electron trajectory can be aligned with the radiation field by steering stations. In all simulations, it is assumed that there is one station at the undulator entrance and one at the exit. These two are needed in order to be able to adjust transverse position and momentum from one undulator module to the next. The normalized gain is only 40% of the ideal gain in case of six stations and 70% in case of seven stations. With these seven stations, the beam wander is reduced to $25\,\mu$m. The total number of steering stations is approximately equal to one per gain length, with one additional one for matching at each undulator module entrance.

Including FODO-lattice, the phase shake can be reduced further by decreasing the phase advance of the electron beam between steering stations. This can be achieved by increasing the β-function. Increasing the β-function for the 300 MeV case from one to two meters, reduces the gain, but the normalized gain with six steering stations is in all cases larger than 70% of the ideal gain (see Fig. 3.3). Therefore, as a good approximations, the gain length increase is given by

$$\ell_g = \frac{\ell_g^{1D}}{1-R}\,, \tag{2}$$

with

$$R = \Delta\psi_{\rm rms} + \frac{1}{2}\left[\left(\frac{\Delta x_{\rm rms}}{\sigma_x}\right)^2 + \left(\frac{\Delta y_{\rm rms}}{\sigma_y}\right)^2\right]\,,$$

where R is calculated over a gain length, and the distance between steering stations is given by

$$L_D = \min\left(\ell_g^{1D}, \beta/2\right)\,. \tag{3}$$

References

1. "A VUV Free Electron Laser at the TESLA Test Facility: Conceptual Design Report", DESY Print TESLA-FEL 95-03, Hamburg, DESY, 1995.
2. Brian M. Kincaid, *J. Opt. Soc. Am. B* **2** (1985) 1294.
3. H.D. Shay and E.T. Scharlemann, *Nucl. Instr. Meth.* **A272** (1988) 601.
4. D.C. Quimby and C.J. Elliott, *Nucl. Instr. Meth.* **A296** (1990) 451.
5. B.L. Bobbs, G. Rakowsky, P. Kennedy, R.A. Cover and D.Slater, *Nucl. Instr. Meth.* **A296** (1990) 574.
6. John Vetrovec, *IEEE J. Quant. Electron.* **QE-27** (1991) 2673.
7. L.H. Yu, S. Krinsky, R.L. Gluckstern and J.B.J. Zeijts, *Phys. Rev. A* **45** (1992) 1163.
8. Richard P. Walker, Interference Effects in Undulator and Wiggler Radiation Sources Sincrotrone Trieste ST/M-93/3, (1993).
9. H.P. Freund and R.H. Jackson, *Nucl. Instr. Meth.* **A331** (1993) 461.
10. A. Friedman, S. Krinsky and L.H. Yu, *IEEE J. Quant. Electron.* **QE-30** (1994) 1295.
11. R. Bonifacio, C. Pellegrini and L.M. Narducci, *Opt. Commun.* **53** (1985) 197.
12. T.-M. Tran and J.S. Wurtele, *Comp. Phys. Commun.* **54** (1989) 263; P. Jha and J.S. Wurtele, *Nucl. Instr. and Meth.* **A331** (1993) 477.
13. B. Faatz, J. Pflüger and P. Pierini, *Nucl. Instr. Meth.* **A375** (1996) 441.

Possible Application of X-ray Optical Elements for Reducing the Spectral Bandwidth of an X-ray SASE FEL

J. Feldhaus[a], E.L. Saldin[b], J.R. Schneider[a], E.A. Schneidmiller[b], M.V. Yurkov[c]

[a] *Hamburger Synchrotronstrahlungslabor (HASYLAB) at Deutsches Elektronen-Synchrotron (DESY), Notkestrasse 85, D-22607 Hamburg, Germany*

[b] *Automatic Systems Corporation, 443050 Samara, Russia*

[c] *Joint Institute for Nuclear Research, Dubna, 141980 Moscow Region, Russia*

Abstract

A new design for a single pass X-ray SASE FEL is proposed. The scheme consists of two undulators and an X-ray monochromator located between them. The first stage of the FEL amplifier operates in the SASE linear regime. After the exit of the first undulator the electron bunch is guided through a non-isochronous bypass and the X-ray beam enters the monochromator. The main function of the bypass is to suppress the modulation of the electron beam induced in the first undulator. This is possible because of the finite value of the natural energy spread in the beam. At the entrance to the second undulator the radiation power from the monochromator dominates significantly over the shot noise and the residual electron bunching. As a result, the second stage of the FEL amplifier operates in the steady-state regime. The proposed scheme is illustrated for the example of the 6 nm option SASE FEL at the TESLA Test Facility under construction at DESY. The spectral bandwidth of such a two-stage SASE FEL ($\Delta\lambda/\lambda \simeq 5\times10^{-5}$) is close to the limit defined by the finite duration of the radiation pulse. The average spectral brilliance is equal to 2×10^{24} photons/(sec×mrad^2×mm^2×0.1 % bandw.) which is by two orders of magnitude higher than the value which could be reached by the conventional SASE FEL.

1. Introduction

In this paper we propose a modification of a single pass X-ray SASE FEL allowing to reduce significantly the bandwidth of the output radiation. The proposed scheme consists of two undulators and an X-ray monochromator located between them (see Fig. 1). The first undulator operates in the linear regime of amplification starting from noise and the output radiation has the usual SASE properties. After the exit of the first undulator the electron is guided through a bypass and the X-ray beam enters the monochromator which selects a narrow band of radiation. At the entrance of the second undulator the monochromatic X-ray beam is combined with the electron beam and is amplified up to the saturation level.

The electron micro-bunching induced in the first undulator should be destroyed prior to its arrival at the second one. This can be achieved because of the finite value of the natural energy spread in the beam and by applying a special design of the electron bypass. At the entrance of the second undulator the radiation power from the monochromator dominates significantly over the shot noise and the residual electron bunching, so that the second stage of the FEL amplifier will operate in the steady-state regime when the input signal bandwidth is small with respect to the FEL amplifier bandwidth.

The monochromatization of the radiation is performed at a low level of radiation power which allows one to use conventional X-ray optical elements for the monochromator design. X-ray grating techniques can be used successfully down to wavelengths of several Å and at shorter wavelengths crystal monochromators could be used. Integral losses of the radiation power in the monochromator are relatively small because grazing incidence optics can be used. The proposed

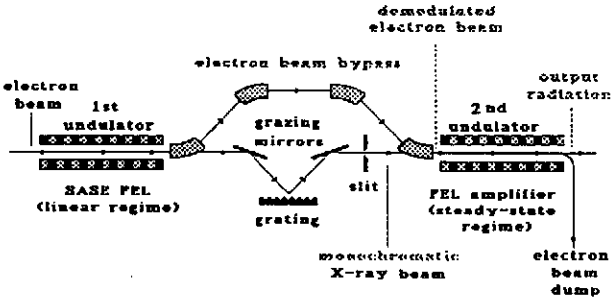

Fig. 1: The principal scheme of a single-pass two-stage SASE X-ray FEL with monochromator.

scheme possesses two significant advantages. First, it reveals a perspective to achieve monochromaticity of the output radiation close to the limit given by the finite duration of the radiation pulse and to increase the brightness and brilliance of the SASE FEL. Second, shot-to-shot fluctuations of the output radiation power could be reduced to less than 10 % when the second undulator section operates at saturation. Since it is a single bunch scheme, it does not require any special time diagram for accelerator operation.

2. Principle of operation of a two stage SASE FEL

After the first undulator the electron beam is guided through a bypass and the X-ray beam enters the monochromator. The functions of the electron bypass consist in making the path lengths of the electron and the radiation beams equal, and in suppressing the modulation of the electron bunch produced in the first undulator.

Let us consider the simplest non-isochronous scheme of the electron bypass composed of three magnets which is symmetrical with respect to its center. The trajectory of the electron beam in the bypass has the shape of an isosceles triangle with the base equal to L, the distance between the two undulators. The angle adjacent to the base, θ, is considered to be small, $\theta \ll 1$. We assume that the particles in the electron beam have a Gaussian energy distribution: $f(P) = (\sqrt{2\pi}\sigma_\mathcal{E})^{-1}\exp(-P^2/2\sigma_\mathcal{E}^2)$. Here $P = (\mathcal{E} - \mathcal{E}_0)/\mathcal{E}_0$, $\sigma_\mathcal{E}$ is the standard deviation, $\mathcal{E}_0$ is the nominal energy of the particles. We also assume that at the entrance of the bypass the electron bunch's density and energy are modulated with wavelength λ equal to that of the FEL radiation. At the exit of the bypass the modulations are suppressed by a factor of

$$D = \exp(-4\pi^2\sigma_\mathcal{E}^2\theta^4 L^2/2\lambda^2) \ . \qquad (1)$$

Let us consider the specific numerical example with $\sigma_\mathcal{E} \simeq 0.1$ %, $\lambda \simeq 6$ nm, $\theta \simeq 1^0$ and $L \simeq 10^3$ cm. According to expression (1), the electron beam modulations are suppressed by a factor of $D = \exp(-5000000)$. Thus, the initial modulation of the electron beam at the entrance into the second undulator is given by the shot noise only.

To provide effective operation of a two-stage SASE FEL, the input radiation power $P_{\rm in}^{(2)}$ at the entrance to the second undulator must exceed significantly the effective power, $P_{\rm shot}$, of shot noise. When the power gain in the first undulator is equal to $G^{(1)}$ and the transmission factor of the monochromator is equal to $T_{\rm m}$, one can write: $P_{\rm in}^{(2)}/P_{\rm shot} = G^{(1)}T_{\rm m}$. The transmission factor $T_{\rm m} = R_{\rm m}K_s$ is defined by the product of the integral reflection coefficient $R_{\rm m}$ of the mirrors and the dispersive element, and the coefficient K_s describing the radiation losses at the exit slit of the monochromator: $K_s = (\Delta\lambda/\lambda)_{\rm m}/(\Delta\lambda/\lambda)_{\rm SASE}$, where $(\Delta\lambda/\lambda)_{\rm m}$ is the resolution of the monochromator and $(\Delta\lambda/\lambda)_{\rm SASE}$ is the radiation bandwidth of the SASE FEL at the exit of the first undulator. As a result, one obtains the following criterium for the power gain in the first undulator: $P_{\rm in}^{(2)}/P_{\rm shot} = G^{(1)}R_{\rm m}K_s \gg 1$.

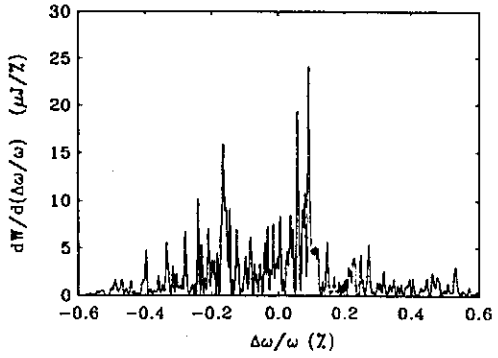

Fig. 2: Spectral distribution of the radiation pulse at the exit of the first undulator.

In addition, the resolution of the monochromator should satisfy the following conditions: $\lambda/\pi\sigma_z < (\Delta\lambda/\lambda)_{\rm m} \ll (\Delta\lambda/\lambda)_{\rm SASE}$. The lower limitation on $(\Delta\lambda/\lambda)_{\rm m}$ is due the fact that the length of the longitudinal coherence of the radiation can not be larger than the length of the electron bunch, σ_z.

The amplification process in the first undulator leads to an energy modulation in the electron beam. After passing the bypass this energy modulation transforms into additional energy spread in the electron beam: $\Delta\sigma_\mathcal{E} \simeq \rho[G^{(1)}/G_{\rm sat}({\rm SASE})]^{1/2}$, where ρ is the saturation parameter [3, 4], $G_{\rm sat}({\rm SASE})$ is the power gain of SASE FEL at saturation. For effective operation of the second stage of the FEL amplifier, this induced energy spread should be small; $\sigma_\mathcal{E}^2 \ll \rho^2$, which leads to condition: $G^{(1)} \ll G_{\rm sat}({\rm SASE})$. This relation means that the first stage of the SASE FEL must operate in a linear high-gain regime.

When optimizing the two-stage FEL one should take into account significant shot-to-shot fluctuations at the exit of the monochromator. If the resolution of the monochromator is $(\Delta\lambda/\lambda)_{\rm m} \simeq \lambda/\pi\sigma_z$, the shot-to-shot fluctuations of the radiation power at the exit of the monochromator are about one order of magnitude (see Fig.2). Our estimations show that the level of the radiation power at the exit of the monochromator (averaged over shot-to-shot fluctuations) must at least be by two orders of magnitude higher than the effective power of shot noise.

In conclusion to this section we combine all the con-

Table 1: Parameters of the conventional SASE FEL at DESY

Electron beam	
Energy, $\mathcal{E}_0$	1000 MeV
Peak current, I_0	2500 A
rms bunch length, σ_z	50 μm
Normalized rms emittance , ϵ_n	2π mm mrad
rms energy spread	0.1 %
External β-function,	300 cm
rms transverse beam size	57 μm
Number of bunches per train	7200
Repetition rate	10 Hz
Undulator	
Type	Planar
Length of undulator, L_w	20 m
Period, λ_w	2.73 cm
Peak magnetic field, H_w	4.97 kGs
Radiation	
Wavelength, λ	6.4 nm
Bandwidth, $(\Delta\lambda/\lambda)_{SASE}$	0.5 %
rms angular divergence	15 μrad
rms spot size	90 μm
autocorrelation time, $\tau_{1/2}$	3 fs
Power average over pulse	5 GW
Flash energy	1.5 mJ
Average power	100 W
Average spectral brilliance	2×10^{22} Phot./(sec$\times$ mrad$^2\times$mm$^2\times$ 0.1% bandw.)

ditions necessary and sufficient for the effective operation of a two-stage SASE FEL:

$$P_{in}^{(2)}/P_{shot} = G^{(1)} R_m (\Delta\lambda/\lambda)_m/(\Delta\lambda/\lambda)_{SASE} > 10^2 ,$$

$$\lambda/\pi\sigma_z < (\Delta\lambda/\lambda)_m \ll (\Delta\lambda/\lambda)_{SASE} ,$$

$$G^{(1)} \ll G_{sat}(\text{SASE}) . \qquad (2)$$

3. Numerical example

The operation of a two-stage SASE FEL is illustrated for the 6 nm option of the SASE FEL which is under construction at DESY (see Table 1) [1]. For our calculations we have used the same parameters for the electron beam and the undulator.

Parameters of the first stage of the SASE FEL are presented in Table 2. It operates in a linear regime with a power gain $G^{(1)} = 10^5$. This value is 1000 times less than the power gain at saturation, $G_{sat}(\text{SASE}) \simeq 10^8$ (see Table 1). Spectral characteristics of the output radiation at the exit of the first stage are presented in Figs.2 (see [6, 7]).

Table 2: Parameters of the first stage of the two-stage SASE FEL

Mode of operation	SASE, linear amplification
Effective power of shot noise, P_{shot}	100 W
Length of undulator, L_w	12 m
Effective gain, G	10^5
Output radiation	
Wavelength, λ	6.4 nm
Bandwidth , $(\Delta\lambda/\lambda)_{SASE}$	0.5 %
Autocorrelation time, $\tau_{1/2}$	2 fs
rms spot size	40 μm
rms angular divergence	18 μrad
Peak power	50 MW
Power average over pulse,	10 MW
Flash energy	3 μJ
Average power	0.2 W

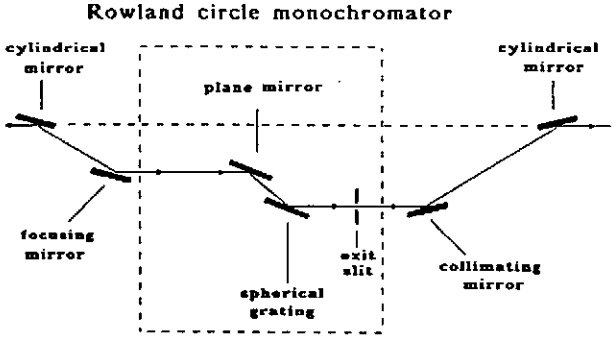

Fig. 3: Layout of a grating monochromator for the TTF FEL.

The monochromator for the TTF-FEL should be able to select any energy between 50 eV and 200 eV with a resolution $(\Delta\lambda/\lambda)_m \simeq 5 \times 10^{-5}$ in order to resolve the fine structure shown in Fig. 2. The optics needed to couple the radiation in and out of the monochromator would be particularly simple and symmetric if a monochromator design was chosen whose magnification would be independent of wavelength. Therefore, a Rowland circle grating monochromator appears to be ideally suited for this purpose since the magnification of the spherical grating is always unity, independent of wavelength. The specific design of F. Senf et al. [5] has the additional advantage that the distance between the entrance and the exit slit is constant and the directions of the in- and outgoing beams are fixed, leading to a straightfor-

Table 3: Parameters of the second stage of the two-stage SASE FEL

Mode of operation	Steady-state, saturation
Input power, $P_{in}^{(2)}$	10^4 W
Length of undulator, L_w	16 m
Gain, G	10^6
Output radiation	
Wavelength, λ	6.4 nm
Bandwidth , $\Delta\lambda/\lambda$	5×10^{-5}
rms angular divergence	15 μrad
rms spot size	90 μm
Autocorrelation time, $\tau_{1/2}$	300 fs
Peak power	5.3 GW
Flash energy	1.5 mJ
Average power	100 W
Average spectral brilliance	2×10^{24} Phot./(sec× mrad^2×mm^2× 0.1 % bandw.)

ward design as shown schematically in Fig. 3. A first estimation of the transmission shows that a value of the order of 10 % is realistic. For all mirrors we use carbon coatings and grazing angles of incidence of 4^0, giving a reflectivity of 90 % for each mirror. Assuming a grating efficiency of 15 % and five mirrors with 90 % reflectivity then gives a total transmission of nearly 9 %.

The parameters of the second stage of the SASE FEL are presented in Table 3. The average value of the input radiation power is 10 kW, which results in a saturation length of 16 m. The quality of the output radiation of the two-stage SASE FEL exceeds significantly that of the conventional SASE FEL (compare Tables 3 and 1).

The output radiation power of the two-stage SASE FEL is close to that of the conventional SASE FEL while the spectral bandwidth is by two orders of magnitude narrower. Thus, the spectral brightness and brilliance of the output radiation exceed the corresponding values of a conventional SASE FEL by two orders of magnitude. In addition, longitudinal coherence of the output radiation over the full radiation pulse is obtained which leads to an autocorrelation time $\tau_{1/2}$ (corresponding to a decrease of the first order correlation function by a factor of two) of about 300 fs .

Fig.4 shows that the value of the output radiation power is rather insensitive to the fluctuations of the input power when the second stage of the FEL amplifier operates near the saturation point.

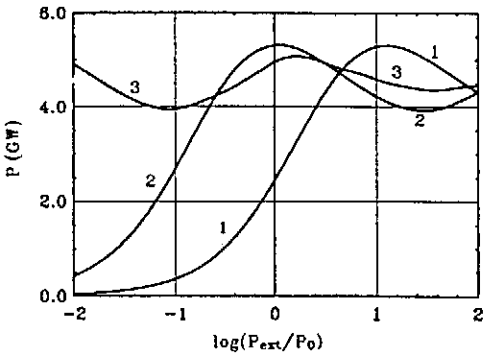

Fig. 4: Dependence of the output power on the input power for the FEL amplifier operation in the steady-state regime for different undulator lengths. (1): L_w = 14 m, (2): L_w = 16 m, (3): L_w = 20 m. Nominal input power $P_{in}^{(2)} = P_0$ = 10 kW.

4. Acknowledgement

We thank J. Rossbach for his interest in this work.

5. References

[1] "A VUV Free Electron Laser at the TESLA Test Facility at DESY. Conceptual Design Report", DESY print, TESLA-FEL 95-03, Hamburg (1995).

[2] J. Rossbach, Nucl. Instrum. and Methods **A375**(1996)269.

[3] R. Bonifacio, C. Pellegrini and L. Narducci, Opt. Commun. **50**(1984)373

[4] E.L. Saldin, E.A. Schneidmiller and M.V. Yurkov, Phys. Rep. **260**(1995)187.

[5] F. Senf, F. Eggenstein, and W. Peatman, Rev. Sci. Instrum. **63**(1992)1326.

[6] E.L. Saldin, E.A. Schneidmiller and M.V. Yurkov, DESY Print, TESLA-FEL 96-07, Hamburg(1996)

[7] P. Pierini and W. Fawley, Nucl. Instrum. and Methods **A375**(1996)332.

Photocathodes for RF photoinjectors

P. Michelato
INFN Milano-LASA, Via F.lli Cervi 201, 20090 Segrate (Milano), Italy

Abstract

Over the past ten years photocathodes have been extensively used as high brightness electron sources in RF guns. In this paper I present a general review about the alkali based high quantum efficiency (QE) photoemitters (e.g. Cs_3Sb, K_2CsSb and Cs_2Te), together with a comparative analysis of the different preparation procedures and the results obtained, both in the preparation chambers and in RF guns.

The need to increase the photocathode reliability has forced to get an R&D activity to go over the alchemy of photocathode preparation procedure. In this paper I will discuss the results so far obtained in different labs, both using traditional investigation strategy (e.g. QE and RF behavior) and by means of surface science techniques as AES (Auger Electron Spectroscopy) and XPS (X-ray Photoelectron Spectroscopy).

Alkali antimonide have been used at first in the RF gun due to the high QE response to the green light of the Nd:YLF second harmonic radiation. Measurements have confirmed the high reactivity of the alkali antimonide photocathodes to the residual gases: this fact make their use in RF guns not practical, mainly for the short lifetime.

Further investigations have shown that the choice of the substratum preparation procedure and chemical composition plays a fundamental role in the photocathode performances, both from the point of view of the QE and for the operative lifetime and ruggedness to gas exposition.

Cesium telluride (Cs_2Te) prepared on a molybdenum substratum seems to be, nowadays, the best compromise, in terms of preparation procedure reliability and ruggedness: now the characteristics and drawbacks of this material are well understood (e.g. the need of an UV laser source).

Future possible developments will be discussed. In particular the measurement and the control of the thermal emittance and the time response could be an important task.

1. Introduction

RF (Radio Frequency) photoinjectors are nowadays the most promising sources of high brightness and low emittance electron beams [1]. A photoinjector consists of a photoemissive material located in a high gradient RF accelerating structure: a laser beam illuminates the photocathode and the photoemitted electrons are promptly accelerated. In this way it is possible to control the spatial (charge distribution, current density etc.) and temporal (bunch length, phase with respect to RF etc.) characteristics of the emitted electrons. The fast energy gain, due to the location of the electron source inside the accelerating structure, gives the possibility to produce high brightness, short electron bunches [2].

Since the electron source is the photocathode, photoinjector performances and operative characteristics strongly depend on photoemitter characteristics. The general requirements for photocathode as RF gun electron sources are here summarized. A photocathode must have a fast response time, of the order of ps, in order to have a correct phase matching with the RF power in the injector. Moreover, to have high brightness beam, photocathode must be able to produce high current density (hundreds of amperes per square centimeter). Finally the photocathode must have a reasonable quantum efficiency and a long lifetime.

Unfortunately QE and lifetime requirements are in contrast and the choice of the photocathode is usually a compromise between high QE and long lifetime.

2. Overview on photocathodes

Generally speaking, photocathodes can be divided in two different groups: metallic photoemitters and semiconductors. Metallic photoemitters are robust, both from the residual gases contamination point of view and for electric breakdown problems, but they have a low QE value (of the order of 10^{-4} in the UV range) due to their high reflectivity and to electron-electron scattering that reduce the escape depth [3]. The e-e scattering may also increase the emittance of the photoemitted electrons [4].

Among semiconductor photoemitters, Cs_3Sb [3, 5] and K_2CsSb [3, 5] ($E_G + E_A$ about 2 eV) can be operated with visible light but are very sensitive to contamination and

Laboratory	QE % @ λ	Substrata	Operational life time a)	Pressure [mbar]	Resp. time [ps]	QE measurement technique	Emax MV/m	Ref.
• **CEA**								
Cs_3Sb	1.3 (@ 532 nm) [a]	Mo	-	10^{-10}	-	Low Voltage	25	[8]
K_2CsSb	3 (@ 532 nm) [a]	Mo	$T_{1/e}$>1 h	10^{-10}	-	Low Voltage	25	[9,10]
Cs_2Te	10 (@265 nm) [b]	Mo	-	10^{-10}	-	Low Voltage	25	[11]
• **CERN**								
Cs_3Sb	0.4 (@532 nm) [b]	-	-	10^{-7}	-	High Voltage	8 [c]	[12]
Cs_2Te	6 (@ 266 nm) [a]	Cu/Cu+Mo	$T_{1/e}$> 100	10^{-9}	~ ps	High Voltage	100	[13]
• **LANL**								
Cs_3Sb	4 (@527 nm) [a]	Mo	$T_{1/2}$<4 h	10^{-10}-10^{-9}	~ ps	Low Voltage	> 20	[14]
K_2CsSb	8 (@527 nm) [a]	Mo	$T_{1/2}$<4 h	10^{-10}-10^{-9}	~ ps	Low Voltage	> 20	[14]
Cs_2Te	13 (@263 nm) [a]	Mo	$T_{1/e}$>100 h	10^{-10}-10^{-9}	< 3 ps	Low Voltage	> 20	[14]
• **Milano**								
Cs_3Sb	9 (@ 543 nm) [b]	Cu	-	10^{-10}-10^{-9} [b]	-	Low Voltage	-	[15]
K_2CsSb	6 (@ 543 nm) [b]	S. Steel	-	10^{-11}-10^{-10} [b]	-	Low Voltage	-	[16,17]
Cs_2Te	13 (@ 254 nm) [b]	Mo	-	10^{-10}-10^{-9} [b]	-	Low Voltage	-	[18]
• **Twente**								
K_2CsSb	4 (@534 nm) [a]	Mo	$T_{1/2}$<2 h	10^{-9}	-	Low Voltage	28	[19]
Cs_2Te	20 (@ 254 nm) [b]	Mo	$T_{1/2}$>10 h	10^{-9}	-	Low Voltage	28	[20]

a) RF gun; b) Test System; c) HV DC test gun.

Tab. 1. Summary of the photocathode produced and used in different laboratories.

must be operated only in XUHV environments ($p < 10^{-10}$ mbar). Semiconductors with higher E_G value, such as CsI, are more robust but require the use of the radiation with λ shorter then 250 nm. Negative Electron Affinity (NEA) [6] photoemitters (as GaAs-Cs-O) can be used with visible light but they are still very sensitive to contamination. Moreover they usually have a longer response time due to the tail in the electron emission [7].

The alkali metal based photoemitters fulfill the majority of the requirements previously discussed. Different laboratories have tested and used them, both in R&D apparatus (preparation chambers and HV DC electron extractors) and in RF injectors. Tab. 1 shows a summary of the alkali based photocathodes used in the different labs, together with their characteristics and performances.

The main problem found in using photoemissive semiconductor film in RF gun is the short lifetime due to high sensitivity of these compounds to contamination and the related poisoning effects caused by the residual gases. Moreover an empirical approach to the preparation procedure optimization doesn't guarantee a good reliability of the film properties.

Therefore the effort done in the last years have been concentrated to go over these limitations and to understand and control the preparation procedure and the poisoning effects. To get that, new techniques have been applied, traditionally used in other fields, as AES (Auger Electron Spectroscopy) and XPS (X-ray Photoemission Spectroscopy). The use of these techniques is not trivial due to the extreme sensitivity of these materials both to vacuum conditions (e.g. less then 1 Langmuir of oxygen can destroy a K_2CsSb film [21]) and to the possible alterations induced in the film structure and composition by the same investigating technique (e.g. electron beam during the characterization of a polluted film).

3. Alkali antimonide

Alkali antimonide, and in particular Cs_3Sb and K_2CsSb, extensively used in photodiodes and photomultipliers tubes, have been the first photocathodes used in RF guns. In particular Cs_3Sb was the photocathode employed inside the first RF gun at LANL in 1988 [22]; in consequence of the high dark current in the gun, this

material was replaced by K_2CsSb [23].

As shown in the tab. 1 these photocathodes has been investigated by many labs but only CEA, LANL and Twente have successfully operate them in a RF gun.

Even if these photoemitters are largely used, the recipe for the fabrication is not well standardized and the formation process unknown. For instance Twente [19] and CEA produce this film starting from a thin layer of K_3Sb. Furthermore Milano has developed a recipe for K_2CsSb starting from Cs_3Sb [21]. The Milano recipe was studied and optimized using AES and step-by-step analysis during the cathode growth. A comparison between cathode prepared by CEA and Milano is discussed in [17]. As a matter of the fact, also the spectral responses of the cathodes used in different labs are not equal and this shows that the compounds produced are not the same.

Investigation about poisoning effect on cesium antimonide and potassium cesium antimonide compound has been done by LANL [24] , by CEA [10] and Milano [16], using traditional approach: cathodes are polluted by exposing them to oxygen, carbon dioxide, water, etc.. While methane and hydrogen have no effects on the cathode performances, carbon dioxide and oxygen produce an high degradation of the QE characteristic of the cathode. Also in these investigations, the use of AES allows to have important information. It is possible, for example, to investigate the influence of substratum cleanliness on the properties of the cathode that is to be prepared. In particular it has been shown that is not possible to remove completely a cathode from the substrate only by an heating process (after 1 hour @ 600 °C Cs, K and Sb are still present at the surface). Moreover a heavily poisoned cathode (e.g. with oxygen) is harder to be cleaned. These results show that the properties of a cathode depend on the history of its substratum. An effectively way to clean-up the surface is Ar ion bombardment [25].

4. Cesium iodide

This material has an energy gap of 6.3 eV, forcing the use of VUV radiation such as the fifth harmonic of Nd lasers in order to have a reasonable QE. Notwithstanding this, CsI is an easy to be prepared film (can be evaporated directly from CsI crystals). It was used at CERN (evaporated on a copper substrate) as a possible photocathode for the CTF gun. Unfortunately it is affected by some kind of charge saturation effects when is used inside a RF gun [12].

5. Cesium telluride

As mentioned before, one of the major drawback in the use of alkali antimonides is their sensitivity to gas exposure. In the last two year, CERN and LANL have partially overcome this limitation, moving towards the use of cesium telluride (Cs_2Te).

Cs_2Te is a semiconductor with an $E_G + E_A$ of about 3.5 eV and is used as photocathode in solar blind UV detectors. A detailed investigation on Cs_2Te photoelectron energy distribution can be found in the Ph.D. thesis of R. O. Powell [26,27] and in Taft and Apker [28]. Unfortunately there is a lack of information about its formation process and its reactivity to gas exposure.

Due to the high E_G, Cs_2Te has an high resistivity [3]. Nevertheless CERN and LANL have demonstrated that it produces high current density, high brightness electron bunches when used on a metallic substrate. The dark current measurements on the Los Alamos AFEL injector have shown values lower then those obtained with K_2CsSb [29] Furthermore LANL has measured the ratio of an emittance figure of merit between K_2CsSb and Cs_2Te: they have not found any significant difference [29]. For these reasons, Cs_2Te is, at this time, the best compromise in terms of robustness, quantum efficiency and lifetime.

In the following I will illustrate some results about the formation process, the reactivity with gases and the rejuvenation effect. The last mentioned effect may be interesting both for the use of Cs_2Te in RF guns (it could increase the cathode lifetime) and for the physics of the phenomenon itself.

5.1 Cs_2Te Production

Cesium telluride production goes through the formation of some compounds with different Cs to Te stoichiometric ratio. The formation of a new compound during the photocathode growth is highlighted by a change in the photocurrent behavior, moving from an increasing slope to a "plateau" [30]. The principal parameters that influence the cathode growth are the substratum material and its temperature during the cathode formation.

Using XPS and AES, Cs_2Te formation has been investigated, by a step-by-step analysis of the cathode during its growth, stopping the preparation procedure at each "plateau" and performing an analysis of the new compound. This kind of approach has been done on cathode prepared at room temperature on copper (CERN like) and on molybdenum substratum, both at room temperature and at 120 °C (cathode similar to the one in use at LANL). While a cathode grown of on molybdenum substrate allows the formation of a "thick" (few tens of nm) Cs_2Te film with the right stoichiometric ratio along all its depth, in the copper case the tellurium diffuses in the substrate and so a more complicated structure is obtained. In particular, in the latter case, Cs_2Te film is present only in a very thin layer at the surface [18]. The substratum affects not only the structure of the photocathode but also its QE value: a cathode grown on Mo has higher QE. In spite of this fact, the different photocathodes have about the same operative lifetime.

5.2 Cs_2Te poisoning and rejuvenation

As previously discussed Cs_2Te cathode are more robust than the alkali antimonide one. Information about Cs_2Te robustness and poisoning are in [18, 31]. These investigations have confirmed that Cs_2Te is at least 2-3 order of magnitude less sensitive to O_2 exposition [32] in respect with K_2CsSb and that is barely sensitive to CO_2 and not affected by CO and methane [18].

LANL, at first, has mentioned the possibility to rejuvenate Cs_2Te polluted films [31]. Investigations on this phenomenon have highlighted that by contemporaneously heating (at about 220 °C) and illuminating with UV radiation (λ = 254 nm) a Cs_2Te poisoned cathode is possible to rejuvenate it: heating and UV radiation (few tens of μW) must be present at the same time otherwise this effect doesn't take place. XPS measurements of Cs_2Te polluted films has highlighted that oxygen is bound to cesium and that during the rejuvenation process we can partially go back to a not polluted Cs_2Te films [18]. A detailed discussion on these themes is also presented at this conference [33]. This process could balance poisoning effects and extend the operative lifetime of the cathode in the RF guns.

6 Future developments

The results so far obtained on the photocathode properties must be applied and developed in order to fulfill the requirements from the new sources for linac based XUV FEL and those from the new acceleration techniques (plasma accelerators). In particular:

- the request of very low emittance beams (i.e. few π mm.mrad) forces some investigations on the thermal emittance of the photoemitted electrons. The Milano collaboration has planned to perform an angular resolved photoelectron spectroscopy in order to measure the thermal emittance [32]; the use of oriented crystals could eventually help in having a lower emittance value from the cathode.
- the photocathode response time is another critical parameters. Requirements on time response in the femtosecond regime are mandatory to apply photoinjector as electron sources in plasma accelerator. In this case, the electron bunch must be inside the plasma bucket and this requires very short electron bunches.
- finally, for TeV colliders, fast sources of polarized electron are very welcome. Nowadays the only photocathode that delivers spin polarized electron bunches is the strained GaAs. Unfortunately this photocathodes has some drawbacks as long response time, low QE value and the charge limit effect [34].

7 Acknowledgments

The author would like to thank D. Sertore for his help and advice during the preparation of this paper.

References

[1] C. Travier, Nucl. Instr. and Meth. A 340 (1994), 26.
[2] R. L. Sheffield, Proc. Particle Accelerator Conference, 1995, Dallas, 882.
[3] A. H. Sommers, Photoemissive materials, (Kriger, NY, 1980).
[4] W. E. Spicer and A. Herrera-Gomez, Modern Theory and Application of Photocathodes, 1993 Int. Symp. on Imaging and Instrumentation, San Diego, CA, July 11-16, 1993.
[5] Philips, "Photomultiplier Tubes", D-PMT-CAT93.
[6] J. E. Clendenin et al., Proc. Particle Accelerator Conference 1993, Washington D.C., 2973.
[7] A. V. Aleksandrov et al., Nucl. Instr and Meth. A340 (1994), 118.
[8] P. Balleyguier et al., Nucl. Instr. and Meth. A 304 (1991), 308.
[9] R. Dei-Cas et al., Nucl. Instr. and Meth. A 318 (1992), 121.
[10] F. Sabary, Proc. "VI Journees d'etudes sur la photoemision a fort courant", 1994, LAL/RT 94-04.
[11] F. Sabary, Proc. "VII Journees d'etudes sur la photoemision a fort courant", Sept. 1995, Universitè J. Fourier, Grenoble, France, ed. J. M. Dolique.
[12] E. Chevally et al., Nucl. Instr. and Meth. A 340 (1994), 146.
[13] R. Bossart et al., Proc. Particle Accelerator Conference 1995, Dallas, 719.
[14] S. H. Kong et al., Nucl. Instr. and Meth. A 358 (1995), 275.
[15] P. Michelato et al., Nucl. Instr. and Meth. A340 (1994), 176.
[16] P. Michelato et al., Proc. European Particle Accelerator Conference 1994, London, 1456, ed. World Scientific.
[17] A. di Bona et al., submitted to Nucl. Instr. and Meth.
[18] A. di Bona et al., J. App. Phys., in press.
[19] Van Oerle et al., Nucl. Instr. and Meth. A 358 (1995), 287.
[20] B.M. van Oerle et al., paper at this conference.
[21] P. Michelato et al., Proc. Particle Accelerator Conference 1995, Dallas, 1079.
[22] R. L. Sheffield et al., Nucl. Instr. and Meth. A 272 (1988), 222.
[23] P. G. O'Shea et al., AIP Conf. Proc., 279 (1993), 743.
[24] R. W. Springer and B. J. Cameron, Nucl. Instr. and Meth. A 318 (1992), 396.
[25] S.Valeri et al., Proc. European Particle Accelerator Conference 1994, London, p. 1459, ed. World Scientific.
[26] R. O. Powell, Ph.D. thesis, Stanford University, 1973.
[27] R. O. Powell et al., Phys. Rev. B. vol. 8 (8), 1973.
[28] E. Taft and L. Apker, J. Opt. Soc. Am. 43 (1953), 81.
[29] S. H. Kong et al., Nucl. Instr. and Meth. A 358 (1995), 284.
[30] A. di Bona et al., Proc. European Particle Accelerator Conference 1995, Barcelona.
[31] S. H. Kong et al., J. Appl. Phys. 77 (11) 1995, 6031.
[32] P. Michelato et al., Proc. European Particle Accelerator Conference 1995, Barcelona.
[33] P. Michelato et al., "Characterization of Cs2Te photoemissive film: formation, spectral responses and pollution", presented at this Conference.
[34] H. Tang et al.,Proc. European Particle Accelerator Conference 1994, London, 46, World Scientific.

Characterization of Cs_2Te photoemissive film: formation, spectral responses and pollution

P. Michelato, C. Pagani, D. Sertore
INFN Milano-LASA, Via F.lli Cervi 201, 20090 Segrate (Milano), Italy

A. di Bona, S. Valeri
Lab. SESAMO, Dip. Fisica-INFM, Via Campi 213/A, 41100 Modena, Italy

Abstract

In the framework of the TTF (Tesla Test Facility) collaboration for the Injector II, we present a study on the formation and characterization of photoemissive films of Cs_2Te grown on Mo substrata. In particular we are interested in relating the quantum efficiency (QE) to the preparation procedures used to obtain the photoemissive films. Using AES and XPS techniques we follow the growth of the evaporated materials (Te and Cs) into a film by a "step by step" analysis, observing the formation of different compounds before obtaining a stoichiometric Cs_2Te. The spectral response of the emissive layers is measured in the wavelength range 254 nm - 514 nm using both a high pressure mercury lamp and CW lasers.

In view of the applications of this photoemitter it is important to know the effect of gas pollution on a photoemitting film prepared with a standard procedure. Since oxygen is one of the most reactive gases, the influence of its contamination on Cs_2Te films has been choosen as representative of QE degradation. An exposure to $5 \cdot 10^{-5}$ mbar s of oxygen is enough to reduce the QE by one order of magnitude. XPS technique has been used to study the effects of the oxidation.

The "rejuvenation" effect (recovery of QE after oxygen exposure) produced by the contemporary action of heating and illumination with 254 nm radiation from a mercury lamp is investigated too.

The results obtained in this work allow to produce reproducible and reliable photocathode (QE = 9-10 % @ 254 nm), to comprehend the cathode formation steps and to have an initial understanding of the pollution and rejuvenation mechanisms.

1. Introduction

Photocathodes illuminated by pulsed light sources are nowadays employed as electron sources in RF guns[1]. RF guns provide high brightness electron beams as required by the future linac-based Free Electron Laser in the X-UV domain and electron-positron TeV collider. The main requirements for the photoemitter are: high current density, good time stability of the Quantum Efficiency (QE), long operative lifetime and fast response time (picosecond or subpicosecond range). Several photoemissive materials are available nowadays with different characteristics [2]. The most promising is cesium telluride (Cs_2Te), a semiconductive material used as solar blind detector [3] and as reference standard for ultraviolet (UV) light intensity measurement[4]. Taft and Apker [5] and Powell [6] performed a detailed study of the photoemissive properties of Cs_2Te. They measured the spectral responses of this photoemitter, the energy distribution of the photoelectrons and gave some information about its band structure. Unfortunately few investigation on the formation process and pollution are available. The knowledge of these characteristics is important in order to guarantee the photocathode requirements before highlighted.

In this paper we discuss about the influence of the substratum material and temperature on the cathode properties. An analysis of the cathode formation process by XPS (X-ray Photoelectron Spectroscopy) and AES (Auger Electron Spectroscopy) coupled with Ar^+ depth profiling is presented.. Pollution produced by different gases (carbon monoxide, carbon dioxide and oxygen) and "rejuvenation" effect [7], *i.e.* the recovery of the photoemissive properties after pollution, are investigated too.

2. Experimental

Cs_2Te film are produced in UHV condition, being the pressure in the low 10^{-11} mbar range. A gas inlet system allows to pollute the cathodes. The gas composition is measured by an RGA, QMG 112 Balzers.

The photocathode is grown on Mo substrate kept at 120 °C. The standard recipe asks for a preliminary deposition of 10 nm of tellurium with a rate of 1 nm/min and then Cs with the same rate. During the cesium

evaporation, the cathode is illuminated by 253.7 nm radiation: the photocurrent till a maximum value. At this point the cathode is complete formed, cesium evaporation stopped and the cooling of the substrate begun. The photocathode thickness is about 25 nanometers.

The light sources used to illuminate the cathode are either an high pressure mercury lamp or low power CW lasers (He-Ne and a multilines Ar^+).

The Auger emission is excited by an electron beam operating at 3 keV, with a current of 1 μA over a spot area of 30 μm x 30 μm. Auger spectra are obtained by using a single pass Cylindrical Mirror Ananlyzer (CMA) operating at 0.6 % relative resolution and in the first derivative mode (modulation voltage of 15 V peak-to-peak). An Ar^+ ion gun allows the Auger depth-profiles, operating at 1 keV, current density 30 μA/cm^2, rastered over a 2 mm x 2 mm area.

XPS spectra have been collected by a Leybold LHS-12 subsystem, equipped with a Concentric Hemispherical Analyser (CHA) and a non monochromatised, Mg X-ray source, tilted by 45° with respect to the CHA axis.

3. Results

3.1 Cathode formation

The first step towards an understanding of the photocathode formation process is the attainment of a reliable recipe that guarantees a reproducible cathode with a good Quantum Efficiency (QE) stable in time.

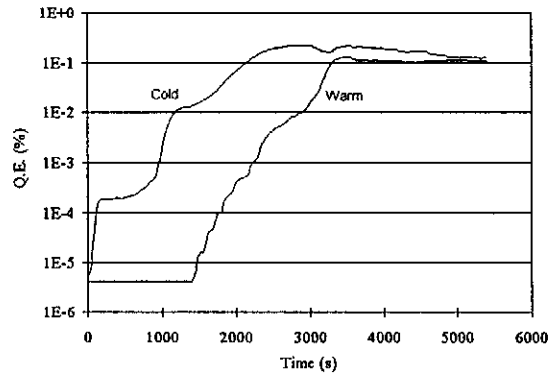

Fig. 1. QE behavior during Cs_2Te formation vs. Substratum temperature.

A preliminary works has been done to evaluate the influence of the substratum temperature during the cathode growth on the photocathode QE characteristic. Fig. 1 shows the QE behavior of cathodes grown respectively on a substratum kept at room temperature (23 °C) and at 120 °C. The "cold" procedure allows to have higher QE value at the end of the formation procedure but less stable in time. Instead of that, the "warm" recipe furnishes lower QE value but stable in time. The QE value of the "cold" recipe after few hours is quite the same obtained with the "warm" procedure. The photocathode QE stability we get with the "warm" recipe has been observed also in operative condition inside a linac [8].

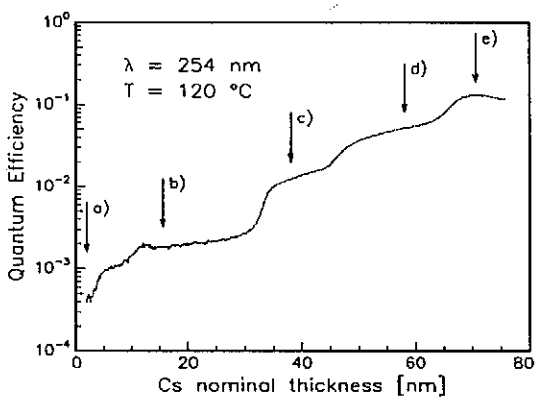

Fig. 2 QE vs. cesium thickness during the Cs_2Te formation. The letters indicates the XPS analysis step.

Following the recipe with warm substratum we obtain cathodes with a QE at 253.7 nm of 9-10 %. In Fig. 2 we report the QE evolution during the cesium deposition. The deposition starts at (a), then the QE evolves through (b)-(d) and then the cathode is formed when the photocurrent is maximum (e). XPS step-by step analysis showed that the changes in the photocurrent slope are due to the formation of different compounds [9]. In particular Fig. 3 shows the results obtained following the Te 3d XPS line features at each deposition step. Before cesium deposition (a), there is only pure Te (572.9 eV). After the evaporation of 20 nm of Cs (b), a second component in the spectrum appears at 572.2 eV. The peak ratio is about 1:1 indicating that about half of tellurium is reacted with cesium. The BE energy shift of -0.6 ÷ -0.7 eV indicates a charge transfer from Cs to Te valence shells. The two components now present are tellurium and a Cs-Te compound with a Cs to Te ratio of 1.2. A further Cs deposition (c) produces an increase $Cs_{1.2}Te$ component, a decrease of pure Te and the growth of a new structure at +0.8 eV respect to covalent Te. In correspondence with the evaporation of 60 nm of Cs (d), we have the presence of three components: pure Te, $Cs_{1.2}Te$ and a new line at 571.0 ± 0.1 eV characterized by a Cs to Te ratio x higher than 1.2. The cathode formation is complete with the evaporation of about 70 nm of Cs (e). Now the baricentrum of the full 3d Te line (571.5 eV) is between the $Cs_{1.2}Te$ and the Cs_xTe compound. If we assume that the (e) phase is the Cs_2Te compound, than we can ascribe the Cs_xTe component to a compound with a Cs to Te ratio higher that 2.

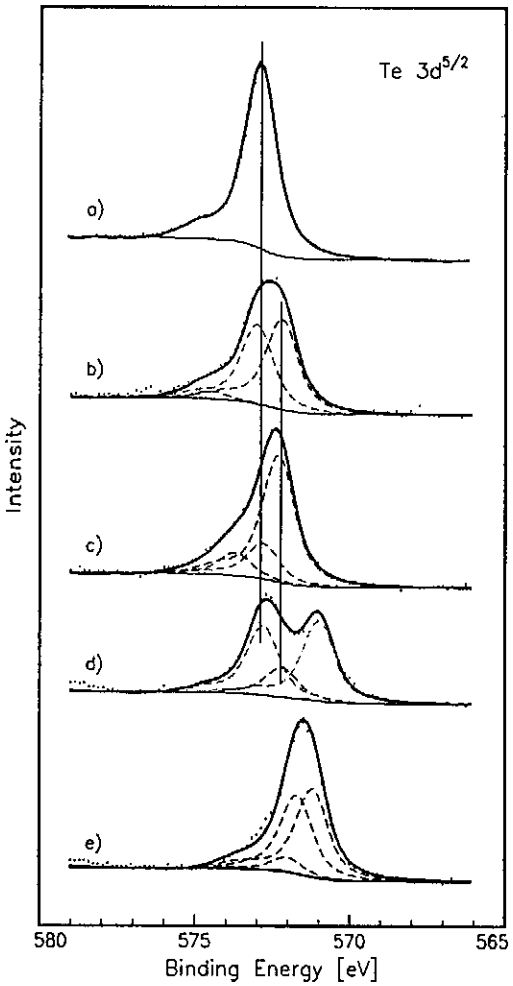

Fig. 3. Evolution of Te 3d line at different cathode formation step. The letter corresponds to a formation process phase as shown in Fig. 2.

Fig. 4 reports a depth profile of the completed cathode showing the good uniformity of the Cs-Te compound

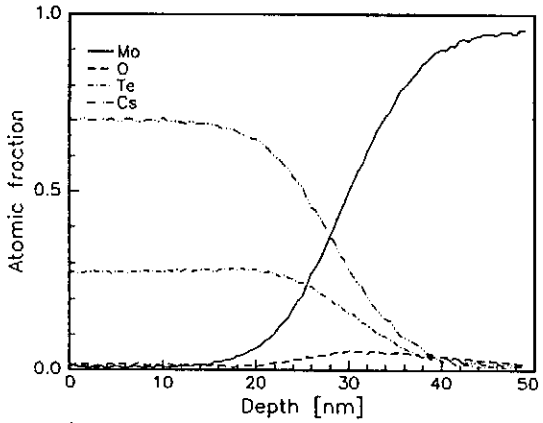

Fig. 4. Ar^+ Auger depth profile of Cs_2Te photocathode.

and the presence of Mo 20 nm under the surface. The presence of confined oxygen at the interface between the cathode and the substratum is probably due to an oxidized layer not removed by our cleaning procedure.

The analysis of the cathode spectral response is important to estimate the photoelectric threshold. As shown in Fig. 5, our cathode has the typical "shoulder" at low energy as previously observed both by Taft and Apker [5] and by Powell [6] in their studies on Cs_2Te. This feature lowers the threshold in the 2 eV range while the work function of the Cs_2Te is about 3.5 eV [6]. The Powell explanation for this shoulder is that more than one phase of Cs_2Te may exists as we haves hown with the XPS analysis.

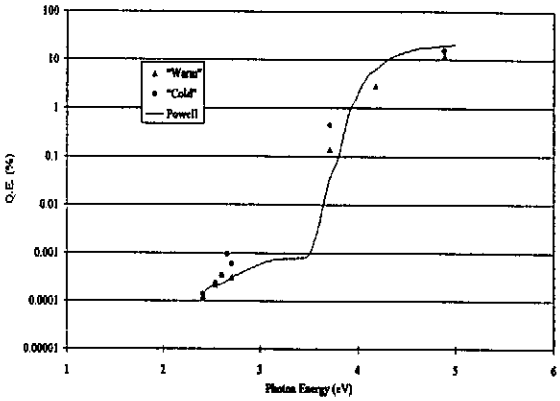

Fig. 5. Spectral response of Cs2Te photocathode compared with the Powell one.

3.2 Pollution

An important parameter for the use of photocathodes inside a RF gun is their operative lifetime, that is primarily affected by the vacuum condition inside the acceleration system. To investigate the pollution effect, we exposed the photocathode to carbon monoxide, carbon dioxide and oxygen, keeping the partial pressure of the gas in the low 10^{-9} mbar range. While carbon monoxide doesn't affect the photoemissive properties, carbon dioxide and oxygen produce a deterioration of the QE characteristic of the cathode, more pronounced with oxygen. Therefore to estimate the roughness of the cathodes, we exposed them to a few hundred Langmuir (1 L = 10^{-6} mbar's) of oxygen. Fig. 6 shows that the behavior of the QE is the same at both wavelength (253.7 nm and 334 nm). 1000 L exposure produces a decrease of one order of magnitude of the QE,. This value must be compared with 1 L necessary to reduce the QE of alkaly-antimonied of the same magnitude [10].

Poisoning the cathode with oxygen at higher partial pressure produces a different effect. If the oxygen pressure is in the 10^{-7} mbar range, the QE has, at first, a fast drop to a 1/e value with 15 L and then a slow decay

towards a saturation. This behavior could be interpreted as a passivation of the surface instead as a diffusion (exponential decay) and has been observed also in operative condition inside a RF gun [11]. The XPS analysis after a 100 L oxygen exposure shows that a thick layer of cesium oxide forms at the photocathode surface lowering the QE.

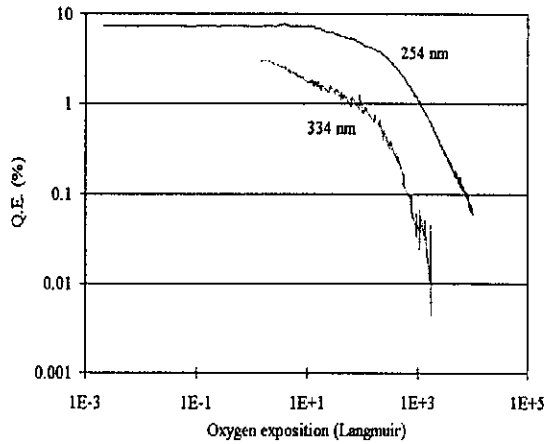

Fig. 6. Pollution of the cathode with oxygen at 253.7 nm and 334 nm.

3.3 Rejuvenation

An interesting properties of the cesium telluride photocathode is the possibility to rejuvenate it, *i.e.* to recovery its photoemissive properties after pollution as shown in Fig. 7.

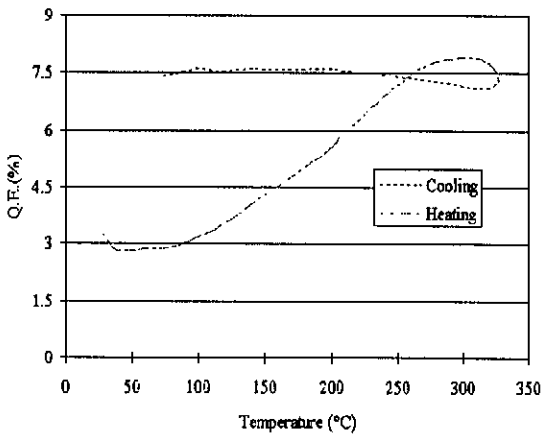

Fig. 7 Rejuvenation effect after pollution. The QE vs. temperature during the heating and cooling phases is reported.

As reported by Kong [7], a heating process after pollution assures a rejuvenation of the cathode. We found that the heating process alone does not gives effective rejuvenation. The rejuvenation effect is attained if, and only if, the polluted photocathode was completed formed and UV radiation (λ = 253.7 nm)is used to illuminate the cathode during the heating process. No rejuvenation is achieved using a radiation wavelength of 334 nm (hv = 3.7 eV) or longer.

We studied by XPS the changes induced in the photocathode by the rejuvenation process. The effect of the heating and radiating with UV light is a recovery of the complete photocathode Te 3d XPS line shape [9]. The rejuvenation process is effective also after the exposure of the photocathode to low vacuum condition (10^{-4} mbar for about eight hours).

Conclusion

A reliable recipe for the formation of reproducible Cs_2Te photocathode has been developed and photocathodes grown on warm substrata have stable QE. Different compounds are produced before the attainment of the right Cs to Te stoichiometric ratio.

As aspected, Cs_2Te photocathode is less sensitive to oxygen exposure than the alkaly-antimonied. Moreover the poising effect depends not only on the exposure time but also on the partial pressure of the gas.

Finally the rejuvenation effect is possible only if there is the contemporary presence of heating and UV radiation.

Reference

[1] C. Travier, Nucl. Instr. Meth. A **340** (1994), 26.
[2] E. Ottinger, Nucl. Instr. Meth. A **272** (1988), 264.
[3] R. W. Engstrom, ed., Photomultiplier Handbook (RCA Electro Optics and Devices, Lancaster, Pa., 1980).
[4] G. B. Fischer et al., App. Optics **12** (1973), 799.
[5] E. Taft and L. Apker, J. Opt. Soc. Am. **43** (1953), 81.
[6] R. A. Powell at al., Phy. Rev. B **8** (1973), 3987.
[7] S. H. Kong et al., Nucl. Instr. Meth. A **358** (1995), 276.
[8] S. H. Kong et al.., Nucl. Instr. Meth. A **358** (1995), 284
[9] A. di Bona et al., J. App. Phys., in press.
[10] P. Michelato et al., Proceedings of the fourth European Particle Accelerator Conference, vol.2 (1994), 1459.
[11] H. Braun et al., CERN CLIC note 293.

The undulator system for the VUV - FEL at the TESLA Test Facility

J. Pflüger, Y. M. Nikitina , B. Faatz, T. Teichmann

Hamburger Synchrotronstrahlungslabor HASYLAB
at Deutsches Elektronen-Synchrotron DESY
Notkestr85, 22603 Hamburg

Abstract

For the VUV - FEL at the TESLA Test Facility a 30m long undulator with a superimposed alternating sequence of focusing and defocusing quadrupoles (FODO lattice) is needed. A planar magnet structure with a fixed gap using permanent magnet technology has been proposed to realize both the undulator and the quadrupolar field.
The period length was chosen to be 27.3mm. At the nominal gap of 12mm a peak field of 0.5T can be reached. The maximum gradient that can be obtained with this structure is in excess of 20 T/m and is fully sufficient for the FODO lattice with the required parameters. The magnetic design is briefly described. The concept to subdivide the whole undulator into modules of about 4.5m length and still provide a smooth overall FODO lattice is presented.

Proofs: J. Pflüger, DESY, HASYLAB, Notkestr. 85, 22603 Hamburg, Germany

Contribution to the FEL 96 in Rome Version 22. August 1996

Undulator Design

At DESY in Hamburg a Free Electron Laser (FEL) for the VUV spectral range at 6.4nm using the principle of Self Amplified Spontaneous Emission (SASE) /1,2 / is under construction. It will use the electron beam of the TESLA Test Facility (TTF) /3/ and will be built in two stages:
Phase 1 will have a nominal energy of 380 MeV and will serve as a system test for the superconducting accelerator and a proof of principle for the SASE FEL. Conservatively we shall assume only 300MeV throughout this paper. In this case an undulator length of 14.33 m is sufficient. In Phase 2 the energy will be raised to 1 GeV and the undulator needs to be extended to the full length of 28.67 m. For practical reasons it has to be subdivided into modules of about 4.5m length which can be handled and manufactured with the required accuracy. There has to be a gap between undulator sections of about 0.3m for beam position monitors and other diagnostic equipment. The undulator design for Phase 1 and 2 is identical. Fig 1 shows a schematic view of the undulator section for the Phase 1 setup which will use three modules. Details and exact numbers can be seen in Tables 1 and 2.

An alternating quadrupole (FODO) lattice which consists of sections with positive and negative gradient separated by focusing free spaces is needed to avoid widening of the beam over the undulator length due to its divergence. The undulator therefore has to combine two functions:

1. It has to provide the sinusoidal field so that the FEL process can take place.
2. It simultaneously has to provide the alternating gradient field of about ±20 T/m for the FODO lattice which is superimposed to the undulator field

Permanent magnet (PM) technology using state of the art NdFeB magnet material has been chosen for the undulator /4-7/. Fig 2 shows a schematic 3-D view of 1 ½ periods of the "Four Magnet Focusing Undulator" (4MFU) which has been proposed to be used for the FEL at the TTF. It is based on a regular Halbach type hybrid structure /8/. The gap between the poles is kept fixed at 12mm. The magnets between the poles, which are magnetized parallel and antiparallel to the beam axis are recessed by 2.5mm to create space for the magnets providing the focusing. These magnets are magnetized parallel / antiparallel to the Y-axis as can be seen in Fig. 2. They can be adjusted horizontally. By changing the horizontal separation distance between these magnets in the top and bottom jaw simultaneously the magnitude of the gradient can be changed. A maximum of 25 T/m is possible. Moving all magnets horizontally the horizontal position of the quadrupole axis can be changed accordingly. Increasing / decreasing the separation distance in the top and decreasing / increasing it in the bottom jaw will move the position of the quadrupole axis down or up, respectively.
Using geometrical arguments it can be shown that on the quadrupole axis the field generated by the symmetric undulator part is not influenced by the antisymmetric array of focusing magnets and its strength. This was also verified with 3-D calculations using the MAFIA code /4,7/. The advantages of this proposal therefore are obvious:

1. It is a completely planar structure, which allows for very good access to the field region at the beam position. This is very important for high accuracy field measurements. Also the vacuum chamber can easily be installed without breaking any magnetic circuits.
2. The gradient can be as large as 25 T/m. The exact value and the position of the quadrupole axis is fine tunable.

3. Undulator and focusing fields are decoupled. This means that on the quadrupole axis the sign and magnitude of the field gradient has no influence on the undulator field and vice versa.

For these reasons the 4MFU principle was chosen as the basis of the undulator setup for the TTF.

FODO Lattice

In order to keep the electron beam size small over the whole undulator length a FODO lattice has to be superimposed to the undulator field. A FODO lattice is made up by a sequence of focusing and defocusing quadrupoles separated by focusing free sections. The β - function varies between a maximum and minimum value found in the center of the focusing and defocusing quadrupoles, respectively. The quadrupolar field for the FODO lattice is provided by the magnetic attachments as discussed in the context of Fig. 2. Its characteristic parameters are the FODO period length λ_{FODO} (see Fig. 1) and the focal strength of the quadrupoles given by:

$$(1) \qquad \frac{1}{f_{Quad}}[m^{-1}] = \frac{0.29979 * g[T/m] * l_q[m]}{E[GeV]}$$

where g is the field gradient, E is the kinetic energy of the electrons and l_q is the length of the quadrupole. In the thin lens approximation for small phase advance the variation of the β - function can be estimated to be :

$$(2) \qquad \beta_{Max,Min} = 2 * f \pm \frac{\lambda_{FODO}}{2}$$

This means that in this approximation the average β - function is determined by the focal strength and its beat by the separation of focusing and defocusing quads only. A β - beat which is too large might have a negative effect on the FEL process. On the other hand the FODO period has to be chosen large enough so that the focusing free section between to quads is large enough to span over the separation space between two modules. as is shown schematically in Fig 1. Only then a smoothly running FODO lattice which runs over all undulator modules is possible. In a number of simulations using the TDA3D code /9,10/ the FODO parameters which fit best to the TTF requirements were determined. They are reproduced in Table 2. As can be seen one focusing section extend over five undulator periods which equals to 136.5mm. The gradient is conservatively taken to be 18.3 T/m which is well within the magnetic design values and gives a quiescent safety margin. Other parameters related with the FODO lattice as well as the minimum and maximum β functions found in the FODO quads can be found in Table 2 as well. They were calculated using an exact tracking

code rather than making the approximations used in eq (2). Due to the large phase advance for the Phase 1 only parameter trends can be seen qualitatively using eq. (2). In the case of phase 2 the results agree better than 15% .
The natural weak focusing of an undulator is given by:

$$\frac{1}{f_{Und}}[m^{-1}] = \frac{0.4494 * L[m] * B^2_{Max}[T]}{E^2[GeV]} \quad (3)$$

Here L denotes the undulator length and B_{Max} the undulator peak field . The values for Phase 1 and Phase 2 are reproduced in table 2. The contribution of the whole undulator in both case is considerably smaller than the focal strength of one individual FODO quad. This effect was included in the tracking calculations. It leads to a small variation of the β function along the undulator of a few percent and can be neglected for the consideration of the FODO parameters..

Undulator Prototype

A first 220mm long prototype of a 4MFU type undulator structure has been assembled. This structure can be seen in Fig 3. The structure consists of 16 poles and the corresponding magnets. The exact vertical position of the poles can be fine tuned via tuning screws. With this means the "naked " undulator without focusing magnets can be fine tuned. The focusing magnets are mounted in groups of four. Two sets separated by five nonfocusing half periods are visible in Fig. 3. Two horizontal adjustment screws are seen per focusing attachment. These attachments are fixed and can be moved independently of the magnetic array producing the undulator field. Their strength can be changed by either changing the separation distance or by the total number of magnets which are mounted per FODO quad. In this way a great flexibility is obtained.
The aim of this prototype was to check its mechanic feasibility and to try assembling techniques, find assembling tools etc. The quality of the magnets was not sufficient for good magnetic tests. It is planned to build a 0.8m long prototype which will be available until the end of 1996 to test the magnetic performance of the 4MFU in detail

.

References

[1] A. M. Kondratenko, E. L. Saldin, Part. Accel. 10 (1980), 207
[2] R. Bonifacio, C. Pellegrini, L. Narducci, Opt. Comm. 50 (1984), 373
[3] "A VUV Free Electron Laser at the TESLA Test Facility at DESY, Conceptual Design Report" DESY, Hamburg, April 1995
[4] Y. M. Nikitina, J. Pflüger, Nucl. Instr. and Methods A375 (1996),325
[5] J. Pflüger, Y. M. Nikitina, TESLA - FEL 96-02, 1996
[6] Y. M. Nikitina, J. Pflüger, TESLA - FEL 96-03, 1996
[7] J. Pflüger, Y. M. Nikitina, in press in Nucl. Instr. and Methods
[8] K. Halbach, Journal de Physique, C1, suppl.2 , (1983) C1-211
[9] T. M. Tran, J. S. Wurtele, Comp. Phys. Comm. 54 (1980), 263
[10] P. Jha, J. S. Wurtele, Nucl. Instr. and Methods A331 (1993), 477

Figure Captions

Fig 1 General layout of the undulator section for the Phase 1 setup showing schematically the subdivision into modules, drift spaces and the relation to the smooth overall FODO lattice (graph in lower part of the figure)

Fig 2 3-D perspective view of 1 ½ periods of the proposed 4MFU structure for the undulator for the TTF. For details see text.

Fig 3 220mm long prototype of the 4MFU showing the focusing sections separated by five nonfocusing half periods.

Table 1 : Parameters for Phase 1 and 2 of the TTF

		Phase 1	**Phase 2**
Energy	[GeV]	0.3	1.0
normalized Emittance	[mm mrad]	2	2
Energy spread	[%]	0.17	0.1
Bunch length	[μm]	250	50
Peak current	[A]	500	2500
Radiative wavelength	[mm]	72	6.4
Saturation length	[m]	14	25
Saturation Power	[GW]	0.2	3.0

Table 2: Undulator and FODO Parameters for Phase 1 and 2

Gap	[mm]	12
Period Length	[mm]	27.3
Undulator Peak Field	[T]	0.5
K - Parameter		1.27
Max. Gradient	[T/m]	25
Number of poles per module		327
Total length per module	[mm]	4492.2
Required field Gradient	[T/m]	18.3
Length of FODO quad	[mm]	136.5
FODO Period Length	[m]	0.9555
Number of FODO periods per module		5
Separation between Modules	[m]	0.2853

		Phase 1	**Phase 2**
Number of modules		3	6
Total length	[m]	14.33	28.67
Focal strength of FODO quads	[m^{-1}]	2.50	0.75
Natural Undulator Focal strength	[m^{-1}]	1.873	0.674
Phase advance per FODO cell	[Deg]	52	18
β_{Max} in Undulator	[m]	1.5	3.5
β_{Min} in Undulator	[m]	0.5	2.5
Ave. Beamsize in Undulator	[μm]	55	55

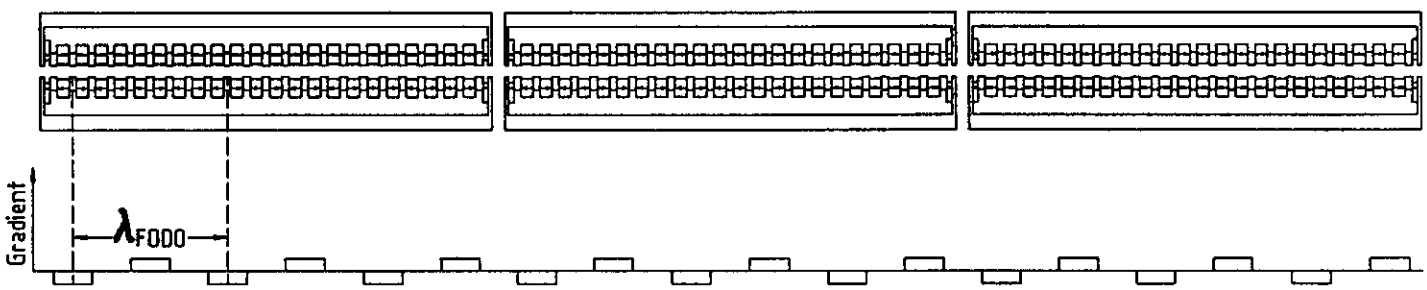

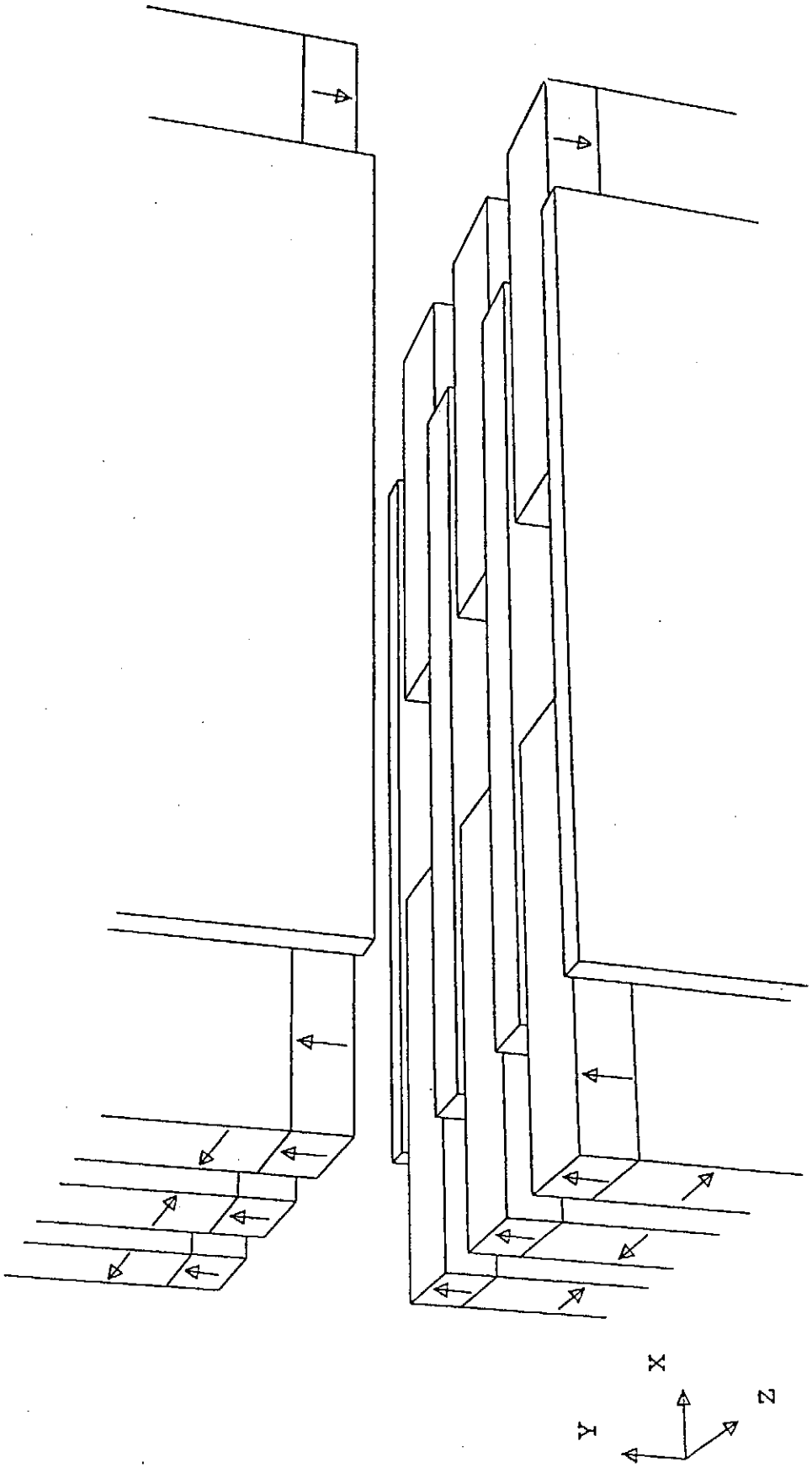
X
Z
Y

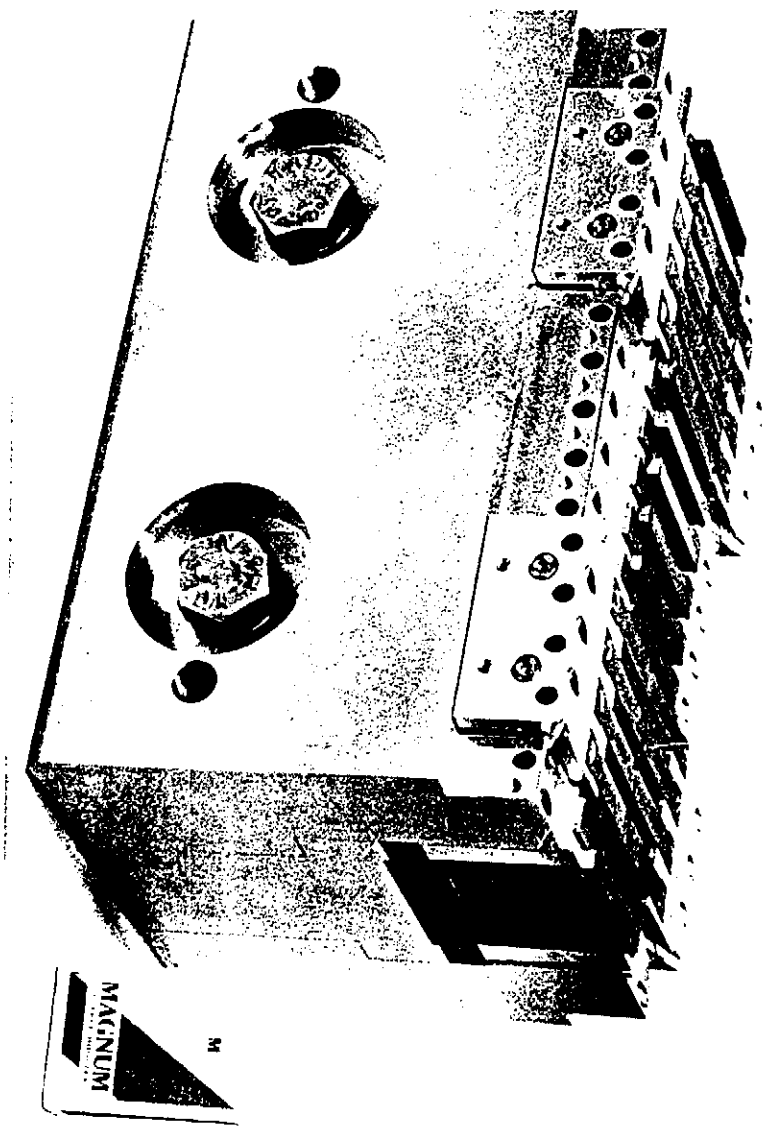
MAGNUM

Fundamental Limitations of an X-ray FEL Operation Due to Quantum Fluctuations of Undulator Radiation

J. Rossbach[a], E.L. Saldin[b], E.A. Schneidmiller[b], M.V. Yurkov[c*]

[a]*DESY, 22607 Hamburg, Germany*

[b]*Automatic Systems Corporation, 443050 Samara, Russia*

[c]*Joint Institute for Nuclear Research, Dubna, 141980 Moscow Region, Russia*

Abstract

In this paper we show that the effect of energy diffusion in the electron beam due to quantum fluctuations of undulator radiation imposes fundamental limit towards achieving very short wavelength in The FEL amplifier.

1. Introduction

R&D works on linear colliders give a promise to obtain in the nearest future high-energy, low emittance and monochromatic electron beams which could be used for a wide range of applications. One of the possible applications of these beams is to use them as driving beams for a SASE FEL (self amplified spontaneous emission free electron laser) operating in the VUV and X-ray wavelength band [1, 2, 3]. There are also trends to develop the projects of SASE FEL operating at shorter wavelength. In connection with this tendency a reasonable question should be formulated whether there are limitations on the way to very short wavelengths.

At present, numerical simulation codes or codes based on fitting formulae are used for optimization of the FEL parameters [1, 2, 4, 5, 6]. Nevertheless, one should use the results obtained with these codes very carefully in new region of parameters (high energy of electrons, short length of the electron bunch, etc) since there could be novel physical effects which have not been taken into account in these physical models and codes. In this paper we show that there exists fundamental effect of quantum fluctuations of undulator radiation which imposes a limit towards very short wavelength [7]. For instance, this effect should play significant role in one of the LCLS scenario [8].

2. Basic equations

We consider an FEL amplifier with helical undulator and axisymmetric electron beam[1]. H_w and λ_w are the amplitude of the magnetic field and the period of the undulator, respectively. The angle of the electron rotation in the undulator is equal to $\theta_s = K/\gamma$, where $\gamma = \mathcal{E}_0/m_e c^2$ is the relativistic factor of the electron with nominal energy $\mathcal{E}_0$, $K = eH_w\lambda_w/2\pi m_e c^2$ is the undulator parameter, $(-e)$ and m_e are the charge and the mass of the electron, respectively, and c is the velocity of light (we use CGS units in this paper).

We assume the transverse phase space distribution of the particles in the beam to be Gaussian and the beam is matched to the magnetic focusing system of the undulator. The rms beam size and rms angle spread of the electrons in the beam are given by the expressions: $\sigma_r = \sqrt{\epsilon_n\beta/\gamma}$ and $\sigma_\theta = \sqrt{\epsilon_n/\beta\gamma}$, where β is the beta function and ϵ_n is the rms normalized emittance. We assume the energy spread to be Gaussian: $dw = d\mathcal{E}\exp(-\mathcal{E}^2/2\sigma_E^2)/\sqrt{2\pi\sigma_E^2}$.

It was shown in refs. [7, 9, 10] that existent projects of SASE FEL have peculiar feature that diffraction expansion of radiation is small at one field gain length, so one-dimensional approximation could be used for quick estimation of the FEL parameters. In the one-dimensional approximation operation of the FEL amplifier can be described in terms of the gain parameter Γ and the following dimensionless parameters: the space charge parameter $\hat{\Lambda}_p^2$, the parameter of the longitudinal velocity spread $\hat{\Lambda}_T^2$ and the efficiency parameter ρ [11, 12]:

$$\Gamma = \left[\frac{I}{I_A}\frac{2\pi K^2}{\gamma^3\lambda_w\sigma_r^2}\right]^{1/3},$$

$$\hat{\Lambda}_p^2 = \Lambda_p^2/\Gamma^2 = \frac{1+K^2}{K^2}\left[\frac{I}{I_A}\frac{2K^2\lambda_w^2}{\pi^2\gamma^3\sigma_r^2}\right]^{1/3},$$

* Corresponding author. Tel. +7 09621 62154, fax +7 09621 65767, e-mail yurkov@sunse.jinr.dubna.su.

[1] The case of a planar undulator is considered in ref. [7]

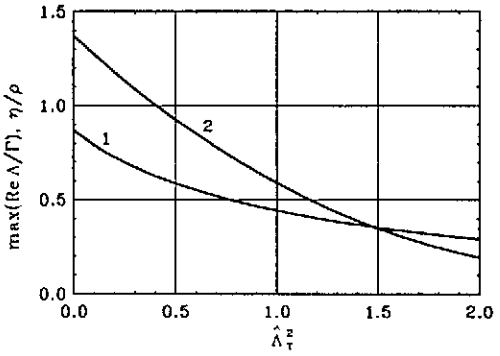

Fig. 1: Normalized field gain Λ/Γ and FEL efficiency at saturation η/ρ versus the parameter of the longitudinal velocity spread $\hat{\Lambda}_T^2$. Here $\hat{\Lambda}_p^2 = 0$ and detuning corresponds to the maximum field gain at each value of $\hat{\Lambda}_T^2$.

$$\hat{\Lambda}_T^2 = \Lambda_T^2/\Gamma^2 = (\sigma_E^2/\mathcal{E}_0^2 + \gamma_z^4\sigma_\theta^4/4)/\rho^2 \quad ,$$
$$\rho = \Gamma\lambda_w/4\pi \; . \tag{1}$$

Here $\lambda = 2\pi c/\omega$ is the radiation wavelength, I is the beam current, $I_A = mc^3/e \simeq 17$ kA is Alfven's current and $\gamma_z^2 = \gamma^2/(1+K^2)$.

The analysis of parameters of proposed VUV and X-ray SASE FELs shows that the region of parameters of these devices is at negligibly small influence of the space charge, $\hat{\Lambda}_p^2 \ll 1$. It means, that the main characteristics of the SASE FEL, field gain and the efficiency at saturation are universal function of the only longitudinal velocity spread parameter Λ_T^2.

The main problem to be solved at a design stage of an experiment is to find a safety margin for the FEL parameters which provide efficient operation. Fig. 1 shows the dependencies of the maximal field gain and the efficiency at saturation on the longitudinal velocity spread parameter. Let us define the safety margin of the FEL amplifier operation by the condition that the relative loss in the field gain due to spread of longitudinal velocities should be less than 10 per cent of the value at $\hat{\Lambda}_T^2 = 0$. This corresponds to the following restriction on the parameter of the longitudinal velocity spread (see Fig. 1)[2]:

$$\hat{\Lambda}_T^2 = \frac{1}{\rho^2}\frac{\sigma_E^2}{\mathcal{E}_0^2} + \frac{1}{4\Gamma^2\beta^2}\left(\frac{2\pi\epsilon}{\lambda}\right)^2 \lesssim 0.1 \; . \tag{2}$$

Analyzing condition (2), we can rewrite it in the following form:

$$\lambda^{4/3} \gtrsim \alpha_1\beta^{2/3} + \alpha_2\beta^{-4/3} \quad , \tag{3}$$

[2] Some authors (see, e.g. refs. [9, 10]) write the conditions for the FEL amplifier operation as:
1) $\Delta\mathcal{E}/\mathcal{E} \lesssim \rho$, 2) $\epsilon \lesssim \lambda/2$.
We see that the first condition corresponds to the first term in eq. (2), but the second condition could considerably overestimate the requirements on the value of the emittance as it is seen from eq. (2).

where we have shown explicitly the parametric dependency on the radiation wavelength λ and on the focusing beta function β. It follows from this condition and definition of the reduced parameters (1) that at the focusing beta function

$$\beta_{cr} = \frac{\epsilon\gamma^2}{\sqrt{2}}\frac{\mathcal{E}_0}{\sigma_E}\frac{1}{1+K^2} \quad , \tag{4}$$

we achieve operation of the FEL amplifier at the shortest possible (critical) wavelength which still lies within the safety margin of operation:

$$\lambda_{cr} \simeq 18\pi\epsilon\frac{\sigma_E}{\mathcal{E}_0}\left[\frac{\gamma I_A}{I}\frac{1+K^2}{K^2}\right]^{1/2} \quad . \tag{5}$$

The critical undulator period is defined by the value of the critical wavelength (5) and the resonance condition: $\lambda_w^{cr} = 2\gamma^2\lambda_{cr}/(1+K^2)$.

3. Quantum fluctuation effects

Particle moving in the field of the undulator emits also incoherent radiation [13]. The mean energy loss of each electron into incoherent radiation is given by:

$$d\mathcal{E}_0/dz = 2r_e^2\gamma^2 H_w^2(z)/3 \quad , \tag{6}$$

where $r_e = e^2/mc_e^2$. This contribution obviously increases with energy. If the energy loss of the electron $\Delta\mathcal{E}_{SR}$ is about

$$\frac{\Delta\mathcal{E}_{SR}}{\mathcal{E}_0} \sim \rho \quad , \tag{7}$$

this effect begins to influence the operation of the FEL amplifier. In principle, this does not lead to a fatal limitation of the maximal electron energy, because the energy losses of the electron can be compensated by an appropriate tapering of the magnetic field of the undulator, thus keeping the resonance condition. It limits though the possibility to tune the photon wavelength by tuning the electron energy to the tuning range

$$\frac{|\Delta\lambda|}{\lambda} \lesssim \frac{\eta}{\Delta\mathcal{E}_{SR}/\mathcal{E}_0} \quad . \tag{8}$$

Also, one might expect considerable experimental difficulties (e.g. heat load on mirrors and monochromators, signal-to-noise ratio, etc), if the totally radiated power is some orders of magnitude larger than the desired FEL power.

A more fundamental limit is imposed by the growth of the uncorrelated energy spread in the electron beam due to the quantum fluctuations of synchrotron radiation. The rate of energy diffusion is given by the expression[3]:

$$< d(\delta\mathcal{E})_{qf}^2/dz >= 55e\hbar\gamma^4 r_e^2 H_w^3/24\sqrt{3}m_e c \quad . \tag{9}$$

[3] Rigorous calculations of energy diffusion show that this formula provide an accuracy about several per cent in the whole region for $K > 1$ [14]

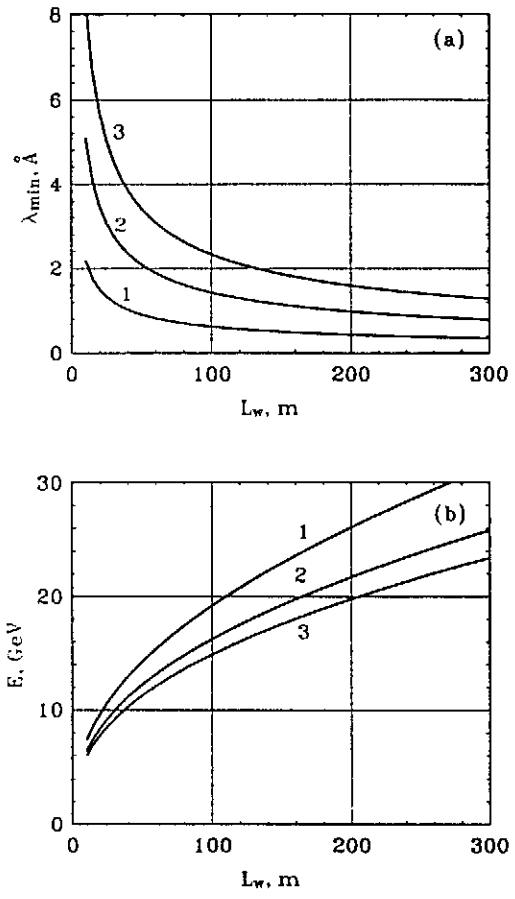

Fig. 2: Minimal achievable photon wavelength in an FEL amplifier and corresponding energy of the electron beam versus the length of the undulator L_w. The curves 1, 2 and 3 correspond to values of the normalized emittance 10^{-4} cm rad, 2×10^{-4} cm rad and 3×10^{-4} cm rad, respectively. The energy spread at the entrance of the undulator in all cases is equal to $\sigma_{E0} = 1$ MeV.

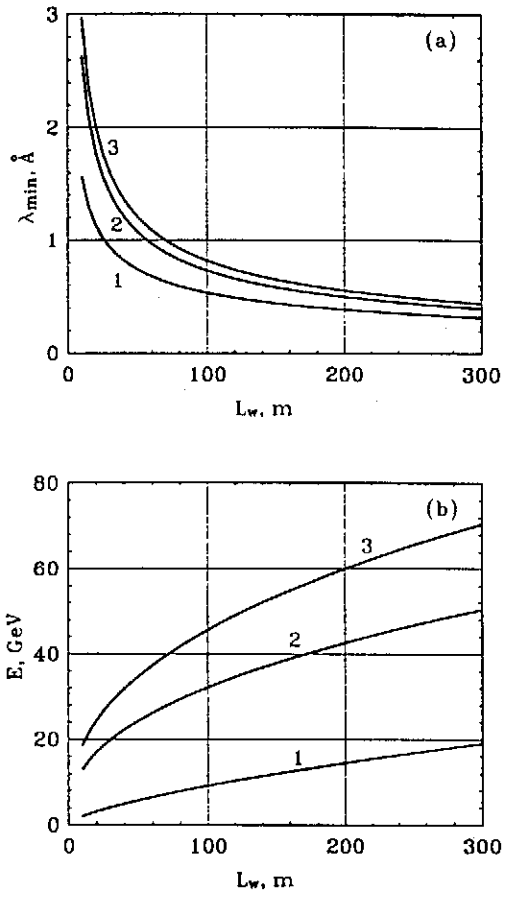

Fig. 3: Minimal achievable photon wavelength in an FEL amplifier and corresponding energy of the electron beam versus the length of the undulator L_w. The curves 1, 2 and 3 correspond to values of the energy spread at the entrance of the undulator of 0 MeV, 3 MeV and 6 MeV, respectively. The normalized emittance is 10^{-4} cm rad in all cases.

This effect is growing drastically with energy and imposes a principle limit on achieving very short wavelengths. Indeed, to achieve a shorter wavelength at specific parameters of the electron beam (i.e. at specific values of the peak current, the normalized emittance and the energy spread), the energy should be increased (see eq. (5). On the other hand, the gain length is increased drastically with increasing the energy which forces to increase the value of the undulator parameter (hence, to increase the undulator field). As a result, at some value of the energy, the energy spread caused by quantum fluctuations will stop the FEL amplifier operation.

To obtain a notion about this limit, let us consider the following model situation. First, consider three parameter sets of the electron beam: $\epsilon_n = 10^{-4}$ cm rad, $\epsilon_n = 2 \times 10^{-4}$ cm rad and $\epsilon_n = 3 \times 10^{-4}$ cm rad. The peak current for all of the examples is equal to $I = 5$ kA and the initial energy spread is equal to $\sigma_{E0} = 1$ MeV. Imagine that one has a possibility to construct an undulator of length L_w. It is reasonable to formulate the problem as follows. At which energy of the electron beam and at which parameters of the undulator the minimal wavelength could be achieved and what is the value of that wavelength.

Fig.2 presents the plots of the minimal achievable wavelength and the corresponding energy of the electron beam versus the undulator length. When performing calculations we assumed that to obtain saturation of a SASE FEL, the undulator length L_w should be about 20 power gain lengths L_g [6]. The operating wavelength has been obtained using expression (5) with the energy spread given by summing up mean squared values of the initial energy spread σ_{E0} and the energy spread due to the fluctuations of synchrotron radiation (9) at the undulator exit, $\sigma_E = (\sigma_{E0}^2 + \sigma_{qf}^2)^{1/2}$. The value of optimal beta function has been calculated in accordance with eq. (4). It is seen from these plots that there is no significant decrease of the minimal wavelength for undulator lengths exceeding $L_w \sim 100$ m.

Fig.3 presents plots of the minimal achievable wavelength and the corresponding energy of the electron beam versus

Table 1: FEL amplifier for the shortest wavelength

	#1	#2	#3
Electron beam			
Energy $\mathcal{E}_0$, GeV	19.2	22.8	26
Peak current I, kA	5	5	5
RMS normalized emittance ϵ_n, cm rad	10^{-4}	2×10^{-4}	3×10^{-4}
RMS energy spread σ_E, MeV	1	2	3
External focusing beta function β, m	54	36	27
Undulator*			
Period λ_w, cm	3.65	5.42	6.93
Magnetic field H_w, T	0.57	0.64	0.69
Undulator parameter K	1.96	3.27	4.46
Undulator length L_w, m	100	100	100
Radiation			
Wavelength λ, Å	0.62	1.59	2.76
Power gain length L_g, m	5	5	5
Efficiency η, %	0.023	0.035	0.045

* Helical tapered undulator.

the undulator length. Here we fix the value of the normalized emittance and change the initial energy spread in the beam σ_E from zero value up to 6 MeV. It is seen that after $L_w \gtrsim 100$ m all the wavelength curves approach asymptotically the curve describing the case of zero value of the initial energy spread. This indicates that quantum fluctuations of synchrotron radiation impose a limit on the value of the minimal achievable wavelength in an X-ray FEL. The value of this limit can be estimated analytically. Let us consider an electron beam with a very small energy spread. We see from (see eq. (5)) that the critical wavelength is then determined by the induced energy spread due to quantum fluctuations. In the same way as it was done above, we assume that the undulator length L_w should be about 20 power gain lengths L_g. Using eqs. (5) and (9) one can obtain that at fixed values of the undulator length L_w, beam current I and normalized emittance ϵ_n, the absolute minimum of the wavelength is achieved at the undulator parameter $K = 1$. The minimal wavelength and the energy at which this minimum is achieved are given by the following expressions [7]:

$$\lambda_{min} \simeq 45\pi \left[\lambda\!\!\!^{-}_c r_e\right]^{1/5} L_w^{-7/15} \left[\epsilon_n^2 \frac{I_A}{I}\right]^{8/15} ,$$

$$\gamma \simeq 0.13 \left[\frac{L_w}{\epsilon_n}\right]^{2/3} \left[\frac{I}{I_A}\right]^{1/3} , \qquad (10)$$

where $\lambda\!\!\!^{-}_c = \hbar/mc$. It should be noted that these formulae give only an estimation of the limit, because they have been obtained using expression (9) for the rate of the energy diffusion which is valid only for $K \gg 1$.

To obtain a feeling about optimized parameters of the FEL amplifier for operation at the shortest possible wavelength, we present in Table 1 three parameter sets.

4. Conclusion

In conclusion we should summarize the following. In principle, quantum fluctuations impose a limit to achieving short wavelengths. The only real possibility to decrease the minimal wavelength is to decrease the value of the normalized emittance. At the present level of accelerator technology it could be possible to construct electron accelerators with a peak current of few kA, a normalized emittance of about 10^{-4} cm rad and an uncorrelated energy spread in the beam about one MeV. At these electron beam parameters the minimal achievable wavelength in an X-ray FEL will be in the range of 0.5 – 1 Å.

5. Acknowledgments

We thank B.H. Wiik, D. Trines and I. Ivanov for their interest and support in our work.

6. REFERENCES

[1] R. Tatchyn et al., Nucl. Instrum. and Methods A375(1996)274.

[2] "A VUV Free Electron Laser at the TESLA Test Facility at DESY. Conceptual Design Report", DESY, TESLA-FEL 95-03, Hamburg, June, 1995.

[3] J. Rossbach, Nucl. Instrum. and Methods A375(1996)269.

[4] K.J. Kim and M. Xie, Nucl. Instrum. and Methods A331(1993)359.

[5] W. Brefeld et al., Nucl. Instrum. and Methods A375(1996)295.

[6] E.L. Saldin, E.A. Schneidmiller and M.V. Yurkov, DESY Print May 1995, TESLA-FEL 95-02, Hamburg, DESY, 1995.

[7] J. Rossbach, E.L. Saldin, E.A. Schneidmiller and M.V. Yurkov, Nucl. Instrum. and Methods A374(1996)401.

[8] R. Tatchyn et al., AIP Conference Proceedings 322(1994)320.

[9] C. Pellegrini, Nucl. Instrum. and Methods A272(1988)364.

[10] K.-J. Kim, Nucl. Instrum. and Methods A358(1995)31.

[11] R. Bonifacio, C. Pellegrini and L. Narducci, Opt. Commun. 50(1984)373.

[12] E.L. Saldin, E.A. Schneidmiller and M.V. Yurkov, Sov. J. Part. Nucl. 23(1992)104.

[13] Ya.S. Derbenev, A.M. Kondratenko and E.L. Saldin, Nucl. Instrum. and Methods 193(1982)415

[14] E.L. Saldin, E.A. Schneidmiller and M.V. Yurkov, DESY Print March 1996, TESLA-FEL 96-05, Hamburg, DESY, 1996. Nucl. Instrum. and Methods A, in press.

Calculation of the Green's Function for an Axisymmetric Diaphragm Focusing Line

E.L. Saldin[a], E.A. Schneidmiller[a], M.V. Yurkov[b]
[a] *Automatic Systems Corporation, 443050 Samara, Russia*
[b] *Joint Institute for Nuclear Research, Dubna, 141980 Moscow Region, Russia*

Abstract
A novel type of an FEL amplifier with diaphragm focusing line (periodically spaced absorbing screens with holes) has perspective to be used for application where high average and peak radiation power is required. In this paper we present the derivation of the Green's function for diaphragm focusing line. The approach to obtain the Green's function is based on the using of impedance boundary conditions proposed by L.A. Veinstein [1]. This algorithm of electromagnetic field calculations can be implemented in linear and nonlinear codes for simulation of the FEL amplifier with diaphragm focusing line.

1. Introduction

It was shown in [2, 3, 4] that the laser driver for commercial inertial confinement fusion reactor could be constructed on the base of FEL amplifier technique. It becomes possible sue to the use of a multistage FEL amplifier. Such an FEL amplifier configuration provides a possibility to obtain peak power of radiation to be much more than the peak power of the electron beam. Nevertheless, in a large number of stages, when the radiation power is of the order or greater than the peak power of electron beam, diffraction expansion of radiation significantly decreases the rate of the energy extraction off the electron beam. In other words, there is no possibility to use conventional FEL amplifier scheme in which radiation is confined due to "optical guiding" effect [5]. To overcome this problem, we have proposed to use the scheme of the FEL amplifier with diaphragm focusing line. A diaphragm focusing line has a form of periodically spaced screens with round holes and is inserted inside the undulator. It provides external focusing of radiation due to the diffraction effects and confines the radiation in the vicinity of the electron beam.

Diaphragm focusing line operates as follows. Consider electromagnetic wave passing inside the sequence of diaphragm. When the electromagnetic wave diffracts at the first diaphragm, it produces diffraction pattern in the plane of the next diaphragm. When the second diaphragm is placed in the main maximum of the diffraction pattern, diffraction losses are minimal. Further, sideband maxima of the diffraction pattern produced by the second diaphragm are less than that of the first pattern, etc. When the wave passes a large number of diaphragms, the field eigenmode is formed which has low diffraction losses.

The first investigation of the diffraction effects influence on the forming of the field in the diaphragm line was carried out by Fox and Lee using Huygens' principle [6]. A more rigorous approach based on Maxwell's equations was developed by Veinstein [1]. Here we use Veinstein method. When the radiation wavelength is much less than the size of the diaphragm line, the impedance boundary conditions can be imposed equivalent in effect to the diaphragm edges action. Thus, the problem of the open waveguide excitation is reduced to that of the closed one. Impedance boundary conditions do not depend on the polarization of the radiation field.

In our previous paper we reported on the development of analytical techniques to solve the eigenvalue problem of the FEL amplifier with axisymmetric electron beam and diaphragm focusing line [7]. In this paper we present the derivation of the Green's function for axisymmetric diaphragm focusing line. The obtained expressions can be implemented in linear and nonlinear codes for simulation of the FEL amplifier with diaphragm focusing line.

2. Formulation of the problem

We consider the electron beam moving along the z axis inside the axisymmetric diaphragm line in the

magnetic field of the helical undulator:

$$H_x + iH_y = H_w \exp(-i\kappa_w z) ,$$

where H_w and $\lambda_w = 2/\pi/\kappa_w$ are the amplitude of the magnetic field and the period of the undulator, respectively. The angle of the electron rotation in the undulator is equal to $\theta_s = K/\gamma$, where $\gamma = \mathcal{E}_0/m_e c^2$ is the relativistic factor of the electron with nominal energy $\mathcal{E}_0$. $K = eH_w\lambda_w/2\pi m_e c^2$ is the undulator parameter, $(-e)$ and m_e are the charge and the mass of the electron, respectively, and c is the velocity of light (we use CGS units in this paper). The electron rotation angle is considered to be small and longitudinal electron velocity v_z is close to the velocity of light ($v_z \simeq c$).

The diaphragm line is formed by a sequence of absorbing screens with holes. Period of the diaphragm line is equal to L and radius of the holes is equal to R. The diaphragm line is azimuthally symmetric relative to the undulator axis which coincides with the z axis of the polar coordinates (r, φ, z). We assume the Fresnel number $N_F = R^2/\lambda L$ (where λ is the wavelength of the amplified electromagnetic wave) to be large, ($N_F \gg 1$). The electric field of amplified electromagnetic wave is presented in the complex form:

$$E_x + iE_y = \tilde{E}(x, y, z) \exp[i\omega(z/c - t)],$$

where $\omega = 2\pi c/\lambda$. We let for simplicity the electromagnetic wave to be circularly polarized. Such an assumption does not restrict the generality of consideration, because the polarization degeneracy takes place in the system under study.

The electromagnetic field in a diaphragm line is subjected to the wave equation

$$c^2\nabla^2\vec{E} - \partial^2\vec{E}/\partial t^2 = c^2\vec{\nabla}(\vec{\nabla} \circ \vec{E}) + 4\pi\partial\vec{j}/\partial t, \qquad (1)$$

which can be obtained from Maxwell's equations. The vector $\vec{j}$ denotes the electron beam current density. If the transverse dimensions of the diaphragms and the electron beam are rather large, the field in the diaphragm line is approximately transverse and we can neglect the term $\vec{\nabla}(\vec{\nabla} \circ \vec{E})$ in the right part of eq. (1). Longitudinal component of beam current density j_z is a periodical function and may be expanded in a Fourier series:

$$j_z = \sum_{m=1}^{\infty} \tilde{j}_m(x, y, z) \exp(im\psi) + C.C.,$$

where phase $\psi = \kappa_w z + \omega(z/c - t)$. Taking into account that the transverse current density has the form

$$j_x + ij_y = \theta_w \exp(-i\kappa_w z) j_z,$$

we find that $\tilde{E}$ satisfies the equation (we keep here only "resonant" terms after averaging over the undulator period):

$$\nabla_\perp^2\tilde{E} + 2i(\omega/c)\partial\tilde{E}/\partial z = -4\pi i\theta_w(\omega/c^2)\tilde{j}_1. \qquad (2)$$

The typical scale of the amplitude $\tilde{E}$ change is assumed to be much more than the wavelength, thus the second derivative of $\tilde{E}$ with respect to z is omitted in eq. (2).

We represent the first harmonic of the electron beam current density $\tilde{j}_1$ and amplitude of radiation field $\tilde{E}$ as a Fourier series in the angle φ:

$$\tilde{j}_1(z, r, \varphi) = \sum_{n=-\infty}^{n=+\infty} \tilde{j}_1^{(n)}(z, r) \exp(-in\varphi),$$

$$\tilde{E}(z, r, \varphi) = \sum_{n=-\infty}^{n=+\infty} \tilde{E}^{(n)}(z, r) \exp(-in\varphi)$$

The Fourier components $\tilde{E}^{(n)}$ are calculated with the integration of the following partial differential equation:

$$\left[\frac{\partial^2}{\partial r^2} + \frac{1}{r}\frac{\partial}{\partial r} + \frac{2i\omega}{c}\frac{\partial}{\partial z} - \frac{n^2}{r^2}\right]\tilde{E}^{(n)} = -\frac{4\pi i}{c^2}\theta_w\omega\tilde{j}_1^{(n)}. \qquad (3)$$

To solve this equation we should impose boundary conditions for the radiation field at the edges of the diaphragm line. In this paper we, following the method of Veinstein [1], use the impedance boundary conditions:

$$\left[\tilde{E}^{(n)} + (1+i)\beta_0\sqrt{cL/4\omega}\partial\tilde{E}^{(n)}/\partial r\right]|_{r=R} = 0.$$

where $\beta_0 = \zeta(1/2)\sqrt{\pi} \simeq 0.824$ and $\zeta(...)$ is the Riemann's zeta function. Thus, the problem of the open waveguide excitation is reduced to conventional one of the closed waveguide excitation.

3. Calculation of Green function

The Laplace transforms of the Fourier components $\tilde{E}^{(n)}$

$$\bar{E}^{(n)}(p, r) = \int_0^{\infty} \exp(-pz)\tilde{E}^{(n)}(z, r)dz$$

are submitted to the following ordinary differential equation

$$\left[\frac{d^2}{dr^2} + \frac{1}{r}\frac{d}{dr} + q^2 - \frac{n^2}{r^2}\right]\bar{E}^{(n)} = \bar{f}^{(n)}, \qquad (4)$$

where notations are introduced:

$$q^2 = 2ip\omega/c,$$

$$\tilde{f}^{(n)} = 2i\omega\tilde{E}_{ext}(r) - (4\pi i\theta_w\omega/c^2)\tilde{j}_1^{(n)}(p,r),$$

$$\tilde{j}_1^{(n)}(p,r) = \int_0^\infty \exp(-pz)j_1^{(n)}(z,r)dz.$$

To solve the inhomogeneous differential equation (4) we use the Green's functions method. We seek the solution of eq. (4) in the form:

$$\tilde{E}(p,r) = \int_0^R \tilde{f}^{(n)}(p,r')\tilde{G}^{(n)}(r,r',p)r'dr' ,$$

where function $\tilde{G}^{(n)}(r,r',p)$ is the Laplace transform of the Green's function $\tilde{G}^{(n)}(r,r',z)$ which has to be found. The function $\tilde{G}^{(n)}$ is the solution of the homogeneous equation

$$\left[\frac{\partial^2}{\partial r^2} + \frac{1}{r}\frac{\partial}{\partial r} + q^2 - \frac{n^2}{r^2}\right]\tilde{G}^{(n)}(r,r',p) = 0 , \qquad (5)$$

which satisfies the conditions

$$\left[\tilde{G}^{(n)} + (1+i)\beta_0\sqrt{cL/4\omega}\partial\tilde{G}^{(n)}/\partial r\right]|_{r=R} = 0,$$
$$\tilde{G}^{(n)}|_{r=r'+0} = \tilde{G}^{(n)}|_{r=r'-0},$$
$$\partial\tilde{G}^{(n)}/\partial r|_{r=r'+0} - \partial\tilde{G}^{(n)}/\partial r|_{r=r'-0} = 1/r'. \qquad (6)$$

We seek the solution of eq. (5) in the form:
Region 1 ($0 < r < r'$):

$$\tilde{G}^{(n)}(r,r',p) = A_1 J_n(qr), \qquad (7a)$$

Region 2 ($r' < r < R$):

$$\tilde{G}^{(n)}(r,r',p) = A_2 J_n(qr) + A_3 N_n(qr), \qquad (7b)$$

where J_n and N_n are the Bessel function and Neumann function of the order n. The conditions (6) give us the following equations:

$$A_2 J_n(\xi) + A_3 N_n(\xi) = 0$$
$$A_1 J_n(qr') = A_2 J_n(qr') + A_3 N_n(qr')$$
$$A_2 J_n'(qr') + A_3 N_n'(qr') - A_1 J_n'(qr') = 1/qr', \qquad (8)$$

where $\xi = qR(1+\Delta)$ and $\Delta = (1+i)\beta_0\sqrt{cL/4\omega R^2}$. The solution of this system is given by

$$A_1 = (\pi/2)N_n(qr') - (\pi/2)J_n(qr')N_n(\xi)/J_n(\xi)$$
$$A_2 = -(\pi/2)J_n(qr')N_n(\xi)/J_n(\xi)$$
$$A_3 = (\pi/2)J_n(qr'). \qquad (9)$$

To find the coefficients A_j we used the relation for the Bessel functions:

$$N_n(X)J_n'(X) - J_n(X)N_n'(X) = -2/\pi X.$$

Substituting expressions (9) into expressions (7) we obtain:
Region 1 ($0 < r < r'$):

$$\tilde{G}^{(n)}(r,r',p) = (\pi/2)\left[J_n(\xi)N_n(qr') - N_n(\xi)J_n(qr')\right]J_n(qr)/J_n(\xi), \qquad (10a)$$

Region 2 ($r' < r < R$):

$$\tilde{G}^{(n)}(r,r',p) = (\pi/2)\left[J_n(\xi)N_n(qr) - N_n(\xi)J_n(qr)\right]J_n(qr')/J_n(\xi). \qquad (10b)$$

Fourier components $\tilde{E}^{(n)}(z,r)$ are obtained by means of the inverse Laplace transformation of $\tilde{E}^{(n)}(p,r)$:

$$\tilde{E}^{(n)}(z,r) = \frac{1}{2\pi i}\int_{\gamma'-i\infty}^{\gamma'+i\infty} dp\tilde{E}^{(n)}(p,r)\exp(pz). \qquad (11)$$

The path of integration in the complex plane p is parallel to the imaginary axis. The constant γ' is a positive number which is larger than all real parts of the integrand singularities. Using Borel's theorem

$$\int_0^\infty dz\exp(-pz)\int_0^z f(x)\Phi(z-x)dx = \tilde{f}(p)\tilde{\Phi}(p), \qquad (12)$$

where

$$\tilde{f}(p) = \int_0^\infty dz\exp(-pz)f(z)\,,\tilde{\Phi}(p) = \int_0^\infty dz\exp(-pz)\Phi(z), \qquad (13)$$

we get

$$\tilde{E}^{(n)}(z,r) = \frac{2i\omega}{c}\int_0^R \tilde{E}_{ext}^{(n)}(r)G^{(n)}(r,r',z)r'dr' -$$
$$\frac{4\pi i}{c^2}\theta_w\omega\int_0^R dr'r'\times$$
$$\int_0^z dz'\tilde{j}_1^{(n)}(z',r')G^{(n)}(r,r',z-z'). \qquad (14)$$

The Green's function $G^{(n)}(r,r',z)$ is also obtained by means of the inverse Laplace transformation:

$$G^{(n)}(r,r',z)=\frac{1}{2\pi i}\int\limits_{\gamma'-i\infty}^{\gamma'+i\infty}dp\bar{G}^{(n)}(r,r',p)\exp(pz). \quad (15)$$

The integral (15) is usually calculated along the closed loop with application of the theory of residues. Consider the closed loop consisting of the straight line $(\gamma'-i\infty,\gamma'+i\infty)$ and a half-circumference of infinite radius in the left-hand half-plane. It can be shown that function $\bar{G}^{(n)}$ is a single-valued function of a complex variable p and satisfies the condition of the Jordan lemma. In accordance with Cauchy's theorem, the integral along the straight line $(\gamma'-i\infty,\gamma'+i\infty)$ can be represented as the sum of the residues with respect to the poles inside the loop. Finally, the solution for the Green function $G^{(n)}$ is written in the form:

$$G^{(n)}(r,r',z)=-\frac{\pi}{2}\sum_j\exp(\lambda_j z)\times \frac{J_n(q_j r)J_n(q_j r')N_n(\xi_j)}{dJ_n(\xi)/dp|_{p=\lambda_j}}, \quad (16)$$

where λ_j is the j th root of the equation

$$J_n(\xi)=J_n\left(qR(1+\Delta)\right)=0. \quad (17)$$

Using approximation of a large value of Fresnel number, $R^2/\lambda L$, we find from eq. (17):

$$\lambda_j=-ic\nu_{nj}^2(1-2\Delta)/2\omega R^2,$$

where ν_{nj} is the j th root of the Bessel function of the n th order. The final expression for the Green's function has the form

$$G^{(n)}(r,r',z-z')=-\frac{ic(1-2\Delta)}{\omega R^2}\times \sum_j\exp\left(-ic\nu_{nj}^2(1-2\Delta)(z-z')/2\omega R^2\right)J_{n+1}^{-2}(\nu_{nj})\times J_n\left(\nu_{nj}(1-\Delta)r/R\right)J_n\left(\nu_{nj}(1-\Delta)r'/R\right). \quad (18)$$

To find $G^{(n)}$ we have used the following relations:

$$dJ_n(\xi)/dp|_{p=\lambda_j}=\left(dJ_n(\xi)/d\xi|_{\xi=\nu_{nj}}\right)i\omega R^2(1+2\Delta)/c\nu_{nj}$$

$$N_n(\nu_{nj})=-2\left(\pi\nu_{nj}dJ_n(\xi)/d\xi|_{\xi=\nu_{nj}}\right)^{-1},$$

$$dJ_n(\xi)/d\xi|_{\xi=\nu_{nj}}=-J_{n+1}(\nu_{nj}).$$

4. Example for application of Green function

Let us demonstrate the application of the Green's function for solution of the initial-value problem for the FEL amplifier with axisymmetric electron beam and diaphragm focusing line. In the linear approximation, in the case of negligibly small space charge field, the evolution of the complex amplitude $\tilde{j}_1^{(n)}(z,r)$ of the first harmonic of the beam current density is given by the equation [8]:

$$\frac{d^2\tilde{j}_1^{(n)}}{dz^2}+2iC\frac{d\tilde{j}_1^{(n)}}{dz}-C^2\tilde{j}_1^{(n)}=\frac{e\omega\theta_w}{2ic\gamma_z^2\mathcal{E}_0}j_0(r)\bar{E}^{(n)}(z,r), \quad (19)$$

where $\mathcal{E}_0$ is the nominal energy of the electrons, $C=k_w-\omega/2\gamma_z^2c$ is the detuning of the particle with nominal energy $\mathcal{E}_0$ from resonance with wave, $\gamma_z^{-2}=\gamma^{-2}+\theta_w^2$, $\gamma=\mathcal{E}_0/mc^2$, $\theta_w=eH_w/\mathcal{E}_0k_w$, $-j_0(r)\simeq-ecn_0(r)$ is the longitudinal component of the beam current density at the undulator entrance, $n_0(r)$ is the beam density. Substitution (14), (18) into (19), we obtain the single integro-differential equation for the first harmonic of the beam current density $\tilde{j}_1^{(n)}$ which can be solved numerically using computer code.

5. References

[1] L.A. Veinstein, Open resonators and waveguides (Sovetskoe Radio, Moscow, 1966).

[2] E. L. Saldin et al., Nucl. Instrum. and Methods, **361**(1995)317

[3] E.L. Saldin, E.A. Schneidmiller, M.V. Yurkov, Nucl. Instrum. and Methods, **375**(1996)389.

[4] E.L. Saldin, E.A. Schneidmiller, M.V. Yurkov, Preprint JINR E9-96-68, Dubna, 1996.

[5] G.T. Moore, Opt. Commun. **52**(1984)46.

[6] A.G. Fox and T. Li, Bell Syst. Tech. J. **40**(1961)453.

[7] E.L. Saldin, E.A. Schneidmiller, Yu.N. Ulyanov and M.V. Yurkov, Nucl. Instrum. and Methods, **375**(1996)385.

[8] E.L. Saldin, E.A. Schneidmiller, M.V. Yurkov, Phys. Rep., **260**(1995)187.

Universal formulae for calculation of energy diffusion in an electron beam due to quantum fluctuations of undulator radiation

E.L. Saldin[a], E.A. Schneidmiller[a], M.V. Yurkov[b]
[a] *Automatic Systems Corporation, 443050 Samara, Russia*
[b] *Joint Institute for Nuclear Research, Dubna, 141980 Moscow Region, Russia*

Abstract
The paper presents calculations of the rate of energy diffusion in the electron beam due to quantum fluctuations of undulator radiation. The cases of a helical and a planar undulator are considered. Universal fitting formulae are obtained valid for an arbitrary value of the undulator parameter.

1. Introduction

When relativistic electron beam passes through the undulator, it emits radiation. This process leads to the decrease of the mean energy of electrons and to the increase of energy spread in the beam due to quantum fluctuations of undulator radiation. This effect should be carefully taken into account when designing systems equipped with undulators. For instance, the effect of energy diffusion imposes a fundamental limit on a minimal achievable wavelength in an X-ray free electron laser [1].

For the first time coefficient of energy diffusion due to quantum fluctuations of synchrotron radiation has been calculated in ref. [2]. This expression is also valid for calculation of energy diffusion in the undulator at large values of the undulator parameter. At small values of undulator parameter the coefficient of energy diffusion could be simply derived using approximation of Thompson scattering of equivalent photons on electrons [3, 4]. In practice, the parameters of devices are frequently lying in an intermediate region and in this paper we consider the case of arbitrary value of the undulator parameter. Using the results of numerical calculations, we have obtained universal fitting formulae for a helical and a planar undulator providing a high accuracy.

2. Helical undulator

We consider ultrarelativistic electron beam propagating in an undulator. The mean energy loss of the electron is given by (in CGS units):

$$d\mathcal{E}/dt = -2r_e^2 c\gamma^2 H^2/3 \quad ,$$

where $r_e = e^2/mc^2$ is classical radius of the electron, $\mathcal{E}$ is the energy of the electron, $\gamma = \mathcal{E}/mc^2$ is relativistic factor and $-e$ and m are the charge and the mass of the electron, respectively. Magnetic field $\vec{H}(z) = (H_x, H_y, H_z)$ at the helical undulator axis has the following form:

$$\vec{H}(z) = (H_w \cos(\kappa_w z), -H_w \sin(\kappa_w z), 0) \ .$$

where H_w is the amplitude of the magnetic field, $\kappa_w = 2\pi/\lambda_w$ and λ_w is the undulator period.

The rate of energy diffusion is given by the expression:

$$\frac{d<(\delta\mathcal{E})^2>}{dt} = \int d\omega \hbar\omega \frac{dI}{d\omega} \ . \qquad (1)$$

The spectral intensity of an undulator radiation $dI/d\omega$ was calculated in ref. [5].

The expression for the rate of energy diffusion can be written in the following form (we assumed that number of the undulator periods is large, so the spectrum broadening due to the finite number of periods is neglected):

$$\frac{d<(\delta\gamma)^2>}{dt} = \frac{14}{15} c\lambda\!\!\!^{-}_c r_e \gamma^4 \kappa_w^3 K^2 F(K) \ , \qquad (2)$$

where $\lambda\!\!\!^{-}_c = \hbar/mc$, $K = eH_w/k_w mc^2$. It is important to notice that the energy diffusion is expressed

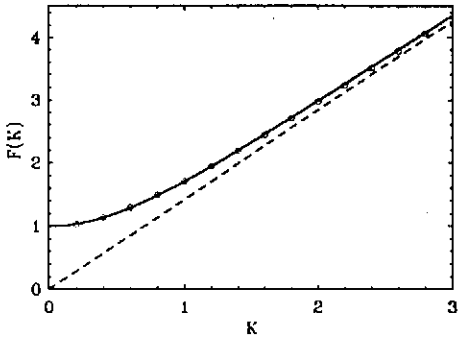

Fig. 1: Function $F(K)$ for helical undulator. Solid curve is calculated with formula (3), the circles are calculations with fitting formula (5) and dotted curve is calculated with asymptotic formula (4) for large values of K.

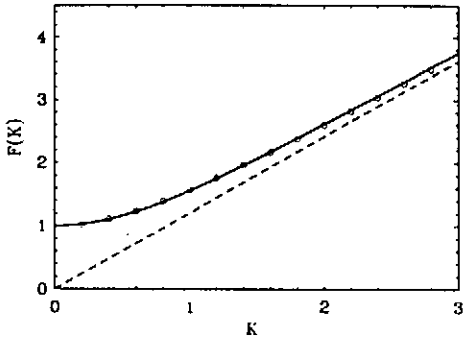

Fig. 2: Function $F(K)$ for planar undulator. Solid curve is calculated with formula (7), the circles are calculations with fitting formula (9) and dotted curve is calculated with asymptotic formula (8) for large values of K.

in terms of dimensionless function $F(K)$ of the only undulator parameter K . Function $F(K)$ is defined as

$$F(K)=\frac{60}{7}\frac{1}{(1+K^2)^3}\sum_{n=1}^{\infty}n^3\times \int_0^1 dyy^2\left[J_n'^2(x)+\left(\frac{n^2}{x^2}-\frac{1+K^2}{K^2}\right)J_n^2(x)\right] \quad (3)$$

where J_n and J_n' are the Bessel function and its derivative, respectively and

$$x=\frac{2K}{\sqrt{1+K^2}}n\sqrt{y(1-y)}\ .$$

The plot of this function is presented in Fig.1. For the cases of small and large values of the undulator parameter K, there exist well known asymptotes [2, 3, 4]:

$$F(K)=\begin{cases}1 & \text{at } K\ll 1\\ \frac{275}{112\sqrt{3}}K\simeq 1.42K & \text{at } K\gg 1\ .\end{cases} \quad (4)$$

In the general case there is no possibility to obtain analytical expression and we write the following fitting formula:

$$F(K)=1.42K+\frac{1}{1+1.50K+0.95K^2}. \quad (5)$$

This formula provides an accuracy better than 1 % in the whole range of parameter K (see Fig.1).

3. Planar undulator

Magnetic field at the planar undulator axis has the following form:

$$\vec{H}(z)=(H_w\cos(\kappa_w z),0,0)\ .$$

In this case expression for the rate of energy diffusion is given by the expression:

$$\frac{d<(\delta\gamma)^2>}{dt}=\frac{7}{15}c\lambda_c r_e\gamma^4\kappa_w^3K^2F(K)\ . \quad (6)$$

Universal function $F(K)$ has the form: [1]:

$$F(K)=\frac{120}{7}\frac{1}{K^2(1+K^2/2)^2}\sum_1^{\infty}n^3\int_0^1 dyyG_n \quad (7)$$

where

$$G_n=\frac{1}{2\pi}\int_0^{2\pi}g_n d\phi,\quad g_n=\frac{(S_1+2S_2/n)^2}{4(1-y)cos^2\phi}-yS_1^2-\frac{2}{n}S_1S_2,$$

$$S_1=\sum_{p=-\infty}^{\infty}J_p(z)J_{n+2p}(x),\quad S_2=\sum_{p=-\infty}^{\infty}pJ_p(z)J_{n+2p}(x),$$

$$x=\frac{2K}{\sqrt{1+K^2/2}}n\sqrt{y(1-y)}cos\phi,\quad z=\frac{K^2}{4(1+K^2/2)}ny\ .$$

For the cases of small and large values of the undulator parameter K, we have:

$$F(K)=\begin{cases}1 & \text{at } K\ll 1\\ \frac{275}{42\pi\sqrt{3}}K\simeq 1.20K & \text{at } K\gg 1\ .\end{cases} \quad (8)$$

[1] There is misprint in the corresponding expression (14) for $dI/d\omega$ in ref. [5]. There should be minus sign inside the square brackets in the expression for function $f(\varphi)$.

In the general case function $F(K)$ is fitted with the following formula:

$$F(K) = 1.20K + \frac{1}{1 + 1.33K + 0.40K^2}\ , \qquad (9)$$

providing an accuracy better than 1 % in the whole range of parameter K (see Fig.2).

4. Acknowledgement

We are extremely grateful to J. Rossbach for many stimulating discussions and support in our work.

5. References

[1] J. Rossbach, E.L. Saldin, E.A. Schneidmiller and M.V. Yurkov, Nucl. Instrum. and Methods A374(1996)401

[2] M. Sands, Phys. Rev. 97(1955)470.

[3] Ya.S. Derbenev, A.M. Kondratenko and E.L. Saldin, Nucl. Instrum. and Methods 193(1982)415.

[4] S. Benson and M.J. Madey, Nucl. Instrum. and Methods, A237(1985)55.

[5] D.F. Alferov, Yu.A. Bashmakov, and E.G. Bessonov, Sov. Phys. Tech. Phys. 18(1974)1336.

A Concept of Free Electron Laser System with 4 MJ Flash Energy for the Laser Fusion Reactor Driver

E.L. Saldin[a], E.A. Schneidmiller[a], Yu.N. Ulyanov[a], M.V. Yurkov[b]

[a] *Automatic Systems Corporation, 443050 Samara, Russia*

[b] *Joint Institute for Nuclear Research, Dubna, 141980 Moscow Region, Russia*

Abstract

This paper presents the further development of a concept of a FEL based driver for commercial inertial confinement fusion reactor [1]-[3]. We have shown technical feasibility of constructing a laser system with the following parameters: laser light wavelength 0.5 μm, flash energy 4 MJ, repetition rate 10 pps and net efficiency 10 %. It becomes possible due to the use of a novel scheme of optical power summation.

1. Introduction

It was shown in refs. [1]-[3] that the laser driver for commercial ICF reactor could be constructed on the base of free electron laser (FEL) technique. In this paper we present a novel scheme of a multi-stage FEL amplifier for ICF energy driver which allows to achieve a higher energy of radiation flash (up to 4 MJ) and ultimate contrast of the laser radiation. It is important that this scheme allows to reduce significantly the requirement on the value of the average current of the driving accelerator with respect to the scheme considered in ref. [1].

An important feature of the proposed driver is that four optical pulses are amplified simultaneously in each FEL amplifier channel. As a result, the number of FEL amplifier channels is reduced by a factor of four. On the other hand, such a solution forces to design a more complicated output optical system. Nevertheless, self-consistent economical analysis, performed in ref. [4], has shown that it results in the reduction of the total cost of the driver by a factor of two with respect to the design presented in refs. [1, 2].

2. Summation of optical power

The main elements of the scheme are the beam transport line with kicker-magnets, matching arcs and multi-stage FEL amplifier (see Fig.1). A train of N electron bunches (N is equal to the number of the FEL amplifier stages) is fed to the entrance of the beam transport line. The bunch separation in the train is equal to $2L_s$, where L_s is the length of one

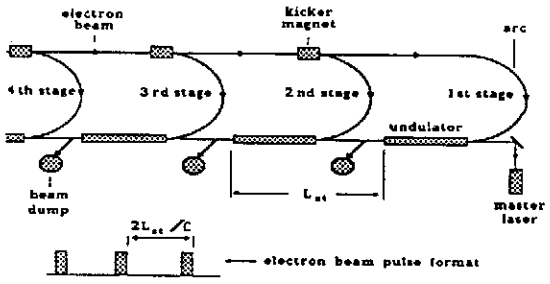

Fig. 1: The scheme of optical power summation.

stage of the FEL amplifier. The first bunch of the train passes the whole beam transport line and is fed to the entrance of the first stage of the FEL amplifier and amplifies an optical bunch from a master laser. At the exit of the undulator the first bunch is directed to the beam dump and the optical pulse is amplified in the second stage of the FEL amplifier by the second electron bunch of the train. The delivering of the second bunch to the second stage of the FEL amplifier is provided by means of switching on the first kicker magnet after passage of the first bunch, etc.

3. Design of the driver

The main parameters and general layout of the driver are presented in Table 1 and Fig.2. Driver consists of three main parts: driving beam generation system, multi-stage, multi-channel FEL amplifier and output

Table 1: General parameters of the laser fusion reactor driver

Radiation wavelength	0.5 μm
Laser pulse length	7 ns
Laser beam brightness	5×10^{20} W/cm^{2}sr
Flash energy	3.5 MJ
Repetition rate	10 pps
Net efficiency	10 %

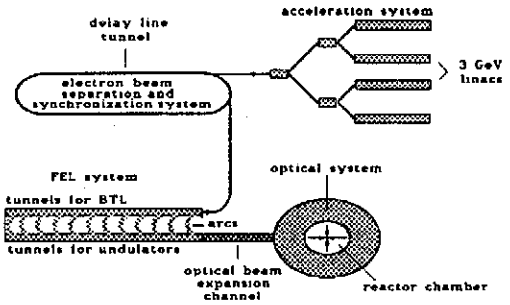

Fig. 2: Layout of the ICF reactor.

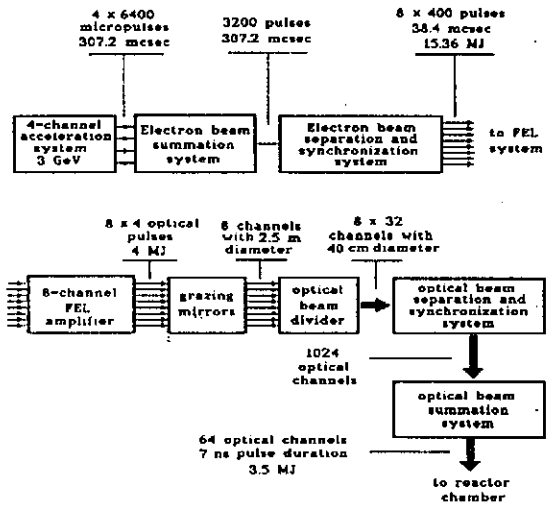

Fig. 3: The scheme of the FEL based energy driver.

optical system.

3.1. *Driving beam generation system*

The driving beam generation system consists of four RF accelerators, a beam summation system and a separation and synchronization system (see Fig. 3) .

The general parameters of RF accelerators are presented in Table 2. The accelerators have module structure (see Fig. 4). Time diagram of the accelerator operation is presented in Fig.5.

Table 2: General parameters of accelerator

Electron energy	3 GeV
RF frequency	500 MHz
Accelerating gradient	5 MV/m
Macropulse duration	308 μs
Repetition rate	10 pps
Shunt impedance	5 MΩ/m
Stored RF energy	23 J/m
Q-factor of unloaded structure	2.5×10^4
Wall RF power losses	3.1 MW/m

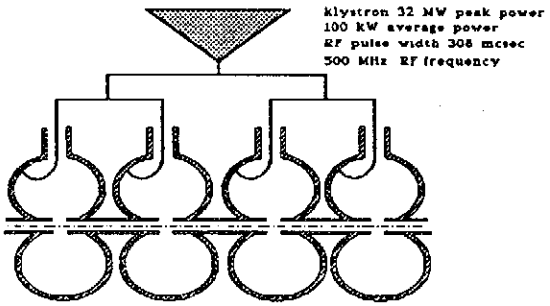

Fig. 4: Module of the RF linear accelerator.

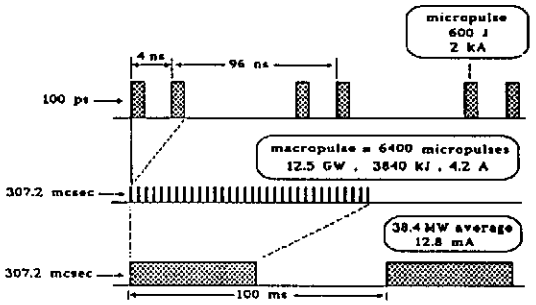

Fig. 5: Electron beam pulse format in the RF accelerator.

To obtain a high value of the average beam current, we use the beam summation system which combines the beams with average over macropulse current of 4.2 A produced by each of four RF linear accelerators into one beam with average over macropulse current of 16.8 A. This is performed in two stages (see Fig.6). At each stage two electron beams with different energies of electrons are combined and then their energies are equalized in a special RF accelerator (see Fig.7).

Separation and synchronization system separates the electron beam of 307.2 μs duration into eight parallel beams of 38.4 μs duration. It has the appearance

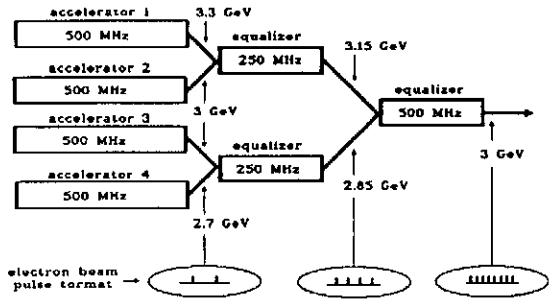

Fig. 6: The scheme of the electron beam summation system.

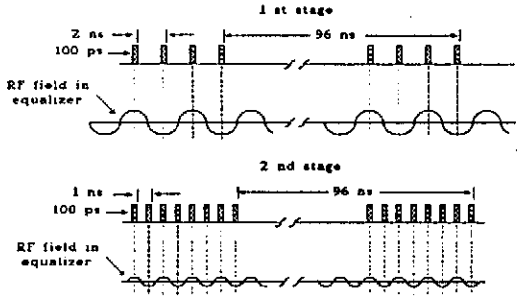

Fig. 7: The scheme of operation of the energy equalizers.

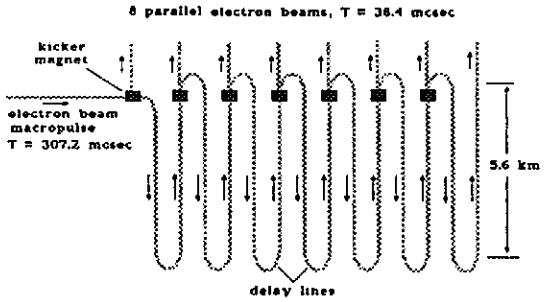

Fig. 8: The scheme of the electron beam separation and synchronization system.

of delay line with the filling time equal to 268.8 μs (see Fig.8). Such a delay line could be placed in two parallel tunnels of 5600 m length connected by arcs with the radius of 50 m. The beam transport line is placed in this tunnel in the same manner as in race-track microtron. After filling the delay line, seven kicker magnets are switched on simultaneously and we obtain eight parallel bunch trains of 38.4 μs pulse duration.

3.2. *FEL amplifier*

FEL amplifier consists of eight parallel channels and each channel has appearance of multi-stage FEL amplifier with 100 stages of amplification (see Fig.9). The principle of operation of this scheme has been described in section 2. The bunch train at the entrance to the beam transport line of each channel consists of 400 micropulses separated by 96 ns. Each micropulse consists of eight electron bunches separated by 1 ns. The time interval between the switching on of kicker magnets is chosen to be equal to 384 ns. It means that each channel of the FEL amplifier amplifies simultaneously four optical micropulses with the same time structure.

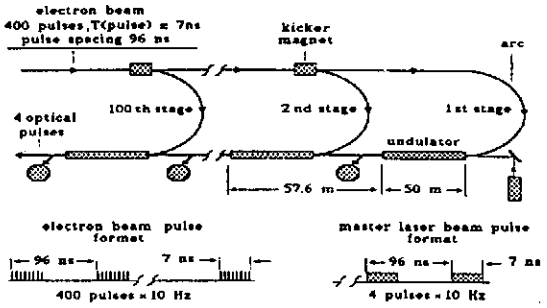

Fig. 9: The scheme of one channel of the FEL amplifier.

Table 3: Parameters of 100 th stage of the FEL amplifier

Electron beam	
Electron energy	3 GeV
Beam current	2 kA
rms energy spread	0.1 %
Normalized emittance	$\pi \times 10^{-3}$ cm rad
Undulator	
Undulator period	15 cm
Undulator field (enter/exit)	15.3 kG / 6.1 kG
Length of the main undulator	48 m
Radiation	
Radiation wavelength	0.5 μm
Efficiency	36 %
Diaphragm line	
Period	10 cm
Radius of the holes	1 cm

The first stage of the FEL amplifier is destined to amplify relatively weak signal from the master laser ($W_{ext} \simeq 1$ MW) by a factor of the order of 10^5. It is designed in a standard manner, i.e. its undulator has a long untapered section and a section with tapered parameters. Subsequent stages of the FEL amplifier amplify a powerful optical beam and provide small amplification per one stage. They operate in a tapered regime from the very beginning and are designed using a scheme of multicomponent undulator (i.e., prebuncher – dispersion section – tapered undulator). The parameters of the prebunchers, dispersion

sections and undulators are optimized for each stage to achieve maximal efficiency. To provide effective focusing of the radiation in these FEL amplifier stages, the diaphragm focusing line is used [1, 5].

Optimization of parameters of the FEL amplifier has been performed in ref. [4]. Total efficiency of the multi-stage FEL amplifier (averaged over all stages) is equal to $\eta_{\rm FEL} \simeq 0.26$. For illustrations we present in Table 3 parameters of the last (100 th) stage of the FEL amplifier.

3.3. *Output optical system*

The function of the output optical system consists in transforming of the input FEL radiation (8 beams of 384 ns pulse duration) into 64 parallel laser beams of 7 ns pulse duration which are directed to the reactor chamber [4]. Its operation proceeds in the three phases: the expansion of radiation, separation and synchronization of the beams and summation of the laser beams. The density and the flux of the radiation energy on the optical elements should be less then 30 J/cm^2 and 3 GW/cm^{2}respectively. So, at the first stage the laser beams are expanded from the size of 2 cm (at the FEL amplifier exit) up to the size of 2.5 m (see Fig.3). Separation and synchronization phase consists of two steps. First, the initial eight laser beams are divided into 256 beams. Second, each of 256 beams are transformed into 1024 parallel beams of 7 ns pulse duration.The necessity in the dividing step is defined by the technical limitations of Pockel's cell which is the main element of optical deflector (see Fig.10). The transmission factor of output optical system is given by the product of the transmission factors of three stages: expansion stage ($T_1 \simeq 0.99$), dividing stage ($T_2 \simeq 0.95$), and separation stage ($T_3 \simeq 0.94$), and equal to $T_{\rm opt} \simeq 0.89$.

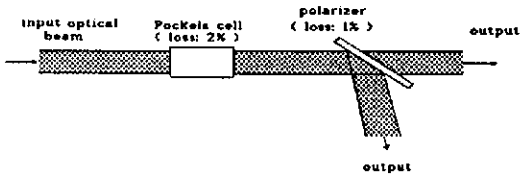

Fig. 10: The scheme of the optical deflector.

3.4. *Efficiency and cost estimation*

The efficiency of the proposed ICF energy driver is defined by the product of the efficiencies of accelerator ($\eta_{\rm ACC} = 0.45$), of the FEL amplifier ($\eta_{\rm FEL} = 0.26$) and of the output optical system ($\eta_{\rm OPT} = 0.89$) and is equal to $\eta_{\rm TOT} \simeq 0.10$.

The total cost of the FEL based fusion driver consists of three main parts: the cost of the accelerator complex (600 M$), the cost of the multi-stage, multi-channel FEL amplifier (700 M$) and the cost of the output optical system (200 M$). So, we estimate the total cost of the FEL driver for ICF reactor to be about 1500 M$ [4].

4. Conclusion

An important feature of the proposed scheme is that it could operate with large spacing of electron bunches. As a result, the requirements on the value of the average current of the driving RF accelerator could be reduced significantly. Another advantage of the proposed scheme is in providing the absolute contrast of the radiation pulse (i.e. there is no any preheating of the target) [4]. This scheme is more preferable with respect to the FEL amplifier design, because the harmful influence of the synchrotron radiation is decreased by two orders of magnitude with respect to the scheme considered in refs. [1, 2]. Also the problem of the beam dump could be solved in a simple way because each bunch passes only one stage of the FEL amplifier.

5. References

[1] E.L. Saldin et al., preprint JINR E9-94-237, Dubna, 1994.

[2] E.L. Saldin et al., Nucl. Instrum. and Methods **A361**(1995)317.

[3] E.L. Saldin et al., Nucl. Instrum. and Methods **A375**(1996)385.

[4] E.L. Saldin et al., preprint JINR E9-96-68, Dubna, 1996.

[5] E.L. Saldin et al., preprint DESY 94-243, DESY, Hamburg, 1994.

Simulation Studies of 6 nm Free Electron Laser at the TESLA Test Facility Starting from Noise

E.L. Saldin[a], E.A. Schneidmiller[a], M.V. Yurkov[b]

[a] *Automatic Systems Corporation, 443050 Samara, Russia*

[b] *Joint Institute for Nuclear Research, Dubna, 141980 Moscow Region, Russia*

Abstract

The paper presents simulation results of Self-Amplified Spontaneous Emission (SASE) FEL at the TESLA Test Facility (TTF) at DESY. One-dimensional, time-dependent program package FEL1D was used for simulations. When simulating linear mode of operation, we have used actual number of electrons in the beam, $N \simeq 6 \times 10^9$, to calculate initial shot noise conditions at the undulator entrance. It was found that there is good agreement between simulation and analytical results. We also performed calculations of autocorrelation functions of the first and the second order, temporal and spectral characteristics of the output radiation of TTF FEL operating in linear and nonlinear SASE modes.

1. Introduction

Self amplified spontaneous emission free electron laser (SASE FEL) is being planned to construct at the TESLA Test Facility at DESY [1]. One of the problems of the SASE FEL design consists in calculation of the output characteristics of such an FEL amplifier starting from noise. Consideration of TTF FEL startup from noise was done previously in ref. [2], where authors have used the modified GINGER code [3]. In this paper we present the simulations of 6 nm option SASE FEL at DESY using one-dimensional, time-dependent codes constructed on the base of program package FEL1D [4].

The linear simulation code is based on the FEL equations written down in linear approximation. This code allows one to perform rigorous simulation of initial conditions. When performing linear simulations of SASE FEL, we have used actual number of electrons in the TTF beam, $N \simeq 6 \times 10^9$, to calculate initial shot noise conditions at the undulator entrance. The results of linear simulations are compared with rigorous results of SASE FEL theory [5, 6]. It was found that there is good agreement between simulation and analytical results.

The nonlinear simulation code is based on macroparticle method. When performing nonlinear simulations we can not use actual number of the particles due to limited capabilities of computer. To overcome this problem, we have used technique proposed in ref. [7] when initial conditions are modelled with small number of macroparticles distributed by special method.

Using linear and nonlinear simulation codes we calculated autocorrelation functions of the first and the second order, temporal and spectral characteristics of the output radiation of TTF FEL. These results could be of use for potential users to define the scope of experiments which could be performed with SASE FEL radiation.

2. Rigorous results of SASE FEL theory

In SASE FEL at DESY the only fundamental TEM_{00} mode is survived which has full transverse coherence. It means, that when considering input shot noise, we should take into account only its fraction having full transverse coherence. The value of this initial modulation could be calculated as follows. Let us consider a monoenergetic electron beam with a current I_0. Then we remember that the electron current is constituted by moving electrons:

$$I(t) = (-e) \sum_k \delta(t - t_k) , \qquad (1)$$

where $\delta(\ )$ is delta-function, (-e) is the charge of the electron and t_k is arrival time of the electron to the undulator entrance. Using this simple physical picture we can calculate the mean squared value of the Fourier harmonic averaged over an ensemble (for $\omega \neq 0$):

$$<| \tilde{I}(\omega) |^2> = < e^2 \sum_k \sum_j e^{i\omega(t_k - t_j)} > = e I_0 T , \qquad (2)$$

where $I_0 T/e$ is the average number of electrons passed through undulator entrance during the time interval T.

In the framework of one-dimensional model and when the effects of space charge field and energy spread in the beam could be neglected, an FEL operation could be described in terms of the gain parameter

Γ and the efficiency parameter ρ (see, e.g. refs. [4]): $\Gamma = [2\pi^2 j_0 K^2 A_{JJ}]^{1/3}[2I_A\lambda_w\gamma^3]^{-1/3}$, $\rho = \lambda_w\Gamma/4\pi$, where λ_w is the undulator period, $K = e\lambda_w H_w/2\pi mc^2$ is the undulator parameter, H_w is the undulator magnetic field, j_0 is the beam current density, $(-e)$ and m are the electron charge and mass, $I_A = mc^3/e \simeq 17kA$, $A_{JJ} = J_0(\nu) - J_1(\nu)$ and $\nu = K^2/(4+2K^2)$.

Solution of the initial-value problem in a high-gain limit for the case when modulated electron beam is fed to the entrance of a planar undulator has the form (see, e.g. [4], Appendix B):

$$\frac{\mid \tilde{E}(\omega,\hat{z}) \mid}{E_0} = \frac{1}{3}\exp\left[\frac{\sqrt{3}}{2}(1-\frac{\hat{C}^2}{9})\hat{z}\right]\frac{\mid \tilde{j}(\omega) \mid}{j_0}, \qquad (3)$$

where $\hat{z} = \Gamma z, \hat{C} = C/\Gamma = (\omega_0 - \omega)/2\rho\omega_0$ is detuning parameter and $\omega_0 = 4\pi c\gamma^2/[\lambda_w(1+K^2/2)]$ is resonant frequency, $\tilde{E}(\omega,z)$ and $\tilde{j}(\omega)$ are, respectively, Fourier components of electric field of the wave $E(t,z)$ and of the beam current density $j(t)$ at the undulator entrance. Normalizing factors E_0 and j_0 are given with the expressions: $E_0 = 8\pi\rho^2\gamma^2 I_A/(\lambda_w cKA_{JJ})$, $j_0 = I_0/S$, where S is the transverse area of the electron beam. We have mentioned above that transversely coherent fraction of the input shot noise is defined by the total beam current, so $\tilde{j}(\omega)/j_0 = \tilde{I}(\omega)/I_0$.

The radiation pulse energy averaged over an ensemble is defined as

$$< W >= \frac{cS}{4\pi^2}\int_0^\infty <\mid \tilde{E}(\omega,z) \mid^2> d\omega. \qquad (4)$$

Substituting eqs. (3) into eq. (4) and taking into account eq. (2), we can calculate the radiation power $\bar{P}_{out} =< W > /T$ averaged over an ensemble and the normalized efficiency [8]:

$$\hat{\eta} = e\bar{P}_{out}/\rho\gamma mc^2 I = \frac{\sqrt{4\pi\rho}}{3\sqrt{\sqrt{3}\hat{z}}N_\lambda}\exp[\sqrt{3}\hat{z}], \qquad (5)$$

where $N_\lambda = 2\pi I/e\omega_0$. We can also write the expression for the spectrum bandwidth (half width at half maximum) of the SASE FEL [9]:

$$\frac{\Delta\omega}{\omega_0}\Big|_{HWHM} = 6\sqrt{\frac{\ln 2}{\sqrt{3}}}\frac{\rho}{\sqrt{\hat{z}}}, \qquad (6)$$

To describe correlation phenomena, the notion of autocorrelation function is introduced. The first order autocorrelation function is defined as:

$$B_1(\tau,z) = \frac{\int_{-\infty}^{\infty} d(\Delta\omega) <\mid \tilde{E}(z,\Delta\omega) \mid^2> \cos[(\Delta\omega)\tau]}{\int_{-\infty}^{\infty} d(\Delta\omega) <\mid \tilde{E}(z,\Delta\omega) \mid^2>},$$

where $\Delta\omega = \omega - \omega_0$. Taking into account expression for spectral density (see eq. (4)) we obtain: $B_1(\tau,z) \propto \exp\left[-9\hat{\tau}^2/\sqrt{3}\hat{z}\right]$, where $\hat{\tau} = \rho\omega_0\tau$. Defining the autocorrelation time $\hat{\tau}_{1/2}$ by the condition of decreasing of the first order autocorrelation function by factor of 2, we get [2]: $\hat{\tau}_{1/2} = \sqrt{\hat{z}\ln(2)/3\sqrt{3}}$.

3. Method for time-dependent simulation

Time-dependent algorithm for simulation of an FEL amplifier should take into account the slippage effect. Electron motion in the undulator is a periodic one, so the radiation of each electron is also periodic function with period $\lambda = 2\pi c/\omega_0$. It seems to be natural to construct the following algorithm [5, 6]. Suppose, we have electron bunch of length l_b. We divide this length into $N_b = l_b/\lambda$ boxes. FEL equations are used in each box for calculation of the motion of the electrons and evolution of the radiation field within one undulator period. The using of steady-state FEL equations averaged over undulator period is justified by the fact that the FEL amplifier is resonance device with a narrow bandwidth. Then we should take into account the slippage effect, i.e. that electromagnetic radiation advances the electron beam by the wavelength λ while electron beam passes one undulator period. It means that radiation which interacted with electrons in the j th box slips to the electrons located in the next, $j+1$ th box. Then procedure of integration is repeated, etc.

This algorithm allows one to calculate the values of the radiation field for each box as a function of the longitudinal coordinate z. Time dependence of the radiation field has the form: $E(z,t) = \tilde{E}(z,t)e^{-i\omega_0(z/c-t)} + C.C.$ at any position along the undulator. Here we explicitly segregated slowly varying complex amplitude $\tilde{E}(z,t)$. Remembering that at any fixed point z of the undulator, time interval between the arrival of radiation connected with to adjacent boxes is equal to $\Delta t = t_{j+1} - t_j = \lambda/c$, we have discrete representation of $\tilde{E}(z,t_j)$.

To calculate spectral characteristics of output radiation, we use Fourier transform. Taking into account that the radiation field $E(z,t)$ is calculated in discrete moments, we obtain ($\Delta\omega = \omega - \omega_0$ and $\omega > 0$):

$$\tilde{E}(z,\omega) = \frac{2\pi}{\omega_0}\sum_j \tilde{E}^{(j)}e^{-2\pi ij\Delta\omega/\omega_0}, \qquad (7)$$

The total radiation energy in the pulse is given by the expression:

$$W = \frac{cS}{4\pi^2}\int_{-\infty}^{\infty}\tilde{E}(z,\Delta\omega)\tilde{E}^*(z,\Delta\omega)\,d(\Delta\omega)\,. \qquad (8)$$

The first and the second order autocorrelation functions, $B_1(\tau)$ and $B_2(\tau)$, are calculated in accordance with the definitions:

$$B_1(\tau,z) = \frac{<\tilde{E}(t,z)\tilde{E}^*(t+\tau,z) + C.C.>}{2<\mid \tilde{E}(t,z) \mid^2>}.$$

$$B_2(\tau,z) = \frac{<\mid \tilde{E}(t,z) \mid^2 \mid \tilde{E}(t+\tau,z) \mid^2>}{\left[<\mid \tilde{E}(t,z) \mid^2>\right]^2}. \qquad (9)$$

Table 1: Parameters of TTF FEL /6 nm option/

Electron beam	
Energy, $\mathcal{E}_0$	1000 MeV
Peak current, I_0	2500 A
rms bunch length, σ_z	5×10^{-3} cm
Normalized rms emittance , ϵ_n	2×10^{-4} cm rad
External β-function,	300 cm
Number of bunches per train	7200
Repetition rate	10 Hz
Undulator	
Type	Planar
Period, λ_w	2.73 cm
Peak magnetic field, H_w	4.97 kGs
Radiation	
Wavelength, λ	6.42 nm
Reduced parameters	
Gain parameter, Γ	9.7×10^{-3} cm^{-1}
Efficiency parameter, ρ	2.1×10^{-3}

where notation "< ... >" indicate average over a time interval T.

4. Results of numerical simulation

General design of 6 nm option of SASE FEL at DESY is presented in ref. [1]. Design parameters of the SASE FEL are presented in Table 1.

The transverse phase space distribution of the particles in the beam is assumed to be gaussian. In the present study we consider two models of axial distribution of the beam current, stepped profile with $I(s) = I_0$ and length $l_b = \sqrt{2\pi}\sigma_z$ and gaussian profile with $I(s) = I_0 \exp(-s^2/2\sigma_z^2)/\sqrt{2\pi}\sigma_z$, where $I(s)$ is the beam current, $s = z - v_z t$, I_0 is the peak beam current (see Table 1). When writing down 1-D FEL equations, we substitute the beam current density by effective value $j(s) = I(s)/(2\pi\sigma_r^2)$ where $\sigma_r = \sqrt{\epsilon_n \beta/\gamma}$, ϵ_n is the normalized emittance, β is the beta function. It means that the actual beam is modelled by the electron beam with constant (along transverse direction) beam current density having transverse area $S = 2\pi\sigma_r^2$.

When performing numerical simulations, we neglect the effects of space charge and longitudinal velocity spread in the beam. We also assume that fluctuations of the beam current density define the value of input shot noise signal. It means that we neglect the effect of the longitudinal velocity fluctuations connected with finite energy spread in the beam. One can show that the ratio of the noise signal due to the fluctuations of the velocity to the shot noise signal is of the order of $\sigma_E^2/\mathcal{E}^2\rho^2$, where σ_E is the energy spread in the beam. This ratio is always less than unity, because the safety margin of FEL amplifier assumes that $\sigma_E^2/\mathcal{E}^2 \ll \rho^2$.

Linear time-dependent simulation algorithm is organized as follows. We divide the electron beam into $N_b = l_b/\lambda$ boxes. Linear steady-state FEL equations are used in each box for calculation of the evolution of the radiation field within one undulator period, i.e. within $\Delta\hat{z} = \lambda_w\Gamma$ (see, e.g. [4]): $d^3\hat{E}^{(j)}/d\hat{z}^3 = i\hat{E}^{(j)}$, where $\hat{E}^{(j)} = \bar{E}/E_0$ is reduced electric field of electromagnetic wave in the j th box.

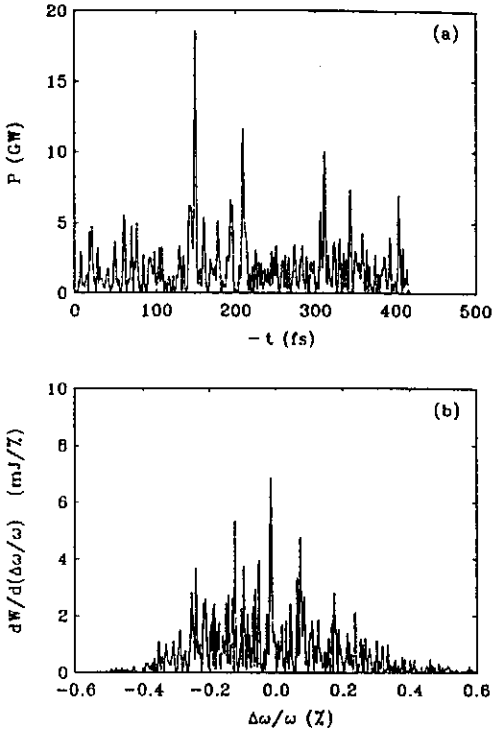

Fig. 1: Temporal structure (a) and spectrum of radiation pulse at $z = 12$ m for stepped axial profile of electron beam. Calculations have been performed with linear simulation code.

If total number of the particles is equal to N, the number of particles per one box is equal to $N_\lambda = N/N_b$. To calculate initial conditions, we distribute N_λ particles randomly in each box. Amplitude and phase of the beam bunching are calculated in accordance with relation:

$$\frac{d\hat{E}^{(j)}}{d\hat{z}}|_{z=0} = \frac{1}{N_\lambda}\sum_{k=1}^{N_\lambda}\exp(-i\psi_k^{(j)}), \quad \frac{d^2\hat{E}^{(j)}}{d\hat{z}^2}|_{z=0} = 0\,,$$

where $\psi_k^{(j)} = 2\pi s_k^{(j)}/\lambda$ is the electron phase and $s_k^{(j)}$ is axial coordinate of the particle in the bunch.

In Figs.1-3 we present the results of numerical simulations of linear regime for stepped axial profile of the electron beam. To calculate initial conditions at the undulator entrance, we have used actual number of electrons in the TTF beam, $N \simeq 6 \times 10^9$.

When simulating SASE FEL with steady-state codes, the notion of "effective" power of input signal P_{in} is usually introduced. The value of P_{in} could be obtained in the following way. First, at fixed undulator length using time-dependent simulation algorithm, we should perform aver-

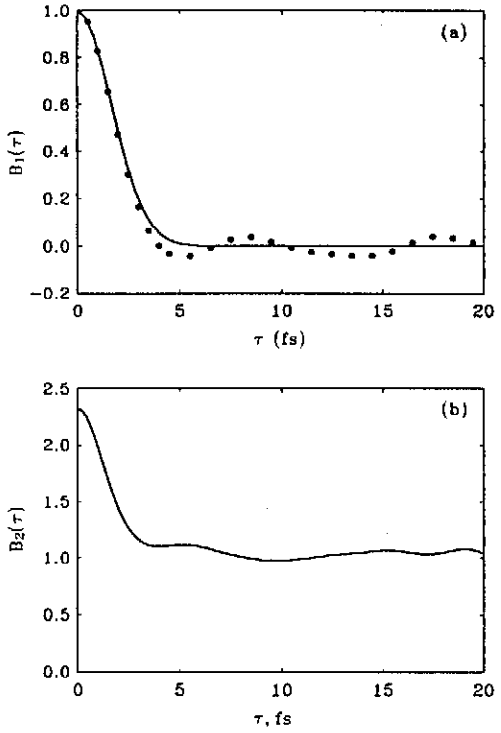

Fig. 2: First order autocorrelation function $B_1(\tau)$ and second order autocorrelation function $B_2(\tau)$ of output radiation pulse at $z = 12$ m for stepped axial profile of electron beam. Circles are the results of calculations with linear simulation code and solid curve is calculated with analytical formula.

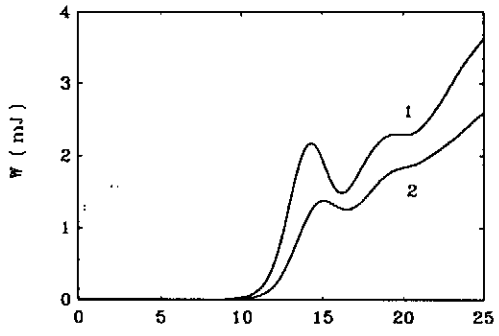

Fig. 3: Dependence of the radiation flash energy on the undulator length for the stepped (curve 1) and Gaussian (curve 2) axial profile of electron beam. Calculations have been performed with nonlinear simulation code.

aging of output power over the total length of the bunch P_{out}. Then, using steady-state expression for $P_{out} = (1/9)P_{in}\exp(\sqrt{3}\hat{z})$ we can obtain the value of P_{in}. Calculations, have been performed at the undulator length of 12 m and provided the value of $P_{in} \simeq 100$ W. It is interesting to compare this value with analytical estimation. Using relation (5), we can obtain estimation for "effective" power of input signal of TTF FEL: $P_{in} \simeq 3\rho^2 P_b/N_\lambda \simeq 100$ W (here we have taken into account that $\hat{z} \simeq 11$ at the length of undulator 12 m).

It follows from the results of numerical simulations that all the important characteristics of radiation are in a good agreement with the analytical asymptotics presented in Section 3. Typical difference of the order of 10 % can be explained by finite number ($\sim 10^2$) of wavepackets (spikes) inside the radiation pulse of TTF FEL. In particular, this effect explain an oscillating behavior around zero value of the tails of autocorrelation functions (see Fig. 2). In the asymptotics of infinitely long electron bunch one will obtain the exact agreement with the analytical results.

Nonlinear time-dependent simulation algorithm is based on similar technique described in the previous part. In the case of nonlinear simulations we can not use actual number of the particles due to limited capabilities of computer. To overcome this problem, we have used technique proposed in ref. [7].

In Fig. 3 we present the results of nonlinear simulations of TTF FEL for stepped and gaussian axial profile of the electron beam. The number of macroparticles in each box was equal to $M = 20$. We can see that the output radiation power continues to grow after saturation point.

5. Acknowledgments

The authors should like to thank R. Bonifacio, J. Rossbach and P. Pierini for many useful discussions and recommendations. We thank G. Materlik and J. Schneider for their interest in our work.

6. REFERENCES

[1] "A VUV Free Electron Laser at the TESLA Test Facility: Conceptual Design Report", DESY Print TESLA-FEL 95-03, Hamburg, DESY, 1995.

[2] P. Pierini and W. Fawley, Nucl. Instrum. and Methods **A375**(1996)332.

[3] R.A. Jong, W.M. Fawley and E.T. Scharlemann, SPIE 1045(1989)18.

[4] E.L. Saldin, E.A. Schneidmiller and M.V. Yurkov, Phys. Rep. **260**(1995)187.

[5] R. Bonifacio et al., Nucl. Instrum. and Methods **A341**(1994)181.

[6] R. Bonifacio et al., Phys. Rev. Lett. **73**(1994)70.

[7] C. Penman and B.W.J. McNeil, Opt. Commun. **90**(1992)82.

[8] K.J. Kim, Phys. Rev. Lett. **57**(1986)1871.

[9] A.M. Kondratenko and E.L. Saldin, Part. Acc. **10**(1980)207.

Analysis of the eigenvalue equation of the FEL amplifier with annular electron beam, helical undulator and circular waveguide

E.L. Saldin[a], E.A. Schneidmiller[a], M.V. Yurkov[b]

[a] *Automatic Systems Corporation, 443050 Samara, Russia*

[b] *Joint Institute for Nuclear Research, Dubna, 141980 Moscow Region, Russia*

Abstract

In this article we present the results of the eigenvalue problem analysis of an FEL amplifier with circular waveguide, helical undulator and annular electron beam. The eigenvalue equation is derived taking into account space charge fields and energy spread of electrons in the beam. Analytical expressions for the eigenfunctions of active waveguide and formulae of their expansion in the eigenfunctions of passive waveguide, are derived, too. Asymptotic behaviour of the obtained solutions is studied in details.

1. Introduction

In a low energy region, it is more effective to generate annular electron beams providing the higher peak current and use them as driving beams for the FELs [1]. So, it is important from the practical point of view to develop the FEL theory for such systems. In this article we present the analysis of the eigenvalue problem for the FEL amplifier with the circular waveguide, helical undulator and annular electron beam. The presented model of the FEL amplifier allows one to perform complete analytical study of the beam radiation modes taking into account space charge fields, energy spread of electrons in the beam and influence of the waveguide walls on the process of amplification.

In particular, we find here that azimuthal symmetry of the electron beam current density modulation does not lead to the azimuthal symmetry of radiation fields and vice versa. Physically it means that azimuthal symmetry is violated by the helicity of the undulator. Indeed, the electron beam moving in the helical magnetic field may be considered as a gyrothrope active medium. In the case of the open beam it results in the circular polarization of radiation field. The presence of the walls of the circular waveguide significantly complicates the situation because boundary conditions on the waveguide walls are different for radial and azimuthal components of the electric field of the amplified wave. As a result, double degeneration of azimuthal modes is eliminated and it leads to the mentioned above difference between the azimuthal dependencies of the electron beam density modulation and radiation field.

2. General equations

We consider the electron beam moving along the z axis in the field of a helical undulator $H_x + iH_y = H_w \exp\{-i\kappa_w z\}$, where $\kappa_w = 2\pi/\lambda_w$ is the undulator wavenumber. We neglect the transverse variation of the undulator magnetic field and assume that the electrons move along the constrained helical trajectories parallel to the z axis. The electron rotation angle $\theta_s = eH_w/\kappa_w\mathcal{E}$, where $\mathcal{E}$ is the energy of the electron, is considered to be small and the longitudinal electron velocity v_z is close to the velocity of light c ($v_z \simeq c$). We assume also that the radius of a helical trajectory of the electron in the undulator is much less than transverse size of the electron beam.

We consider paraxial approximation when writing down the equations for electromagnetic field. This approximation assumes that the characteristic scale of the field amplitude change along the z axis is much more than the radiation wavelength and the field is nearly to be transversely polarized. Under this approximation the electric field $\vec{E}$ of the electromagnetic wave could be written in the form:

$$\vec{E}(z,\vec{r}_\perp,t)=\left[\vec{e}_x\hat{E}_x(z,\vec{r}_\perp)+\vec{e}_y\hat{E}_y(z,\vec{r}_\perp)\right]\times \exp\left[i\omega(z/c-t)\right]+C.C. \qquad (1)$$

where $\vec{e}_x$ and $\vec{e}_y$ are the unit vectors directed along the x axis and y axis, respectively, and ω is the frequency

of the amplified wave. Here we explicitly segregated the strong dependence of E on the z coordinate.

We consider conventional initial conditions when electromagnetic wave with frequency ω and nonmodulated electron beam are fed to the undulator entrance. Under these conditions the evolution of the electromagnetic field amplitude $\tilde{E}$ in the FEL amplifier is subjected to the system of integro-differential equations [2]:

$$\nabla_\perp^2 \begin{pmatrix} \tilde{E}_x \\ \tilde{E}_y \end{pmatrix} + \frac{2i\omega}{c}\frac{\partial}{\partial z}\begin{pmatrix} \tilde{E}_x \\ \tilde{E}_y \end{pmatrix} = \int_0^z dz' \left\{ \begin{pmatrix} i \\ 1 \end{pmatrix} \frac{\pi\omega\theta_s^2 e}{c^2} j_0(\vec{r}_\perp)\left(\tilde{E}_x + i\tilde{E}_y\right) + \frac{4\pi i e}{\omega} j_0(\vec{r}_\perp)\left[\nabla_\perp^2 \begin{pmatrix} \tilde{E}_x \\ \tilde{E}_y \end{pmatrix} + \frac{2i\omega}{c}\frac{\partial}{\partial z'}\begin{pmatrix} \tilde{E}_x \\ \tilde{E}_y \end{pmatrix}\right]\right\} \times \int_{-\infty}^{\infty} d\xi \left(\frac{dF(\xi)}{d\xi}\right) \exp\left\{ i\left[\frac{\omega}{c\gamma_z^2\mathcal{E}_0}\xi + C\right](z'-z)\right\}. \quad (2)$$

where $-j_0(\vec{r}_\perp) \simeq -ecn_0(\vec{r}_\perp)$ is the longitudinal component of the beam current density at the undulator entrance at $z = 0$, $P = \mathcal{E} - \mathcal{E}_0$, $C = \left[\kappa_w - \omega/(2c\gamma_z^2)\right]$ is the detuning of the particle with nominal energy $\mathcal{E} = \mathcal{E}_0$, $\gamma_z^{-2} = \gamma_0^{-2} + \theta_s^2$, $\gamma_0 = \mathcal{E}_0/m_e c^2$ and $-e$ and m_e are the electron charge and mass, respectively. The $F(P)$ is function describing the initial energy distribution and is normalized to the unity. When deriving eqs. (2), the space charge effect have been taking into account using approximation that transverse electron beam size r_0 is rather large, $r_0^2/\gamma_z^2 \gg c^2/\omega^2$ (in particular it means that the plasma frequency reduction in the waveguide can be neglected).

To solve these equations, we should impose the conditions of continuity of the field and its derivative at the beam boundary and boundary conditions on the waveguide walls. In the case of circular waveguide, in paraxial approximation boundary conditions have the form [2]:

$$\tilde{E}_\varphi\,|_{r=R} = 0, \qquad \partial(r\tilde{E}_r)/\partial r\,|_{r=R} = 0, \quad (3)$$

where R is the waveguide radius.

3. Solution of the eigenvalue problem

In the linear high-gain limit the radiation of the electron beam in an undulator could be presented as a set of modes:

$$\vec{E}_\perp(\vec{r}_\perp, z, t) = e^{i\omega(z/c-t)} \sum_k A_k \vec{\Phi}_k(\vec{r}_\perp) \exp[\Lambda_k z]. \quad (4)$$

When amplification takes place, the mode configuration in the transverse plane remains unchanged while the amplitude grows with the undulator length exponentially. Each mode is characterized by the eigenvalue Λ_k ($\mathrm{Re}\,\Lambda_k$ is referred as the field gain) and the eigenfunction $\vec{\Phi}_k(\vec{r}_\perp)$ (which presents the field distribution over transverse coordinate).

In the following we consider the case of annular electron beam with total current I and inner and outer radiuses r_1 and r_0, respectively. The electron beam moves in the field of helical undulator along the axis of circular waveguide and the system is azimuthally symmetric relatively to the z axis.

In the high-gain limit, we find the solutions of the self-consistent field equations (2) for the electric field of the amplified wave in the form of

$$\tilde{E}_{r,\varphi}(z, r, \varphi) = F_{r,\varphi}^{(m)}(r) \exp(-im\varphi + \Lambda z),$$

where m is integer number. Then we go over to complex amplitudes $F_\pm^{(m)} = \left(F_r^{(m)} \pm iF_\varphi^{(m)}\right)$ and in the high gain limit we obtain that the complex amplitude $F_+^{(m)}$ is subjected to the equation:

$$\left[\frac{d^2}{d\hat{r}^2} + \frac{1}{\hat{r}}\frac{d}{d\hat{r}} - \frac{(m-1)^2}{\hat{r}^2} + 2iB\hat{\Lambda} - \frac{2i\hat{D}}{1 - i\hat{D}\hat{\Lambda}_p^2}\right] F_+^{(m)} = 0, \quad (5a)$$

inside the electron beam, at $r_1 < r < r_0$, and outside the electron beam – to the equation:

$$\left[\frac{d^2}{d\hat{r}^2} + \frac{1}{\hat{r}}\frac{d}{d\hat{r}} - \frac{(m-1)^2}{\hat{r}^2} + 2iB\hat{\Lambda}\right] F_+^{(m)} = 0, \quad (5b)$$

The complex amplitude $F_-^{(m)} = \left(F_r^{(m)} - iF_\varphi^{(m)}\right)$ is subjected to the equation

$$\left[\frac{d^2}{d\hat{r}^2} + \frac{1}{\hat{r}}\frac{d}{d\hat{r}} - \frac{(m+1)^2}{\hat{r}^2} + 2iB\hat{\Lambda}\right] F_-^{(m)} = 0, \quad (5c)$$

inside and outside the electron beam. Here notations have been introduced:

$$\hat{r} = r/r_0, \quad \hat{\Lambda} = \Lambda/\Gamma, \quad \hat{C} = C/\Gamma, \quad \hat{\Lambda}_p^2 = \Lambda_p^2/\Gamma^2,$$

$$B = \Gamma r_0^2\omega/c, \quad \Lambda_p = \left[4I/((r_0^2 - r_1^2)I_A\gamma_z^2\gamma)\right]^{1/2},$$

$$\Gamma = \left[I\omega^2\theta_s^2/(I_A c^2\gamma_z^2\gamma)\right]^{1/2}, \quad I_A = m_e c^3/e \simeq 17\ \mathrm{kA},$$

$$\hat{D} = \int_{-\infty}^{\infty} d\xi \left(d\hat{F}(\xi)/d\xi\right)\left[\hat{\Lambda} + i\hat{C} + i\xi\right]^{-1}, \quad (6)$$

where $\hat{F}(\xi)$ is the reduced distribution function. For the Gaussian energy spread distribution the expression for the function $\hat{D}$ has the form:

$$\hat{D} = i\int_0^\infty \xi \exp\left(-\hat{\Lambda}_T^2\xi^2/2 - (\hat{\Lambda} + i\hat{C})\right)\xi d\xi,$$

where $\hat{\Lambda}_T^2 = \sigma^2\omega^2/(\gamma_z^4\mathcal{E}_0^2c^2\Gamma^2)$ is the energy spread parameter and σ is the width of the energy distribution.

The procedure of the solution of the eigenvalue problem consists in writing down general solutions of equations (5) in each of three regions $r < r_1$, $r_1 < r < r_0$ and $r_0 < r < R$ and imposing boundary conditions at the beam boundaries (continuity of eigenfunction and its derivative) and the boundary condition (3) on the waveguide wall. As a result, we obtain the following eigenvalue equation:

$$
\begin{aligned}
&[gK_m(g)J_{m-1}(\mu) - \mu J_m(\mu)K_{m-1}(g)] - \\
&\frac{\mathcal{D}_{(+)}}{2}\{[gI_m(g)J_{m-1}(\mu) + \mu J_m(\mu)I_{m-1}(g)] + \\
&Q[gI_m(g)N_{m-1}(\mu) + \mu N_m(\mu)I_{m-1}(g)]\} - \\
&Q[gK_m(g)N_{m-1}(\mu) - \mu N_m(\mu)K_{m-1}(g)] = 0 . \qquad (7)
\end{aligned}
$$

Here $(J,\ N)$ and $(I,\ K)$ are the Bessel functions of the first and the second kind, respectively,

$$
Q = \frac{\alpha I_m(\alpha)J_{m-1}(\beta) + \beta I_{m-1}(\alpha)J_m(\beta)}{\alpha I_m(\alpha)N_{m-1}(\beta) + \beta I_{m-1}(\alpha)N_m(\beta)} ,
$$

$$
\mathcal{D}_{(\pm)} = \frac{K_m(G)}{I_m(G)} \pm \frac{K'_m(G)}{I'_m(G)}, \qquad \alpha = g\sqrt{B_1/B},
$$

$$
\beta = \mu(B_1/B)^{1/2}, \quad B_1 = \Gamma r_1^2\omega/c ,
$$

$$
G = g(\Omega/B)^{1/2}, \quad \Omega = \Gamma R^2\omega/c ,
$$

$$
g^2 = -2iB\hat{\Lambda}, \quad \mu^2 = -2i\hat{D}\left[1 - i\hat{D}\hat{\Lambda}_p^2\right]^{-1} - g^2.
$$

The radiation field eigenfunction is of the form:
Region 1 $(r < r_1)$:

$$
\begin{aligned}
F_r^{(m)} &= \frac{1}{2\pi}\frac{I_{m-1}(g\hat{r})}{\alpha I_m(\alpha)N_{m-1}(\beta) + \beta I_{m-1}(\alpha)N_m(\beta)} + \\
&\frac{\mathcal{D}_{(-)}}{2}\frac{J_{m-1}(\mu) - QN_{m-1}(\mu)}{K_{m-1}(g) + \mathcal{D}_{(+)}I_{m-1}(g)}I_{m+1}(g\hat{r}), \\
F_\varphi^{(m)} &= -\frac{i}{2\pi}\frac{I_{m-1}(g\hat{r})}{\alpha I_m(\alpha)N_{m-1}(\beta) + \beta I_{m-1}(\alpha)N_m(\beta)} - \\
&\frac{i\mathcal{D}_{(-)}}{2}\frac{J_{m-1}(\mu) - QN_{m-1}(\mu)}{K_{m-1}(g) + \mathcal{D}_{(+)}I_{m-1}(g)}I_{m+1}(g\hat{r}), \qquad (8a)
\end{aligned}
$$

Region 2 $(r_1 < r < r_0)$:

$$
\begin{aligned}
F_r^{(m)} &= J_{m-1}(\mu\hat{r}) - QN_{m-1}(\mu\hat{r}) + \\
&\frac{\mathcal{D}_{(-)}}{2}\frac{J_{m-1}(\mu) - QN_{m-1}(\mu)}{K_{m-1}(g) + \mathcal{D}_{(+)}I_{m-1}(g)}I_{m+1}(g\hat{r}) \\
F_\varphi^{(m)} &= -i[J_{m-1}(\mu\hat{r}) - QN_{m-1}(\mu\hat{r})] + \\
&\frac{i\mathcal{D}_{(-)}}{2}\frac{J_{m-1}(\mu) - QN_{m-1}(\mu)}{K_{m-1}(g) + \mathcal{D}_{(+)}I_{m-1}(g)}I_{m+1}(g\hat{r}) \qquad (8b)
\end{aligned}
$$

Region 3 $(r_0 < r < R)$:

$$
\begin{aligned}
F_r^{(m)} &= \frac{1}{2}\frac{J_{m-1}(\mu) - QN_{m-1}(\mu)}{K_{m-1}(g) + \mathcal{D}_{(+)}I_{m-1}(g)}\left[\mathcal{D}_{(+)}I_{m-1}(g\hat{r}) + \right. \\
&\left. 2K_{m-1}(g\hat{r}) + \mathcal{D}_{(-)}I_{m+1}(g\hat{r})\right], \\
F_\varphi^{(m)} &= -\frac{i}{2}\frac{J_{m-1}(\mu) - QN_{m-1}(\mu)}{K_{m-1}(g) + \mathcal{D}_{(+)}I_{m-1}(g)}\left[\mathcal{D}_{(+)}I_{m-1}(g\hat{r}) + \right. \\
&\left. 2K_{m-1}(g\hat{r}) - \mathcal{D}_{(-)}I_{m+1}(g\hat{r})\right]. \qquad (8c)
\end{aligned}
$$

We also can perform the expansion of the beam radiation mode in a series of the passive waveguide modes. Relative contribution of the passive waveguide TE_{mn} and TM_{mn} modes into the power of the beam radiation mode are given with the expression:

$$
\frac{W_{mn}^{TE,TM}}{W} = \frac{|\ C_{mn}^{TE,TM}\ |^2}{\sum_i |\ C_{mi}^{TE}\ |^2 + \sum_j |\ C_{mj}^{TM}\ |^2} , \qquad (9)
$$

where the coefficients of expansion are given with the expressions:

$$
\begin{aligned}
C_{mn}^{TE} &= \frac{\mu_{mn}P_{mn}^{TE}}{\sqrt{\mu_{mn}^2 - m^2}J_m(\mu_{mn})} \times \\
&\frac{1}{\left[\hat{\Lambda} + i\mu_{mn}^2/2\Omega\right]\left[\mu^2 - M_{mn}^2\right]}, \\
C_{mn}^{TM} &= \frac{P_{mn}^{TM}}{J_{m-1}(\nu_{mn})}\frac{1}{\left[\hat{\Lambda} + i\nu_{mn}^2/2\Omega\right]\left[\mu^2 - N_{mn}^2\right]}, \qquad (10)
\end{aligned}
$$

where

$$
\begin{aligned}
P_{mn}^{TE} &= -\mu J_m(\mu)J_{m-1}(M_{mn}) + \\
&M_{mn}J_{m-1}(\mu)J_m(M_{mn}) + \\
&Q[\mu N_m(\mu)J_{m-1}(M_{mn}) - \\
&M_{mn}N_{m-1}(\mu)J_m(M_{mn})] + \\
&\frac{\alpha I_m(\alpha)J_{m-1}(T_{mn}) + T_{mn}I_{m-1}(\alpha)J_m(T_{mn})}{2\pi[\alpha I_m(\alpha)N_{m-1}(\beta) + \beta I_{m-1}(\alpha)N_m(\beta)]},
\end{aligned}
$$

$$
\begin{aligned}
P_{mn}^{TM} &= -\mu J_m(\mu)J_{m-1}(N_{mn}) + \\
&N_{mn}J_{m-1}(\mu)J_m(N_{mn}) + \\
&Q[\mu N_m(\mu)J_{m-1}(N_{mn}) - \\
&N_{mn}N_{m-1}(\mu)J_m(N_{mn})] + \\
&\frac{\alpha I_m(\alpha)J_{m-1}(L_{mn}) + L_{mn}I_{m-1}(\alpha)J_m(L_{mn})}{2\pi[\alpha I_m(\alpha)N_{m-1}(\beta) + \beta I_{m-1}(\alpha)N_m(\beta)]}.
\end{aligned}
$$

$$
M_{mn} = \mu_{mn}(B/\Omega)^{1/2}, \qquad N_{mn} = \nu_{mn}(B/\Omega)^{1/2},
$$

$$
T_{mn} = \mu_{mn}(B_1/\Omega)^{1/2}, \qquad L_{mn} = \nu_{mn}(B_1/\Omega)^{1/2}.
$$

Let us now analyze some important asymptotes of the dispersion equation (7).

3.1. Solid beam limit

In this case we should let $r_1 \to 0$. As r_1 tends to zero, factor Q tends to zero, too, and eigenvalue equation (7) transforms to the eigenvalue equation for the case of an FEL amplifier with an axisymmetric electron beam with the stepped profile of current density, helical undulator and circular waveguide [2]:

$$[gK_m(g)J_{m-1}(\mu) - \mu J_m(\mu)K_{m-1}(g)] - \frac{1}{2}\left[\frac{K_m(G)}{I_m(G)} + \frac{K'_m(G)}{I'_m(G)}\right] \times [gI_m(g)J_{m-1}(\mu) + \mu J_m(\mu)I_{m-1}(g)] = 0. \qquad (11)$$

3.2. "Open" beam limit

In this case we should let the waveguide walls to be set at infinity, $R \to \infty$ ($\Omega \to \infty$). Using asymptotical expansions of the Bessel functions at large values of arguments, we find that $\mathcal{D}_{(\pm)} \to 0$ at $\Omega \to \infty$ (we assume here $\mathrm{Re}(g) > 0$). As a result, the eigenvalue equation (7) transforms to

$$\mu J_{n+1}(\mu)K_n(g) - gK_{n+1}(g)J_n(\mu) - [gN_n(\mu)K_{n+1}(g) - \mu K_n(g)N_{n+1}(\mu)]\,Z = 0\,, \qquad (12)$$

where $n = \mid m - 1 \mid$ and

$$Z = \frac{\alpha I_{n+1}(\alpha)J_n(\beta) + \beta I_n(\alpha)J_{n+1}(\beta)}{\alpha I_{n+1}(\alpha)N_n(\beta) + \beta I_n(\alpha)N_{n+1}(\beta)},$$

This is the eigenvalue equation of the radiation modes with azimuthal index n of the FEL amplifier with the "open" annular beam. At $r_1 \to 0$ equation (12) transforms to the eigenvalue equation for the case of the FEL amplifier with an "open" axisymmetric electron beam with the stepped profile of current density [3, 4]:

$$\mu J_{n+1}(\mu)K_n(g) - gK_{n+1}(g)J_n(\mu) = 0\,. \qquad (13)$$

It is seen from eqs. (7), (12) and (13) that removal of the waveguide walls leads to double degeneration of azimuthal modes.

3.3. Single-mode approximation

Analysis of the eigenvalue equation (7) shows that at small values of the waveguide diffraction parameter $\Omega \sim 1$, the dependence of the field gain on the detuning has a character of maxima series. It means that each time when the resonant condition of the beam with the corresponding passive waveguide mode is fulfilled, the contribution of the latter to the beam radiation mode becomes dominating at small values of waveguide diffraction parameter Ω (see eqs. (10)). This situation could be well described with a single-mode approximation. Physically this is the region of small values of the beam current I. At $I \to 0$ we should let $B \to 0$, $\Omega/B = \mathrm{const}$ and $\Lambda/\Gamma \to \infty$. In zeroth approximation we find that $\mu = ig$ and equation (7) takes the form $I_m(G)I'_m(G) = 0$. As a result, we obtain zeroth approximation for the eigenvalues:

$$\hat{\Lambda} = \hat{\Lambda}_0 = -i\mu_{mn}^2/(2\Omega) \qquad \text{for } \mathrm{TE}_{mn} \text{ mode,}$$

$$\hat{\Lambda} = \hat{\Lambda}_0 = -i\nu_{mn}^2/(2\Omega) \qquad \text{for } \mathrm{TM}_{mn} \text{ mode.}$$

Representing the eigenvalue in the form $\hat{\Lambda} = \hat{\Lambda}_0 + \hat{\Lambda}_1$ where $\hat{\Lambda}_1$ is small, we obtain from equation (7) the eigenvalue equation for the single-mode approximation:

$$\left[V\left[\hat{\Lambda} - \hat{\Lambda}_0\right]^{-1} - \hat{\Lambda}_p^2\right]\hat{D} = i, \qquad (14)$$

where factor V for TE_{mn} mode is given with the expression:

$$V^{TE} = \frac{i\mu_{mn}^2}{2\Omega[B - B_1]J_m^2(\mu_{mn})(\mu_{mn}^2 - m^2)} \times \left\{B\left[J_m^2(M_{mn}) - J_{m-1}(M_{mn})J_{m+1}(M_{mn})\right] - B_1\left[J_m^2(T_{mn}) - J_{m-1}(T_{mn})J_{m+1}(T_{mn})\right]\right\},$$

and for TM_{mn} mode - with the expression

$$V^{TM} = \frac{i}{2\Omega[B - B_1]J_{m-1}^2(\nu_{mn})} \times \left\{B\left[J_m^2(N_{mn}) - J_{m-1}(N_{mn})J_{m+1}(N_{mn})\right] - B_1\left[J_m^2(L_{mn}) - J_{m-1}(L_{mn})J_{m+1}(L_{mn})\right]\right\}.$$

In the case of negligibly small energy spread eigenvalue equation (14) reduced to the cubic one:

$$\left[\left(\hat{\Lambda} + i\hat{C}\right)^2 + \hat{\Lambda}_p^2\right]\left[\hat{\Lambda} - \hat{\Lambda}_0\right] = V.$$

4. References

[1] A.A. Kaminsky et. al, Proc. of the XV-th International Conference on High Energy Accelerators, Vol. II, pp. 900-902 (World Scientific, Singapore, 1993).

[2] E.L. Saldin, E.A. Schneidmiller and M.V. Yurkov, Opt. Commun. **85**(1991)117.

[3] G.T. Moore, Opt. Commun. **52**(1984)46.

[4] E.L. Saldin, E.A. Schneidmiller and M.V. Yurkov, Opt. Commun. **97**(1993)272.